Forschungszentrum Karlsruhe
Technik und Umwelt

Wissenschaftliche Berichte
FZKA 5587

Corrosion Studies on Selected Packaging Materials for Disposal of Heat-Generating Radioactive Wastes in Rock-Salt Formations

E. Smailos, J. A. Gago, I. Azkarate, B. Fieh
Institut für Nukleare Entsorgungstechnik

Keep
one package

Mai 1995

Summary

In previous corrosion studies, carbon steels and the alloy Ti 99.8-Pd were identified as promising materials for heat-generating nuclear waste containers that could act as a barrier for immobilization of radionuclides in a rock-salt repository. For this reason, these materials are subject to more detailed investigations. In the present study, the long-term corrosion behaviour of three preselected carbon steels has been investigated in the liquid and vapor phase of disposal relevant brines at 150°C-170°C without radiation and in the presence of a gamma radiation field. Stress corrosion cracking studies (SCC) were also performed on the steels in an $MgCl_2$-rich brine at 25°C-170°C and slow strain rates of 10^{-4}-$10^{-7}s^{-1}$.

In addition to these laboratory-scale experiments, long-term in-situ experiments on Fe-base alloys, Ti 99.8-Pd and Hastelloy C4 were performed in the Asse salt mine. Both metal sheets and tubes of these materials with selected container manufacturing characteristics (e.g. sealing technique, corrosion protection of steel with either Ti 99.8-Pd or Hastelloy C4) were examined in rock salt and rock salt plus brine at 32°C-200°C.

Both in the liquid and in the vapor phase of the brines the steels investigated (unalloyed TStE 355 steel, low-alloyed TStE 460 and 15MnNi 6.3 steels) are resistant to pitting corrosion. The liquid-phase corrosion rates (36-71 µm/a in NaCl-rich brine, 65-203 µm/a in $MgCl_2$-rich brines) are significantly higher than the vapor-phase corrosion rate (10 µm/a), but they imply acceptable corrosion allowances for thick-walled containers. The gamma dose rate of 10 Gy/h and the submerged arc welding (SAW) do not accelerate the corrosion rates of the steels in NaCl-rich brine. In $MgCl_2$-rich brines, the corrosion rates in the irradiated environment are a factor of about 1.5 higher than in the unirradiated system, and the welded specimens are suffered from deep local corrosion attacks.

Under the conditions of the slow strain rate tests in the $MgCl_2$-rich brine, the TStE 355 steel is resistant to SCC. The TStE 460 steel shows a sensitivity to SCC at 170°C and $10^{-5}s^{-1}$, whereas the forged 15MnNi 6.3 is highly susceptible to SCC at 90°C and 170°C at strain rates of $10^{-7}s^{-1}$ and $10^{-5}s^{-1}$, respectively.

Under the in-situ test conditions, corrosion of all materials is negligible small. Only in rock salt plus $MgCl_2$-rich brine, the steel exhibits a high general corrosion rate (90 µm/a). In view of these results the unalloyed TStE 355 steel and Ti 99.8-Pd continue to be considered as the most promising container materials and will be further investigated.

FORSCHUNGSZENTRUM KARLSRUHE
Technik und Umwelt

Wissenschaftliche Berichte
FZKA 5587

CORROSION STUDIES ON SELECTED PACKAGING MATERIALS FOR DISPOSAL OF HEAT-GENERATING RADIOACTIVE WASTES IN ROCK-SALT FORMATIONS

E. Smailos, J.A. Gago*, I. Azkarate**, B. Fiehn
Institut für Nukleare Entsorgungstechnik

* ENRESA, Spain
** INASMET, Spain

CEC-Contract F I 2 W - CT 90 - 0030
Final Report 1991-1994

Forschungszentrum Karlsruhe GmbH, Karlsruhe
1995

Korrosionsuntersuchungen an ausgewählten Verpackungsmaterialien für die Endlagerung von wärmeerzeugenden radioaktiven Abfällen in Steinsalzformationen

Zusammenfassung

Bisherige Korrosionuntersuchungen ergaben, daß Kohlenstoffstähle und die Legierung Ti 99.8-Pd aussichtsreiche Materialien für langzeitbeständige Behälter zur Endlagerung von wärmeerzeugenden Abfällen in Steinsalzformationen sind. Deshalb werden diese Werkstoffe detaillierter untersucht. In der vorliegenden Arbeit wurde das Langzeit-Korrosionsverhalten von drei ausgewählten Stählen in der Flüssig- und in der Dampfphase von endlagerrelevanten Salzlösungen bei 150°C-170°C mit und ohne Gammastrahlenfeld untersucht. Darüber hinaus wurde die Beständigkeit der Stähle gegenüber Spannungsrißkorrosion (SpRK) in einer $MgCl_2$-reichen Lösung bei 25°C-170°C und langsamen Dehnungsraten von 10^{-4}-$10^{-7}s^{-1}$ geprüft.

Zusätzlich zu den oben genannten Laborexperimenten wurden auch In-Situ-Experimente an Eisenbasislegierungen, Ti 99.8-Pd und Hastelloy C4 im Salzbergwerk Asse durchgeführt. Neben Metallblechen wurden auch Rohrabschnitte aus diesen Materialien, versehen mit ausgewählten Herstellungsmerkmalen für Behälter (z.B. Verschlußtechnik, Korrosionsschutz von Stahl durch Ti 99.8-Pd oder Hastelloy C 4), in Steinsalz bzw. Steinsalz plus Lösung bei T=32°C-200°C geprüft.

Sowohl in der Flüssig- als auch in der Dampfphase der Lösungen sind die untersuchten Stähle (unlegierter Stahl TStE 355, niedriglegierte Stähle TStE 460 und 15MnNi 6.3) beständig gegenüber Lochkorrosion. In der Flüssigphase sind die linearen Korrosionsraten (36-71µm/a in der NaCl-reichen Lösung bzw. 65-203 µm/a in den $MgCl_2$-reichen Lösungen) deutlich höher als in der Dampfphase (10 µm/a) jedoch führen die Werte zu technisch akzeptablen Behälterkorrosionszuschlägen. Ein Gammastrahlenfeld von 10 Gy/h und das Unterpulverschweißen führen zu keiner Erhöhung der Korrosionsraten der Stähle in der NaCl-reichen Lösung bei 150°C. In den $MgCl_2$-reichen Lösungen sind die Korrosionsraten unter Bestrahlung etwa um den Faktor 1,5 höher als ohne Bestrahlung und bei den geschweißten Proben treten starke lochfraßartige Korrosionsangriffe auf.

Die Untersuchungen in einer $MgCl_2$-reichen Lösung bei Dehnungsraten von 10^{-4}-$10^{-7}s^{-1}$ zeigen, daß der Stahl TStE 355 beständig gegenüber SpRK ist. Der Stahl TStE 460 zeigt eine Empfindlichkeit gegenüber SpRK bei 170°C und einer Dehnungsrate von $10^{-5}s^{-1}$, während bei dem Schmiedestahl 15MnNi 6.3 eine starke Empfindlichkeit gegen diese Korrosionsart sowohl bei 90°C als auch bei 170°C bei Dehnungsraten von $10^{-7}s^{-1}$ bzw. $10^{-5}s^{-1}$ festgestellt wurde.

Unter den In-Situ-Prüfbedingungen ist die Korrosion aller Werkstoffe gering. Nur in Steinsalz plus $MgCl_2$-reiche Lösung tritt bei Stahl eine starke Flächenkorrosion von ca. 90 µm/a auf. Aufgrund der Ergebnisse dieser Arbeit werden der unlegierte Stahl TStE 355 und Ti 99.8-Pd weiterhin als aussichtsreiche Behälterwerkstoffe betrachtet und werden weiter untersucht.

Table of Contents

		Page
	Summary	
1.	Introduction and objectives	1
2.	General and local corrosion testing of carbon steels in brines with and without gamma irradiation (FZK)	2
2.1	Materials and specimens	2
2.2	Test conditions	3
2.3	Experimental set-ups	4
2.4	Post-test examination of the specimens	5
2.5	Results	6
2.5.1	Corrosion of the unalloyed TStE 355 steel	6
2.5.2	Corrosion of the low-alloyed TStE 460 and 15MnNi 6.3 steels	8
3.	In-situ corrosion studies on selected container materials (FZK)	9
3.1	Testing of metal sheets	10
3.2	Testing of welded tubes	11
3.2.1	Test field and details of the specimens	11
3.2.2	Test conditions and experimental set-up	11
3.2.3	Post-test examination of the specimens	13
3.2.4	Results	13
4.	Stress corrosion cracking testing of carbon steels (ENRESA/INASMET)	15
4.1	Materials and experimental	15
4.2	Results	16
5.	Conclusions	20
6.	References	21

1. INTRODUCTION AND OBJECTIVES

According to the German concept, the heat-generating nuclear waste such as vitrified high-level waste and spent fuel will be disposed of in repositories located in deep rock-salt formations. The isolation of the radionuclides from the biosphere shall be ensured by a combination of geological and engineered barriers. One element of this multi-barrier system is the waste packaging. Consequently, studies have been undertaken by FZK within the framework of the European Union research programme to qualify materials for long-lived packagings that could act as a radionuclide barrier during the elevated-temperature phase in the disposal area, which lasts a few hundred years. The main requirement made on the packaging materials is their corrosion resistance in rock salt and salt brines. Salt brines in the disposal area may originate from the thermal migration of brine inclusions in the rock salt and have to be considered in accident scenarios, e.g. brine inflow through an anhydride layer.

In previous corrosion studies on a wide range of materials in salt brines [e.g. 1,2,3], two materials were identified as the most promising for the manufacturing of long-lived containers surrounding the Cr-Ni steel waste canisters. These are: The passively corroding alloy Ti 99.8-Pd for a corrosion resistant concept and the actively corroding carbon steels for a corrosion allowance concept. To characterize the corrosion behaviour of these materials in more detail, a 1991-1994 EU research programme was performed jointly by FZK and ENRESA/ INASMET (Spain).

The research programme consists of two parts In the first part, FZK studied the influence of important parameters on the long-term corrosion behaviour of four preselected carbon steels (two unalloyed, two low-alloyed) and Ti 99.8-Pd in disposal relevant salt brines. These parameters are: Temperature, gamma radiation and selected characteristics of container manufacturing. Both, laboratory-scale immersion experiments and in-situ corrosion studies in the Asse salt mine were carried out.

The second part of the corrosion studies concerns the investigation of resistance of the carbon steels to stress corrosion cracking in a disposal relevant salt brine at variable strain rates and temperatures by ENRESA/INASMET. For this purpose, the slow strain rate technique (SSRT) was applied. These studies served to complete the results available so far on statically loaded U-bent specimens. The entire research programme was coordinated by FZK.

In the present paper, the progress achieved in the research programme from January 1991 to December 1994 shall be described.

2. GENERAL AND LOCAL CORROSION TESTING OF CARBON STEELS IN BRINES WITH AND WITHOUT GAMMA IRRADIATION (FZK)

2.1 Materials and specimens

One unalloyed and two low-alloyed carbon steels were investigated which are discussed in the Federal Republic of Germany as container materials for the disposal of HLW/Spent Fuel in rock salt. The steels investigated in brines had the following compositions in wt.%:

Fine-grained steel TStE 355 (unalloyed):

0.17C; 0.44 Si; 1.49 Mn; bal. Fe

TSt E 460:

0.18 C; 0.34 Si; 1.5 Mn; 0.51 Ni; 0.15 V; bal. Fe

15MnNi 6.3 (low-alloyed):

0.17 C; 0.22 Si; 1.59 Mn; 0.79 Ni; bal. Fe

The parent materials of the TStE 355 and TStE 460 steels were hot-rolled and annealed plates, and for 15MnNi 6.3 forged and annealed disks. For the TStE 355 and TStE 460 steels, a ferritic microstructure with perlite bands typical of the rolling process was observed. A grain size value of 10 according to ASTM E- 112 was measured for both steels. For the 15MnNi 6.3 forged steel, a ferrite-perlite microstructure of a duplex grain size with an average value of 9 (according to ASTM E- 112) was observed.

For the investigation of the general and local corrosion in brines, plane specimens of the dimensions 40mm x 20mm x 4mm were used. Prior to specimen fabrication, the parent materials were freed from the adhering oxide layer by milling. After this mechanical treatment, specimens were cut and cleaned with alcohol in an ultrasonic bath.

The TStE 355 steel was examined for general and local corrosion in the brines only in the as-received condition. In case of the TStE 460 and 15MnNi 6.3 steels, submerged arc welded (SAW) specimens were tested in addition to specimens of the parent materials with a view to examine the influence of this welding technique discussed for the spent fuel disposal container closure on the corrosion.

For the welding of the steels, materials in the forged and annealed condition were used.

2.2 Test conditions

The test conditions for the steels are summarized in Table 1. All three steels were investigated for general and local corrosion in the liquid phase of disposal relevant brines simulating conditions after intrusion of large amounts of brine into the disposal area. In addition to these immersion experiments, the unalloyed TStE 355 steel was examined in the vapor phase of an $MgCl_2$-rich brine. Such experiments simulate conditions after intrusion of limited amounts of brine into the lower part of the HLW boreholes and location of the up to 300-600 m stocked containers in the vapor space over the brine.

To examine the influence of the brine composition on the corrosion behaviour of the steels, three disposal relevant salt brines differing qualitatively and quantitatively were used as the corrosion media. Two of them, brine 1 (Q-brine) and brine 2 are highly concentrated in $MgCl_2$, the third one (brine 3) has a high concentration of NaCl. The compositions and the measured pH and O_2-values of the test brines are given in Table 2. The pH values given are relative data and were measured using a glass electrode. Application of the correction formula proposed by Bates et al. [4] gives pH values at 25°C which are higher than the measured values by 1.8-2.2 units for the brines 1 and 2, and by 0.4 units for the brine 3. The O_2-values of the brines were determined by a polarographic method using an O_2-sensor; the saturation values (1.0-1.4 mg O_2/l) obtained by the Winkler method were used as the reference values. Liquid corrosion of the steels was investigated in all three brines, whereas vapor corrosion of the TStE 355 steel was examined only in the brine 1. In these vapor corrosion studies, besides investigations in pure brine, experiments were conducted in sulfide containing brines in order to examine the influence of this salt impurity on corrosion. The sulfide was added to the brine as Na_2Sx9H_2O at concentrations of $6x10^{-4}$ M/l, $3x10^{-3}$ M/l, and $6x10^{-3}$ M/l, respectively.

The steels were examined up to 18 months in the liquid and in the vapor phase of the brines at temperatures of 150°C and 170°C that roughly correspond to the maximum temperature on the surface of the disposal containers according to the German concept. The investigations on the low-alloyed steels (TStE 460 and 15MnNi 6.3) were performed without gamma irradiation, because the dose rate

expected on the surface of the about 30 cm thick-walled spent fuel disposal containers is negligible low.

However, by using carbon steel containers for disposal of vitrified high-level waste (HLW) in boreholes, mechanical and corrosion allowances of the order of 10-15 cm are discussed for containers with a service life of 300 years. In this case, gamma dose rates of 1 Gy/h - 10 Gy/h are calculated. To get information about the influence of gamma radiation on the corrosion of the steels at high temperature, the TStE 355 unalloyed steel was tested up to about 600 days in the brines at 150°C in the presence of a gamma radiation of 10 Gy/h. For comparison, also experiments without irradiation were performed. Investigations under gamma irradiation are important because the radiolytic productss formed by the impact of radiation on salt brines, e.g. H_2O_2, ClO^-, ClO_3^- etc. [5], might influence the corrosion process.

2.3 Experimental set-ups

For the corrosion experiments without irradiation, stainless steel pressure vessels with corrosion-resistant polytetrafluorethylene (PTFE) inserts of 250 ml volume were used to avoid evaporation of the brines at the high test temperatures (150°C and 170°C). Each PTFE insert contained 200 ml of brine and two specimens of 40 cm^2 total surface. This gave a brine volume to specimen surface ratio (V/S) of 5 ml/cm^2. This means that the experiments were performed for an excess of the corrodents. The steel specimens were suspended by PTFE threads, which were fixed below the lid of the insert, and immersed into the brine (liquid corrosion) or they were located in the vapor space of the pressure vessels (vapor corrosion). After tightly closing the inserts, the vessels were stored in heating chambers at the test temperatures. In the case of the vapor-corrosion experiments, the environment was water vapor-saturated air. The experiments were caried out at an equilibrium pressure of about 0.5 MPa.

The corrosion experiments under gamma irradiation were performed in the spent fuel storage pool of KFA Jülich. The radiation source were spent fuel elements with a gamma energy spectrum similar to that of 10-years-old vitrified HLWC. The experimental set-up is shown schematically in Fig. 1. For the experiments, autoclaves made of the corrosion resistant alloy Ti 99.8-Pd with insert vessels of Duran glass were used. The autoclaves were placed in a circular configuration into heated cylindrical stainless steel containers (irradiation containers). Each glass insert contained 120 ml of brine and three specimens of 60 cm^2 total surface, which were totally immersed into the brine. This gave a brine volume to

specimen surface ratio of 2 ml/cm². The specimens were suspended from a frame made of a glass-fibrereinforced plastic. For irradiation, the stainless steel containers were positioned at the bottom of the 6 m deep water-filled spent fuel element storage pool. The specimens and brines were heated to the test temperature of 150°C using heaters. To determine the corrosion kinetics, the specimens were examined at various test times.

2.4 Post-test examination of the specimens

After removal from the brines, the specimens were examined for general and local corrosion. The general corrosion expressed as the average thickness reduction of the specimens was calculated from the gravimetrically measured weight losses and the material density. To determine the time dependence of the general corrosion, regression analyses of the thickness reduction values were performed by means of the SAS® software (registered trademark of the SAS Institute Inc., Cary, NC, USA). Application of SAS for statistical analyses of corrosion data has already been described in previous work [6].

For the regression analyses, the following equations were examined:

$$\Delta S = A + B \cdot t \qquad (1)$$

$$\Delta S = A + B \cdot t + C \cdot t^2 \qquad (2)$$

$$\Delta S = A + B \cdot t^N \qquad (3)$$

where A, B, C and N are the regression coefficients, t the time and ΔS the computed thickness reduction.

The parameter A can be interpreted as an indicator of an initial corrosion process that is influenced by the preparation of the specimens. This parameter is of minor importance for the long-term thickness reduction of the specimens. The parameter B gives a measure of the linear corrosion rate, whereas the two other coefficients (C,N) can be taken as an indication of the formation of protecting corrosion layers on the specimen surface.

Evaluation of the specimens with regard to local corrosion was carried out by measurements of the pitting depths, surface profilometry and metallography. Additional information on the corrosion mechanism was obtained from the

analysis of the corrosion products by means of X-ray diffraction (XRD) and Mössbauer-spectroscopy.

2.5 Results

2.5.1 Corrosion of the unalloyed TStE 355 steel

The time-dependence of the thickness reduction of the TStE 355 steel in the liquid phase of irradiated (10 Gy/h) and unirradiated brines at 150°C and a V/S-ratio of 2 ml/cm² is plotted in Figs. 2-4. The results show a linearly increase of the thickness reduction with exposure time. The results of the linear regression analyses for the thickness reduction of the steel in the test brines are compiled in Table 3. In both cases with and without gamma radiation, the corrosion rates (B) of the steel in the $MgCl_2$-rich brines 1 and 2 are significantly higher than in the NaCl-rich brine 3. The higher corrosivity of the $MgCl_2$-rich brines compared to the NaCl-rich brine is attributed to their higher HCl concentration. This could be explained by the higher Cl^--concentration and the hydrolysis of Mg^{2+}. The acceleration of steel corrosion in brines containing high amounts of $MgCl_2$ is in line with the results reported by Westerman et al. [7].

The imposition of a 10 Gy/h radiation field on the 150°C brine environment increases the linear corrosion rates of the steel specimens in the brines 1 and 2 from about 47 µm/a to 72 µm/a, and from 120 µm/a to 162 µm/a, respectively. In brine 3, the corrosion rate in the 10 Gy/h irradiated environment (13.7 µm/a) is very close to the value attained in the unirradiated system (15.3 µm/a).

Surface profiles and metallographic examinations of corroded specimens have shown that the steel is resistant to pitting corrosion in both irradiated and unirradiated brines. In all brines, a non-uniform general corrosion was observed. However, the measured maximum penetration depth of this uneven corrosion corresponds to the values of the average thickness reduction. Figure 5 shows optical micrographs of steel specimens after 166 days of exposure to the test brines at 150°C and 10 Gy/h.

The regression analysis of the time-dependent thickness reduction of the steel at 170°C in the vapor phase of the brines shows that a linear equation fits the experimental data well. This is in good agreement with the results obtained in the liquid phase of the brines. The experimental data of the vapor-phase corrosion and the regression line are plotted in Figs. 6 through 9. The results of the linear regression analysis of the thickness reduction of the steel in the various brines are compiled in Table 4. For comparison, the corrosion results in the liquid

phase of the brines at the same V/S ratio of 5 ml/a determined in earlier work [8] are also given in Figs. 6 through 9 and Table 4.

In the vapor phase of the Na_2S-free brine, the linear corrosion rate of the steel is about 10 µm/a and, hence, significantly lower than that in the liquid phase (about 200 µm/a). By Na_2S additions of $6x10^{-4}$ - $6x10^{-3}$ M/l to the brine, the vapor-phase corrosion rates increase to about 20-40 µm/a. However, the values remain clearly lower than those in the liquid phase (about 192-317 µm/a). Both in the liquid and in the vapor phase of the brines, the maximum corrosion rate occur at a Na_2S concentration of $3x10^{-3}$ M/l. At the higher Na_2S concentration of $6x10^{-3}$ M/l the corrosion rate decreases. This effect may probably be attributed to the formation of a denser corrosion layer at the higher Na_2S concentration, as was observed in the metallographic examinations.

Tenacious black corrosion products were present on all the steel specimens following exposure to the water vapor-saturated gas phase of the brines with and without Na_2S. X-ray diffraction and Mössbauer-spectroscopic analyses have shown that the corrosion products primarily consist of Fe_3O_4 (magnetite). In addition, α-Fe_2O_3 (hematite) and α/β-FeOOH were identified. The formation of higher oxidation-state oxides such as Fe_2O_3 or FeOOH is due to the fact that oxygen was present during the tests. The presence of tenacious corrosion products of Fe_3O_4 in the specimens is consistent with the observed low rates of general corrosion in the vapor phase of the brines.

For the TStE 355 steel specimens exposed to liquid phase of the $MgCl_2$-rich brine 1, a magnesium-containing ferrous hydroxide, $(Fe,Mg)(OH)_2$, of amakinite structure was identified as the primary corrosion product, without evidence of Fe_3O_4. It appears that Mg^{2+}, when present at high concentrations in the brine, inhibits the normal formation of Fe_3O_4 from a $Fe(OH)_2$ precursor. The higher corrosion rates observed in the liquid phase of the brines, compared to the vapor phase, suggest that $(Fe,Mg)(OH)_2$ is less protective than Fe_3O_4. A further reason for the high liquid-phase corrosion is considered to be the high HCl concentration of the brine. This could be explained by the high Cl^- concentration and the hydrolysis of Mg^{2+}, as already discussed. The formation of $(Fe,Mg)(OH)_2$ in $MgCl_2$-rich salt brines has also been reported by Westerman et al. [7].

The contribution of oxygen to corrosion should be low, because the limited amount of oxygen (about 15 mg) available in the closed experimental equipment will be consumed after a relatively short time due to the reaction with iron.

It is evident from the metallographic examinations and the surface profiles of specimens exposed to the vapor phase of the brines that the steel is resistant to pitting corrosion in the sense of an active-passive corrosion element. As in the liquid phase, a non-uniform general corrosion of a maximum depth of 80-100 µm was observed in all brines with and without Na_2S. However, with increasing test duration this uneven corrosion attack spread over the specimen surface rather than penetrated into the metal and the penetration rate decreased. Therefore, the gravimetrically determined general corrosion rates (about 10-43 µm/a) are of decisive importance for long-term predictions of the container lifetime in the vapor phase of the $MgCl_2$-rich Q-brine. Characteristic optical micrographs of the steel after 320 days of exposure to the vapor phase of the test brines at 170°C are shown in Figs. 10 through 13.

2.5.2 Corrosion of the low-alloyed TStE 460 and 15MnNi 6.3 steels

The general corrosion of the unwelded steel specimens (parent materials) at 150°C in the liquid phase of the brines, expressed as the thickness reduction, is plotted in Fig. 14. As in the case of the TStE 355 unalloyed steel, the thickness reduction in the brines increases linearly with exposure time. The results of the linear regression analyses of the thickness reduction for the steels in the brines are compiled in Table 5. The lowest corrosion rates occur in the NaCl-rich brine 3 with values of 56 µm/a (TStE 460) and 71 µm/a (15MnNi 6.3), respectively. In the $MgCl_2$-rich brines 1 (Q-brine) and 2, higher corrosion rates (65-203µm/a for TStE 460, 94-117 µm/a for 15 MnNi 6.3) are obtained compared to the values of the NaCl-rich brine. The higher corrosivity of the $MgCl_2$-rich brines compared to the NaCl-rich brine is attributed to their higher HCl-concentration, as already discussed for the TStE 355 steel.

It is evident from the metallographic examinations and the surface profiles that the unwelded specimens are resistant to pitting corrosion in all three brines. A non-uniform corrosion is observed for both steels in the test brines which is attributed to inhomogeneities of the steel composition. However, the maximum penetration depth of this uneven corrosion attack corresponds to the values of the average thickness reduction. Characteristic optical micrographs of the TStE460 and 15MnNi 6.3 steels after an 18-month exposure to brine 1 (Q-brine) at 150°C are shown in Fig. 15.

Welding do not influence noticeably the corrosion behaviour of the steels in the NaCl-rich brine 3. The SAW specimens undergo a non-uniform corrosion attack as did the unwelded specimens, and the general corrosion rates correspond to the values obtained for the parent materials. In the $MgCl_2$-rich brines, however, considerable local corrosion attacks are detected for both steels in the heat-affected zone. The depth of these corrosion attacks increases with exposure time to the brines and after 18 months reaches values between 2 mm and 4 mm, depending on the steel and the brine (Tab.6). Figure 16 shows optical micrographs of welded specimens of the TStE 460 and 15MnNi 6.3 steels after an 18-month exposure to brine 1.

The corrosion products formed on the surface of the steel specimens were analysed by X-ray diffraction. For specimens exposed to the NaCl-rich brine 3, Fe_3O_4 (magnetite) and γ-Fe_2O_3 (maghemite) were identified. In the $MgCl_2$-rich brines, (Fe, Mg)$(OH)_2$ of the amakinite structure and β-FeOOH (akaganeite) were found, with no evidence of oxides.

3. IN-SITU CORROSION STUDIES ON SELECTED CONTAINER MATERIALS (FZK)

On the basis of the corrosion results obtained so far and considering mechanical aspects, a thick-walled carbon steel container with or without a corrosion protection made of Ti 99.8-Pd was identified for the packaging of the wastes [9,10]. As an alternative to Ti 99.8-Pd, the suitability of Hastelloy C4 as a corrosion protection material is being examined. Both, in-depth laboratory-scale and in-situ corrosion studies are being performed.

An important aspect of the in-situ studies is the investigation of the influence of selected container manufacturing characteristics (e.g. sealing technique, application mode of the corrosion protecting layer on the steel) on the corrosion of the materials. Therefore, besides metal sheets, two types of cast steel tubes are being examined under simulated disposal conditions in heated boreholes in the Asse salt mine:

- Non-corrosion protected cast steel tubes with the container sealing technique being simulated by electron beam (EB) welding.
- Corrosion protected cast steel tubes with the corrosion protection of either Ti 99.8-Pd or Hastelloy C4 being simulated by explosion plating and electron beam welding.

In addition to the cast steel tubes, some investigations are being performed on electron beam and tungsten inert gas (TIG) welded tubes made of Ni-resist D4 (an Fe-base material) and Ti 99.8-Pd in order to complete the results available to date.

In-situ corrosion results obtained for metal sheets and tubes after 1.5-3 years of exposure to rock salt and rock salt plus brine have already been reported about [2,11,12]. In the period under review, the long-term in-situ corrosion experiments lasting up to about 9 years for metal sheets and 6 years for tubes, respectively, were completed and the specimens were examined for corrosion attacks.

3.1 Testing of metal sheets

Metal sheets of Ti 99.8-Pd, Hastelloy C4 and the two Fe-base materials Ni-resist D4 and Si-cast iron were investigated for 9 years in loose rock salt at the rock temperature of 32°C. For this, material specimens were stored in small boreholes (50 mm diameter, 200 mm length) at the 775 m level of the Asse salt mine and covered with salt grit. The composition of the materials investigated is evident from Table 7. The rock salt had the following average composition (wt.%).

Na^+: 38.3; K^+: 0.33; Ca^{2+}: 0.17; Mg^{2+}: 0.16;

Cl^- : 58.02; SO_4^{2-}: 2.47; H_2O: 0.1.

For Ni-resist and Si-cast iron, only the parent materials (as received) were studied. For the most promising HLW container materials Ti 99.8-Pd and Hastelloy C4, the influence of welding on the corrosion behaviour was studied with respect to container closing by welding in a later application. For this purpose, specimens were examined with a TIG (Tungsten Inert Gas) weld beam applied.

All material specimens were examined for their resistance to general corrosion (weight change) and local corrosion by gravimetry, surface profilometry and metallography. Plane specimens with the following dimensions were used: Ti 99.8-Pd, Hastelloy C4 and Si-cast iron: 40 mm x 20 mm x 4 mm; Ni-resist D4: 50 mm x 10 mm x 10 mm.

The integral weight losses of the specimens after 9 years of testing at 32°C and the integral corrosion rates calculated from them are presented in Table 8. The values are average values of three specimens. No measurable corrosion attack was observed on Ti 99.8-Pd. Moreover, the corrosion rates for the materials Hastelloy C4, Ni-resist D4 and Si-cast iron are very small (0.17-1.14 µm/a). The surface profiles and the metallographic examinations of the specimens in the as-received and welded conditions do not provide any indication of local corrosion.

3.2 Testing of welded tubes

3.2.1 Test field and details of the specimens

The configuration and dimensions of the underground test field at the 775 m level in the Asse salt mine are shown in Fig. 17. The composition of the rock salt taken from the test field boreholes is given in section 3.1.

Following eight tubes were investigated under simulated disposal conditions (see section 3.2.2):

- Five electron-beam (EB) welded cast steel tubes (GS 16 MnS). Two do not have any corrosion protection, two are provided with a corrosion protection layer of Ti 99.8-Pd, and one with Hastelloy C4 applied by explosion plating and EB-welding.
- One tungsten inert gas (TIG) welded tube made of Ti 99.8-Pd.
- Two electron-beam welded tubes made of the Fe-base material Ni-resist D4.

The tube materials used had the following compositions in wt.%:

Cast steel: 0.16 C; 0.66 Si; 1.51 Mn; 0.02 P+S; bal. Fe.

Ti 99.8-Pd: 0.2 Pd; 0.03 Fe; bal. Ti.

Hastelloy C4: 15.5 Cr; 15.3 Mo; 0.8 Fe; bal. Ni.

Ni-resist D4: 30.9 Ni; 5.5 Cr; 2.6 C; 4.25 Si; 0.5 Mn; bal. Fe.

The specimens of cast steel and Ni-resist D4 consisted of nine tube sections (50 mm length, 45 mm outside diameter, 20 mm inside diameter each) and a bottom part which was joined by EB-welding to simulate a container sealing technique. Thus, tubes of 500 mm total length were obtained. Figure 18 shows a cast steel specimen by way of example. The Ti 99.8-Pd specimen was a tube (L=500 mm, D=25.4 mm) with a longitudinal weld and a TIG-welded bottom. More detailed information on the manufacturing of the specimens can be found elsewhere [13].

3.2.2 Test conditions and experimental set-up

The tubes were tested under the following conditions:

- Two cast steel tubes with and without corrosion protection made of Ti 99.8-Pd, and two Ni-resist D4 tubes were tested for 5.3 years in the Asse rock salt (H_2O content: 0.1 wt.%) at HLW design temperature ($T_{max.}$=200°C). Thus, the normal operating conditions of a repository were simulated.

- Three carbon steel tubes with and without corrosion protection of Ti 99.8-Pd or Hastelloy C4, and one TIG-welded Ti 99.8-Pd tube were tested under the conditions of a hypothetical inflow of brine into the HLW boreholes during the initial disposal phase. This means while the annular gap between the container and the borehole wall was still open. The carbon steel tubes were tested for 6.3 years both in an $MgCl_2$-rich brine (Q-brine) and in saturated NaCl-brine at rock temperature of 32°C. The Ti 99.8-Pd tube was examined for 2.8 years only in NaCl-brine at $T_{max.} = 200°C$.

Each tube was placed into a heated vertical borehole of 2 m depth at the 775 m level of the Asse salt mine (see Fig. 19). At the beginning of the experiments, a 1 mm wide annular gap existed between the tubes and the borehole wall. In the experiments with brine as the corrosion medium, the annular gap was filled with 100 ml Q-brine (26.8 wt.% $MgCl_2$; 4.7 wt.% KCl; 1.4 wt.% $MgSO_4$; 1.4 wt.% NaCl; 65.7 wt.% H_2O) or NaCl-brine (26.9 wt.% NaCl; 73.1 wt.% H_2O).

The temperature of 200°C was set at the borehole wall using a heater. The radial temperature distribution between two boreholes and the vertical temperature profile developed during the experiments at the contact surface between the tube and the borehole wall are shown in Figs. 20 and 21. The maximum temperature of 200°C occurred in the centre of the heated zone, the minimum temperature of 90°C was measured in the upper tube zone. The temperature in the centre between two boreholes nearly corresponded to the rock salt temperature of about 32°C at the 775 m level. The temperature was measured using NiCr-Ni thermocouples. In order to avoid invalidation of the corrosion results due to the corrosion induced by the contact of the thermocouples and tube surface, the temperature measurements were performed in reference boreholes of identical experimental set-up. In the experiments with the presence of brine and T = 200°C, the pressure in the annular gap of the real test boreholes was measured continuously with a manometer, which was introduced into the brine inlet tube. The maximum pressure measured was 0.28 MPa which corresponds to a salt brine boiling point of 140°C. This means that the water contained in the brine evaporates at points of elevated temperature and recondenses at the upper cooler end of the tube (90°C).

Like the temperatures, the stresses prevailing on the tube surface were measured in reference boreholes using strain gauges. The measurements have shown that the first contact of the borehole wall with the tube due to rock pressure occurred after about six months. On the basis of the results obtained in an identical

preliminary test [13], complete closure of the 1 mm wide annular gap would have taken place after approximately twelve months.

3.2.3 Post-test examination of the specimens

When the specified test duration was reached, the tubes were retrieved by overcoring. The salt drilling cores obtained (1 m length, 120 mm outside diameter) were cut into two half shells and visual inspection of the tubes and the drilling cores was made. The tubes were freed from the adhering salts and corrosion products by mechanical treatment, cleaning in H_2O at 60°C and pickling in diluted HCl. Then the tubes were cleaned in distilled H_2O and alcohol. After drying, the tubes were subjected to post-test examination for corrosion attack by means of surface profilometry and metallography.

3.2.4 Results

Visual inspection of the drilling cores indicated that the 1 mm annular gap between the tubes and the borehole wall existing at the beginning of the experiments had completely closed. In the experiments with brine at 90°C-200°C, dissolved salt was clearly visible below the ceramic insulation in the cooler upper part of the tube (T = 90°C). This was attributed to the condensation of water vapor. The microscopic evaluation of microsections taken from the drilling cores revealed that the heat and the brines added caused changes in the surrounding rock salt. Zones of crystallized brine, corroded grain boundaries of rock salt, etc. were observed.

The surface profiles and the metallographic examinations of specimens show that corrosion of a non-corrosion protected cast steel tube in rock salt containing a small amount of water (0.1 wt.%) is negligibly small. Neither on the parent material nor on the EB-welds were any signs of pitting corrosion or stress corrosion cracking found. After 5.3 years of testing at 90°C-200°C, a general corrosion of about 10 µm only was observed over the initial roughness of the tube surface (30-35 µm). Figure 22 shows an optical micrograph of a cast steel tube section after exposure to rock salt.

In rock salt plus $MgCl_2$-rich Q-brine (6.3 years at 32°C), the non-corrosion protected cast steel tube also was resistant to pitting corrosion and stress corrosion cracking. However, the tube suffered from significant general corrosion with voluminous corrosion products present. This corrosion attack was non-uniformly distributed on the tube surface (see optical micrograph Fig. 23) such

that the individual tube areas exhibited significant differences in the penetration depth. This indicates that certain tube parts were exposed to a larger brine volume than others. This is attributed to the irregular distribution of the brine in the annular gap as a consequence of irregularities in the shape of the borehole and the positioning of the tube.

Figure 24 shows the maximum penetration depth of corrosion in various sections of the cast steel tubes exposed to rock salt (very small corrosion) and to rock salt plus brine (extensive corrosion). It is evident that in rock salt plus brine the greatest corrosion attack of 570 µm occurred at the lower part of the tube, while the smallest of 180 µm existed at the top of the tube. These values determined after 6.3 years of test duration at 32°C correspond to average corrosion rates of about 30 µm/a (top of the tube) and 90 µm/a (bottom), respectively, and are smaller than those obtained in previous studies [11] at 90°C-200°C. A possible explanation for the smaller corrosion of the upper tube part is the lowering of the brine level in the borehole during the test period due to water consumption by the corrosion reaction with Fe. This means that the upper tube part was not exposed to brine during the entire test period.

The Ni-resist tubes tested in rock salt (5.3 years at 90°C-200°C) and the Ti 99.8-Pd tube examined in rock salt plus NaCl-brine (2.8 years at 90°C-200°C) were found to be resistant to general and local corrosion as well as to stress corrosion cracking. For Ni-resist D4, very little general corrosion of about 5-10 µm was detected after about 5 years of testing. In case of Ti 99.8-Pd, corrosion attacks were found neither on the parent material nor on the TIG-welded bottom of the tube. Figures 25 and 26 show optical micrographs of Ni-resist and Ti 99.8-Pd tubes after in-situ testing.

The examination of the cast steel tubes provided with a corrosion protection of Ti 99.8-Pd and Hastelloy C4, respectively, has not shown any changes on the surface of the plating materials by corrosion attacks in rock salt or rock salt plus NaCl-brine. Neither on the mechanically finished surface nor on the hot-rolled and electron beam welded sheet metal surface were any signs of corrosion observed. Even the crack produced by a steel needle in order to simulate severe conditions due to handling of the containers did not stimulate a corrosion attack. Figures 27 and 28 show optical micrographs of the plating materials Ti 99.8-Pd and Hastelloy C4 after testing in rock salt and rock salt plus brine.

4. STRESS CORROSION CRACKING TESTING OF CARBON STEELS (ENRESA/INASMET)

The resistance of the three preselected carbon steels TStE 355, TStE 460 and 15MnNi 6.3 (see session 2.1) to stress corrosion cracking was examined in the $MgCl_2$-rich brine 1 (Q-brine, composition see Table 1) by means of the slow strain rate technique (SSRT). The experiments were performed in Hastelloy C-276 autoclaves at strain rates of 10^{-4}-$10^{-7}s^{-1}$, temperatures of 25°C, 90°C and 170°C, and an argon pressure of 13 MPa.

In order to be able to interpret the results obtained in the brine, additional comparative investigations were carried out in argon as an inert medium. Besides specimens of the parent materials, also MAG (Metal Active Gas) welded specimens simulating a possible container closure technique were tested. To evaluate the resistance of the steels to stress corrosion cracking, metallographic and scanning electron microscopic (SEM) examinations of specimens were performed in addition to the tensile experiments.

4.1 Materials and experimental

The parent materials for the TStE 355 and TStE 460 steels were hot-rolled and annealed plates, and for 15MnNi 6.3 forged and annealed disks. Information about composition and microstructure of the steels is given in session 2.1. The mechanical properties of the steels are given in Table 9.

For the MAG-welding of the specimens, filler materials (Griduct SV-8 for TStE 355, and Thyssen Union K-5 for TStE 460 and 15MnNi 6.3) were used.

For the slow strain rate tests, round specimens of 6 mm diameter and 30 mm gauge length were machined and finished with 1000 grade emery paper. The TStE 355 and TStE 460 specimens were machined in transverse direction to the rolling direction of the plates, those of 15MnNi 6.3 in the radial direction of the forged disks. Specimens of the welded joints were taken in the transverse sense.

For the experiments constant extension rate tensile testing machines of 50 KN capacity and selectable crosshead spead within the range of 0.1 to 10^{-6} mm/s were used. The specimens were located in the Hastelloy C-276 autoclaves with one end being attached to a fixed frame and the other to the pull rod. Fittings made of ZrO_2 ensured the electrical insulation of the specimens. Then, the autoclaves were filled either with Q-brine or argon, closed, pressured and heated. Once the testing temperature and pressure were reached, the specimens were

pulled until fracture at the selected actuator displacement speed. A general view of the test equipment is shown in Fig. 29.

Load, position, time and temperature data were continuously logged by the microprocessor that controls the testing machine. After each test, the elongation (E), reduction of area (R.A.), energy, yield strength (Y.S.), maximum load, and true stress at fracture were calculated.

4.2 Results

Test temperature of 25°C

The results of the slow strain rate tests obtained for MAG-welded and unwelded steel specimens in argon and Q-brine at 25°C and strain rates of 10^{-4}-$10^{-7}s^{-1}$ are shown in Figs. 29-33. All values are the average of at least two experiments. At the two slowest strain rates ($10^{-6}s^{-1}$ and $10^{-7}s^{-1}$), the elongation, reduction of area and true stress at fracture of the unwelded specimens are lower in brine than in argon. In the case of the welded specimens, the values of these parameters are about the same in both media. The values of the yield strength, maximum load and energy in Q-brine are very close to those in argon for both welded and unwelded specimens.

In the metallographic examinations, a non-uniform general corrosion due to repeated breaking of the corrosion surface layer was observed for the forged 15MnNi 6.3 steel after testing in Q-brine. Secondary cracks typical for stress corrosion cracking were not observed for all steels neither in argon nor in brine (Figs. 34 and 35). This is true both for welded and unwelded steel specimens. The fracture of the welded specimens was always located in the unwelded region, except for the fastest strain rate of $10^{-4}s^{-1}$. In this case, the fracture was located sometimes in the weld. The absence of secondary cracks is an indication that the loss of ductility of the steels after testing in brine at very slow strain rates cannot be attributed to stress corrosion cracking. For this effect another mechanism such as embrittlement could be responsible.

The scanning electron microscopic (SEM) examinations show ductile fracture surfaces for all steels after testing in argon and brine (Fig. 36). Only at the slowest strain rate some small brittle areas are seen (Fig. 37).

Test temperature of 90°C

The results of the slow strain rate tests on welded and unwelded steel specimens in argon and brine at 90°C and various strain rates (10^{-4}-$10^{-7}s^{-1}$) are shown in Figs. 38-41). A clear decrease of the elongation, reduction of area, energy and true stress at fracture occurs for all steels after testing in Q-brine in comparison to argon. The values of the yield strength and maximum load in brine are very close to those obtained in argon. The loss of ductility of the steels at 90°C is bigger than that at 25°C and is in agreement with the results reported by Westerman et al.[7] The results obtained for the welded specimens show that the reduction of ductility in brine is very similar to that observed for the unwelded specimens.

In the metallographic examinations of steel specimens tested in Q-brine, a non-uniform general corrosion due to repeated breaking of the corrosion surface layer was observed for all steels both in the welded and unwelded conditions (Fig. 42). Secondary cracks typical for stress corrosion cracking were not observed for the hot-rolled steels TStE355 and TStE 460 under any of the test conditions. Also in case of the forged steel 15MnNi 6.3, no signs of sensitivity to stress corrosion cracking were found in Q-brine at 90°C and strain rates up to $10^{-6}s^{-1}$. However, at the slowest strain rate of $10^{-7}s^{-1}$, extensive lateral secondary cracks indicating stress corrosion cracking were observed, besides a non-uniform corrosion (Figs. 43 and 44). The fracture of welded specimens was always located in the unwelded region.

The SEM fracture surface examinations show a change from a fully ductile fracture, when specimens are tested in argon, to a more brittle one when tests are performed in Q-brine. The brittle nature of the fracture surface becomes greater as the strain rate is slower. Figures 45, 46 and 47 show brittle features on the fracture surface of specimens tested at a strain rate of $10^{-7}s^{-1}$. Figure 45 shows a transgranular fracture mode, whereas Fig. 46 shows the intergranular appearence of the fracture surface.

Test temperature of 170°C

The results of the slow strain rate tests obtained for welded and unwelded steel specimens in argon and brine at 170°C and various strain rates (10^{-4}-$10^{-7}s^{-1}$)) are shown in Figs. 48-51. Compared to the values in argon, a clear decrease of the elongation, reduction of area, energy and true stress at fracture occcurs for all steels when tested in brine. Yield strength and maximum load do not show

significant differences in the two media. The loss of ductility at 170°C is greater than that observed at 25°C and 90°C.

The metallographic examinations show areas of non-uniform corrosion for all steels after testing in brine, as in the experiments at 90°C. On the fracture surface of TStE 355 specimens no secondary cracks were observed which indicates the resistance of this steel to stress corrosion cracking. However, in the case of the 15MnNi 6.3 forged steel and to a less degree of the TStE 460 hot-rolled steel, secondary cracks were observed after testing in the brine at the strain rate of $10^{-5}s^{-1}$. The TStE 460 steel shows a light sensitivity to stress corrosion cracking (Figs. 52 and 53), whereas in the case of the 15MnNi 6.3 extensive secondary cracks indicate a high susecptibility to stress corrosion cracking in the brine at $10^{-5}s^{-1}$ (Fig. 54).

The SEM examinations show a fully ductile fracture surface (dimples) for all steels after testing in argon (Fig. 55). In the brine, extensive areas of brittle fracture were observed for all steels. Figures 56 and 57 show secondary cracks on the fracture surface of the TStE 460 and 15MnNi 6.3 steel specimens. The extensive lateral secondary cracking of a 15MnNi 6.3 steel specimen when tested in brine at a strain rate of $10^{-5}s^{-1}$ is shown in Fig. 58. The SEM micrograph in Fig. 59 shows brittle areas and dimples in the fracture surface of a TStE 355 specimen.

To evaluate the effect of environment and temperature on the mechanical properties of the steels, the results obtained for each parameter (e.g. elongation, reduction of area) are represented in Figs. 60-71 as ratios of the values (V) obtained in brine and argon. Ratios ($R = V_{brine}/V_{argon}$) near 1 indicate that there is no effect of medium or temperature on the mechanical properties, ratios significantly less that 1 are an indication for a strong influence. The results at 90°C and 170°C show that the reduction of area, true stress at fracture and energy are the parameter for which the effect of brine is more pronounced. At 25°C the effect of brine is lower and only noticeable for the slowest strain rate ($10^{-7}s^{-1}$). Yield strength and maximum load ratios near 1 indicate that the environment (Q-brine) has no effect on the mechanical properties of the steels.

In order to quantify and compare the resistance of the steels to stress corrosion cracking in Q-brine, the crack density on the lateral surface of the specimens, the maximum crack length, and the crack length/width ratio parameters were measured. The results obtained in the brine at 90°C and 170°C are plotted in Figs. 72-74. The values at 25°C are not plotted because no secondary cracks and no localized corrosion were observed at this temperature. It is important to mention that the term "crack" is used in a wide sense including both secondary cracks and

areas of localized corrosion due to the breaking of the oxide corrosion layer. This is the reason for the relatively high crack density for the TStE 355 steel at 90°C at the strain rate of $10^{-6}s^{-1}$. The 15 MnNi 6.3 forged steel shows the deepest cracks, mainly at $10^{-5}s^{-1}$ when tested at 170°C, and at $10^{-7}s^{-1}$ when tested at 90°C. The crack length/crack width ratio gives an idea of the sharpness of the crack and it is useful for evaluating the sensitivity of the steels to stress corrosion cracking. According to these data, the unalloyed hot rolled steel TStE 355 is the most resistant and the low-alloyed forged steel 15MnNi 6.3 the least resistant material to stress corrosion cracking in the Q-brine. The TStE 460 steel shows an intermediate behaviour.

The results of the stress corrosion cracking studies show that all steels investigated suffer a loss of ductility when tested in Q-brine at very slow strain rates. At 25°C only a very slight drop of the mechanical properties was observed, but at higher temperatures (90°C and 170°C) an important loss of ductility occurred. This loss of ductility is mainly noticed in the elongation, reduction of area, energy and true stress at fracture.

The loss of ductility of the steels in brine is attributed to the embrittling effect of the corrosion hydrogen produced on the specimen surface during the test by the reactions

$$Fe \rightarrow Fe^{2+} + 2e^{-}$$

$$2H^{+} + 2e^{-} \rightarrow 2H$$

The hydrogen produced enters the material mainly through the high stressed zones of the specimen and interacts with the microstructure resulting in a deterioration of mechanical properties specially manifested in elongation and reduction of area parameters. The amount of hydrogen produced on the specimen surface due to corrosion reactions increases with the temperature. Values of 0.003 and 0.017 $mg(H_2)/cm^2 \cdot day$ have been measured during the corrosion of TStE 355 carbon steel in Q-brine at 90°C and 170°C, respectively.

The loss of ductility of the steels in the $MgCl_2$-rich Q-brine at slow strain rates is interpreted as a Hydrogen Assisted Stress Cracking (HASC). Only in the case of the 15MnNi 6.3 and TStE 460 steels in which secondary cracks have been found the loss of ductility is also due to stress corrosion cracking.

5. CONCLUSIONS

In salt brines relevant for a rock-salt repository, the carbon steels investigated (TStE 355, TStE 460 and 15MnNi 6.3) are resistant to pitting corrosion and the linear rates of general corrosion at 150°C-170°C imply corrosion allowances acceptable for thick-walled containers. Under the test conditions applied, corrosion allowances of about 11 mm in NaCl-rich brine and 60 mm in $MgCl_2$-rich brines, respectively, are needed for containers made of the unalloyed TStE 355 steel with a service life of e.g. 300 years.

Comparative corrosion studies on the TStE 355 steel in the vapor and in the liquid phase of an $MgCl_2$-rich brine (T=170°C) show that the vapor-phase corrosion (10 µm/a) is significantly lower that the liquid-phase corrosion (199 µm/a).

A gamma dose rate of 10 Gy/h does not increase the corrosion rate of the TStE 355 steel in NaCl-rich brine at 150°C. In $MgCl_2$-rich brines, the corrosion rate in the irradiated environment is a factor of about 1.5 higher than in the unirradiated system.

Submerged are welding (SAW) does not influence the corrosion behaviour of the low-alloyed steels TStE 460 and 15MnNi 6.3 in NaCl-rich brine. In $MgCl_2$-rich brines, however, several local corrosion attacks in the heat-affected zone of the SAW steel specimens were observed. Thus, the application of this welding technique for the container closure is not recommended.

The results of the in-situ corrosion studies show that corrosion of cast steel, Ni-resist D4, Ti 99.8-Pd and Hastelloy C4 in rock salt up to 200°C (normal operating conditions of a repository) is negligible small. The same is true for the above-mentioned materials (metal sheets and tubes) up to 200°C in the two-phase system of rock salt plus NaCl-rich brine simulating accident conditions in a repository. In rock salt plus $MgCl_2$-rich brine, the cast steel tube suffers from extensive non-uniform general corrosion. However, the maximum corrosion rate of about 90 µm/a implies a technically acceptable corrosion allowance for a thick-walled container.

According to the results obtained from the slow strain rate tests, the unalloyed TStE 355 steel (hot-rolled and annealed) is resistant to stress corrosion cracking (SCC) in the $MgCl_2$-rich test brine up to 170°C. For the low-alloyed TStE 460 steel (hot rolled and annealed) no sensitivity to SCC was found at 25°C and 90°C, but at 170°C and the strain rate of $10^{-5}s^{-1}$ a slight susceptibility to SCC was observed. The forged and annealed low-alloyed 15MnNi 6.3 steel is clearly sensitive to SCC in the brine both at 90°C and $10^{-7}s^{-1}$, and at 170°C and $10^{-5}s^{-1}$. All steels investigated

suffer a loss of ductility in the brine at the slow strain rates of 10^{-4}-$10^{-7}s^{-1}$ compared to argon which is likely due to hydrogen embrittlement. However, this effect does not appear to be serious, as the residual mechanical properties, e.g. the elongation and the reduction of area are relatively high.

Generally, it can be stated that the corrosion results obtained in this study confirm the promising nature of the unalloyed TStE 355 steel and the alloy Ti 99.8-Pd for the production of long-lived containers for heat-generating wastes. For the final evaluation of these materials for long-lived containers, however, further investigations are needed. These involve above all the clarification of questions relating to the synergestic effect of salt impurities and radiolytic products on corrosion at high temperature as well as the examination of the influence of pH and welding on the corrosion process in brines. The suitability of the Cr-Mo-Ni alloy Hastelloy C4 and Ni-resist D4 as material for disposal containers in rock salt must be doubted because of their susceptibility to local corrosion in $MgCl_2$-rich brines observed in previous work [13].

ACKNOWLEDGMENTS

The authors thank Prof. Dr. J. I. Kim for reviewing this papers, Mrs. V. Madina and Mrs. R. Weiler for the technical assistance, and the Commission of the European Union, Brussels, Belgium, for supporting this work.

6. REFERENCES

[1] E. Smailos, "Korrosionsuntersuchungen an ausgewählten Werkstoffen als Behältermaterial für die Endlagerung von hochradioaktiven Abfallprodukten in Steinsalzformationen", KfK 3953 (1985).

[2] E. Smailos, W. Schwarzkopf, R. Köster et al., "Corrosion Testing of Selected Packaging Materials for Disposal of High-Level Waste Glass in Rock Salt Formations", KfK 4723 (1990).

[3] E. Smailos, and R. Köster, "Corrosion of HLW Packaging Materials in Disposal Relevant Salt Brines", Proc. of the Int. Conference on High-Level Radioactive Waste Management," Las Vegas, Nevada, USA, April 12-16, 1992, Vol. 2, 1992, p. 1676.

[4] R.G. Bates, B.R. Staples, and R.A. Robinson, "Ionic Hydration and Single Ion Activities in Unassociated Chlorides at High Ionic Strength," Analytical Chemistry 42, 8, 867 (1970).

[5] G.H. Jenks, "Radiolysis and Hydrolysis in Salt-Mine Brines", ORNL/TM-3717, Oak Ridge National Laboratory (1972).

[6] B. Kienzler, E. Smailos, and R. Köster, "Statistical Evaluation and Forecasting of Steel Corrosion Data," SAS European Users Group, International (SEUGI 91) Symposium, Amsterdam, June 11-14, 1991.

[7] R.E. Westerman, J.H. Haberman et al., " Corrosion and Environmental-Mechanical Characterization of Iron-Base Nuclear Waste Package Structural Barrier Materials", PNL Report No. 5426 (1986).

[8] E. Smailos, W. Schwarzkopf, B. Kienzler, and R. Köster, "Corrosion of Carbon-Steel Containers for Heat-Generating Nuclear Waste in Brine Environments Relevant for a Rock-Salt Repository," Mat. Res. Soc. Symp. Proc., C.G. Sombret, ed., Vol. 257, 399 (1992).

[9] W. Schwarzkopf, E. Smailos, R. Köster, "Langzeitbeständige Korrosions-schutzumhüllung für dicht verschlossene Gebinde mit hochradioaktivem Inhalt", DE-OS 34 47 278 (Juni 1986).

[10] W. Schwarzkopf, R. Köster, "Längszylindrischer Behälter für die Endlagerung von einer oder mehreren mit hochradioaktiven Abfällen gefüllten Kokillen", DE-OS 36 10 862 (Oktober 1987).

[11] W. Schwarzkopf, E. Smailos, and R. Köster, "In-Situ-Corrosion Studies on Cast Steel for a High-Level Waste Packaging in a Rock-Salt Repository", Mat. Res. Symp., Proc. Vol. 127, pp. 411-418, Materials Research Society (1988).

[12] E. Smailos, W. Schwarzkopf, J.A. Gago, I. Azkarate, "Corrosion Studies on Selected Packaging Materials for Disposal of Heat-Generating Radioactive Wastes in Rock - Salt Formations," KfK 5011 (1992).

[13] E. Smailos, W. Schwarzkopf, R. Köster, "Corrosion Behaviour of Container Materials for the Disposal of High-Level Wastes in Rock Salt Formations", Nuclear Science and Technology, CEC-Report EUR 10400 (1986).

Table 1 : Test conditions for steels in the laboratory-scale corrosion experiments (maximum test duration : 600 days)

Steel	Corrosion medium	V/S (ml/cm^2)	T (°C)	D (Gy/h)
TStE 355 (unalloyed)	brines 1 ,2 ,3 (liquid phase)	2 : 1	150	0;10
	brine 1 and brine 1 + Na_2S ($6x10^{-4}$ - $6x10^{-3}$ M/l) (liquid and vapor phase)	5 : 1	170	0
TStE 460 (low-alloyed)	brines 1,2,3 (liquid phase)	5 : 1	150	0
15MnNi 6.3 (low-alloyed)	brines 1,2,3 (liquid phase)	5 : 1	150	0

brines 1 and 2 : $MgCl_2$-rich; brine 3 : NaCl-rich

Table 2: Compositions, pH values and O_2 -contents of the salt brines used in the laboratory-scale corrosion experiments

Brine	Composition (wt.%)							
	NaCl	KCl	$MgCl_2$	$MgSO_4$	$CaCl_2$	$CaSO_4$	K_2SO_4	H_2O
1	1.4	4.7	26.8	1.4	—	—	—	65.7
2	0.31	0.11	33.03	—	2.25	0.005	—	64.3
3	25.9	—	—	0.16	—	0.21	0.23	73.5

pH (25°C): 4.6 for brine 1; 4.1 for brine 2; 6.5 for brine 3
O_2 (55°C): 0.8 mg/l for brine 1; 0.6 mg/l for brine 2; 1.2 mg/l for brine 3

Table 3: Results of linear regression analyses for the thickness reduction ($\Delta S = A+Bt$) of the TStE 355 steel in irradiated and unirradiated brines at 170°C ($V/S = 2 ml/cm^2$)

Corrosion medium	D (Gy/h)	Number of specimens	A (µm)	Standard error of A (µm)	B (µm/a)	Standard error of B(µm/a)
brine 1	0 10	16 19	8.0 34.1	2.5 10.6	47.1 72.6	2.5 11.0
brine 2	0 10	20 15	20.9 23.6	9.7 17.5	119.6 162.4	10.6 20.4
brine 3	0 10	16 18	1.3 1.6	1.0 1.1	15.3 13.5	1.0 1.8

brines 1 and 2 : $MgCl_2$-rich; brine 3 : NaCl-rich

Table 4: Results of linear regression analyses for the thickness reduction ($\Delta S = A+Bt$) of the TStE 355 steel in the test brines at 170°C ($V/S = 5 ml/cm^2$)

Corrosion medium	Phase	Number of specimens	A (µm)	Standard error of A (µm)	B (µm/a)	Standard error of b (µm/a)
brine 1	V L	12 14	5.8 24.5	2.1 8.4	10.2 199.4	3.6 15.0
brine 1 + $6x10^{-4}$ M/l Na_2S	V L	10 8	7.6 42.8	3.2 4.9	18.2 192.5	5.8 8.0
brine 1 + $3x10^{-3}$ M/l Na_2S	V L	12 8	-2.8 22.4	3.0 24.9	43.5 317.4	5.1 40.9
brine 1 + $6x10^{-3}$ M/l Na_2S	V L	12 8	4.8 44.9	3.4 14.0	20.1 203.0	5.8 23.0

V = vapor; L = liquid; test duration: 60-322 days; brine 1 : $MgCl_2$ - rich

Table 5: Results of linear regression analyses for the thickness reduction ($\Delta S = A+Bt$) of the TStE 460 and 15MnNi 6.3 steels in the test brines at 150°C ($V/S = 5 ml/cm^2$)

Steel	Brine	Number of specimens	A (µm)	Standard error of A (µm)	B (µm/a)	Standard error of B (µm/a)
TStE 460	1	12	-0.6	5.7	203.5	5.8
	2	12	85.2	8.6	65.4	8.7
	3	12	-5.9	4.3	56.3	4.4
15MnNi 6.3	1	12	47.5	9.3	117.3	9.4
	2	12	57.8	6.9	94.0	7.0
	3	12	-3.9	1.6	71.3	1.7

brines 1 and 2 : $MgCl_2$-rich; brine 3 : NaCl-rich

Table 6: Maximum penetration depth of corrosion in the HAZ +) of the submerged arc welded steels TStE 460 and 15MnNi 6.3 after 18 months of exposure to brines at 150°C

Material	Maximum penetration depth (mm)		
	Brine 1	Brine 2	Brine 3
TStE 460	2.0	2.5	0.04
15MnNi 6.3	1.9	4.0	0.05

+) heat - affected zone

Table 7: Chemical composition of the materials tested in rock salt at rock temperature (32°C) in an in-situ manner

Material	Composition (wt.%)								
	Ti	Pd	Cr	Ni	Mo	C	Si	Mn	Fe
Ti 99.8-Pd Material No. 3.7025.10	Bal.	0.18	-	-	-	0.01	-	-	0.05
Hastelloy C4 Material No. 2.4610	0.33	-	16.8	Bal.	15.9	0.006	0.05	0.09	0.05
Ni-resist D4 Material No. 0.7680	-	-	5.5	30.9	-	2.6	4.25	0.5	Bal.
Si-cast iron	-	-	-	-	-	0.72	15.0	0.62	Bal.

Table 8: Integral weight losses and corrosion rates of the materials tested in rock salt at rock temperature in an in-situ manner (test time: 9 years, T=32°C)

Material	Material condition	Weight loss (g/m^2)	Corrosion rate (µm/a)
Ti 99.8-Pd	W	-[1]	-[1]
Hastelloy C4	A W	13.39±3.1 28.73±24.4	0.17±0.04 0.37±0.31
Ni-resist D4	A	74.94±7.5	1.14±0.12
Si-cast iron	A	37.62±11.6	0.60±0.18

[1] no corrosion attack; A = as-received; W = TIG-welded

Table 9: Mechanical properties of the parent materials investigated in the slow strain rate tests

Steel		Yield strength (MPa)	Maximum load (MPa)	Elongation (%)	Reduction of area (%)
TStE 355	T	419	566	27	61
	L	427	568	28	64
TStE 460	T	505	633	24	51
	L	510	635	26	53
15MnNi 6.3	R	343	545	33	78
	Tg	340	484	29	78

T:Transversal; L: Longitudinal; R: Radial; T: Tangential

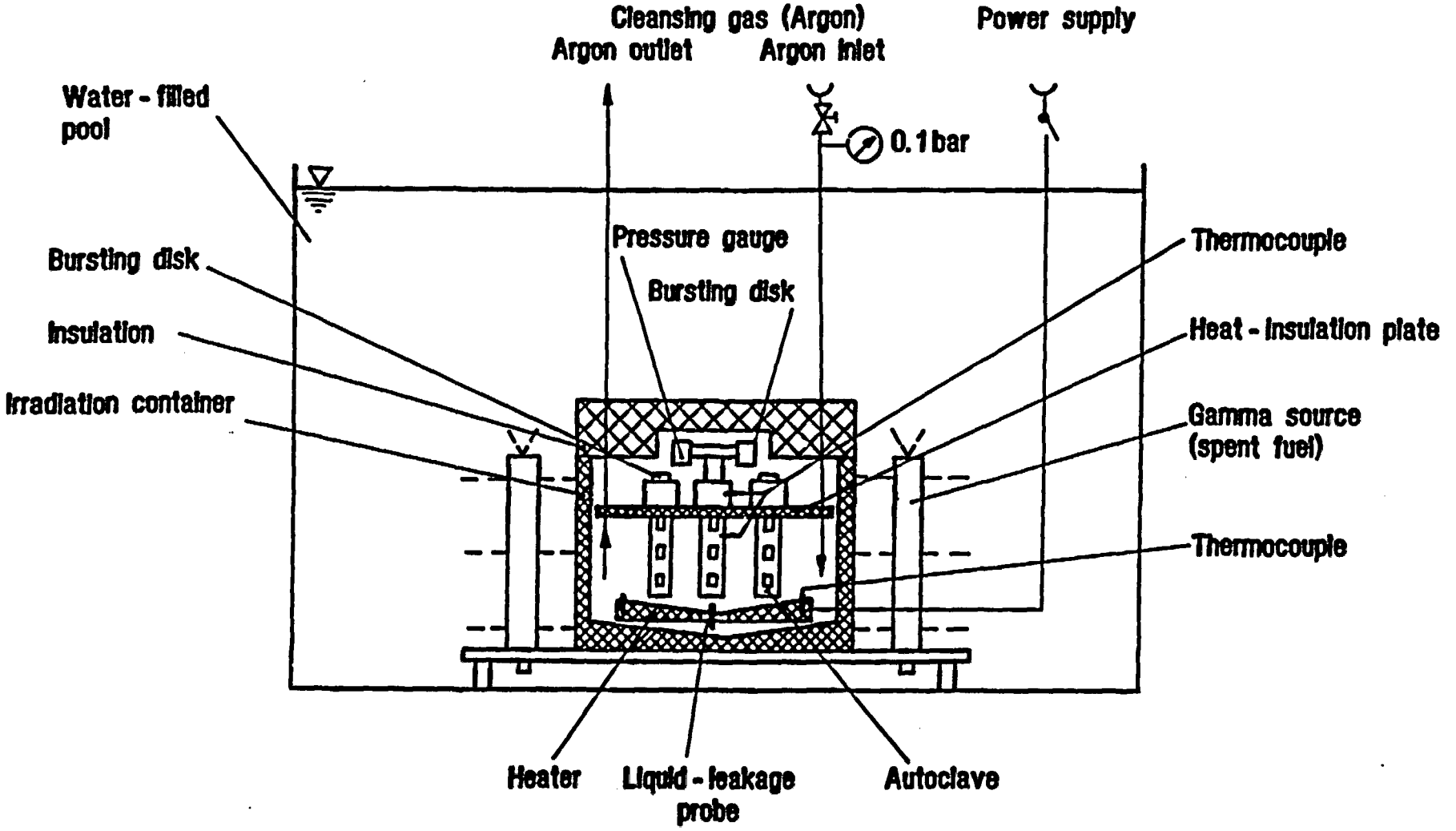

Fig. 1: Schematic of irradiation-corrosion test facility

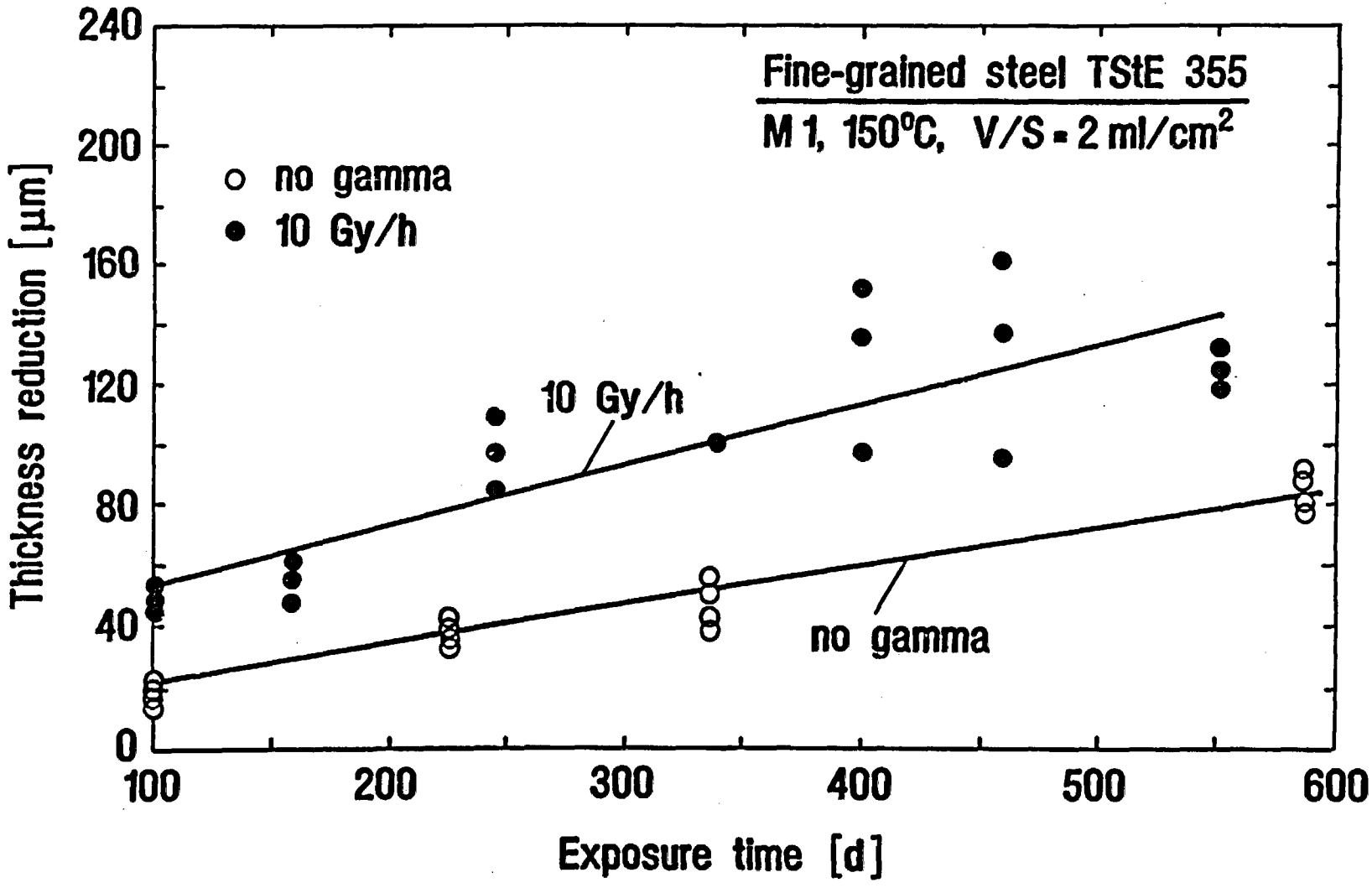

Fig. 2: Thickness reduction of the TStE 355 steel in the $MgCl_2$-rich brine 1 (Q-brine) with and without gamma radiation (T=150°C)

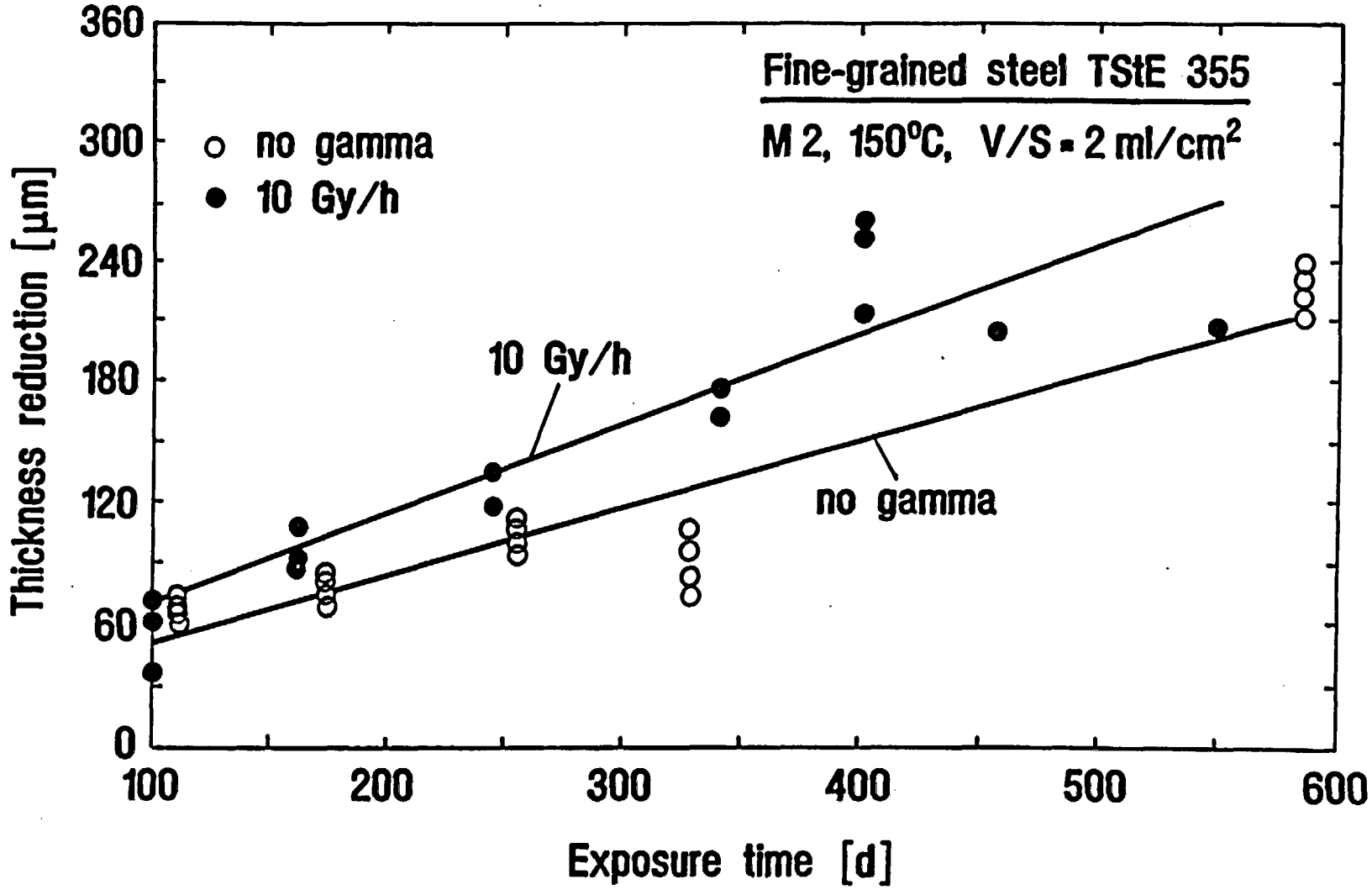

Fig. 3: Thickness reduction of the TStE 355 steel in the $MgCl_2$-rich brine 2 with and without gamma radiation (T=150°C)

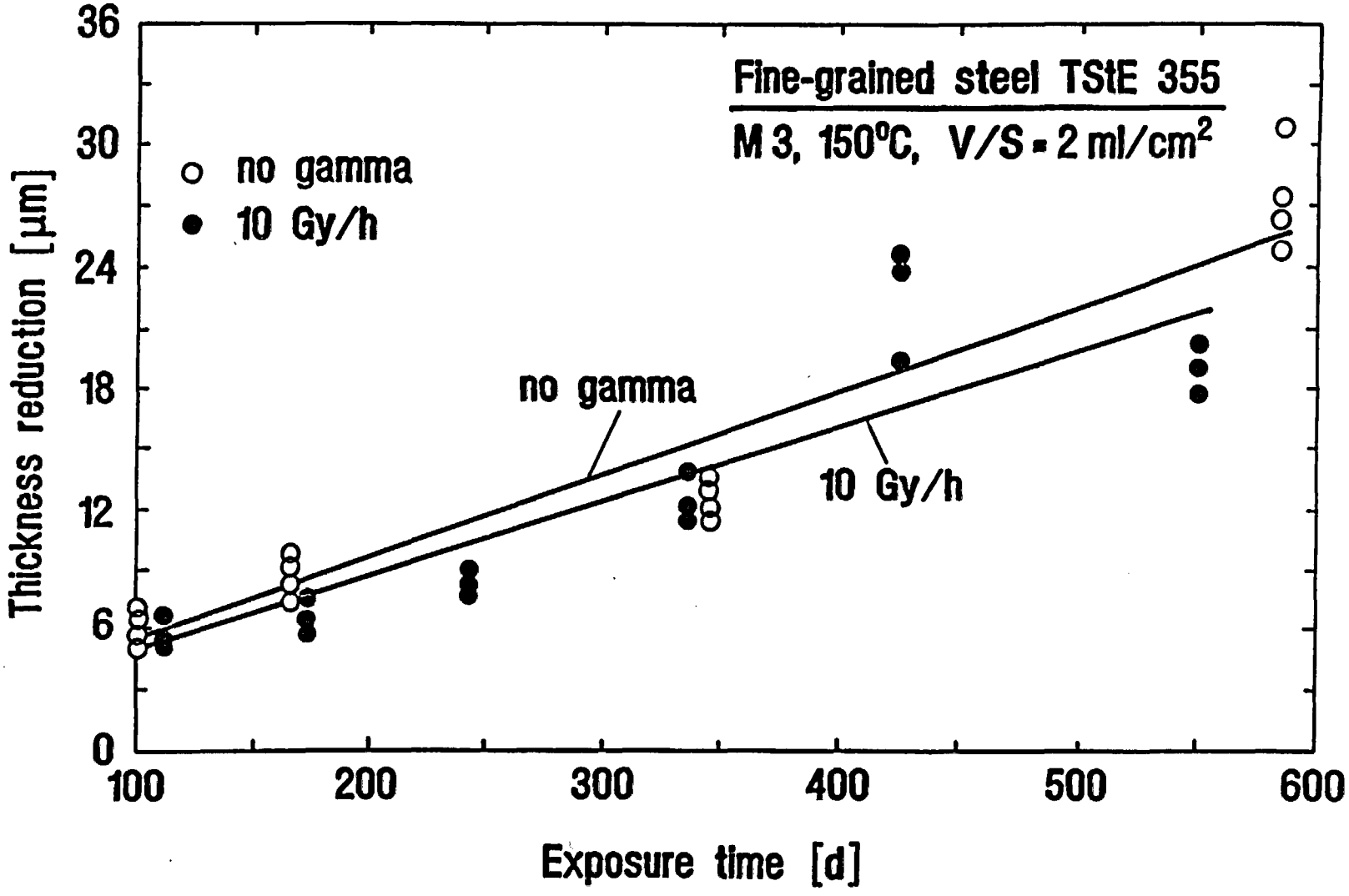

Fig. 4: Thickness reduction of the TStE 355 steel in the NaCl-rich brine 3 with and without gamma radiation (T=150°C)

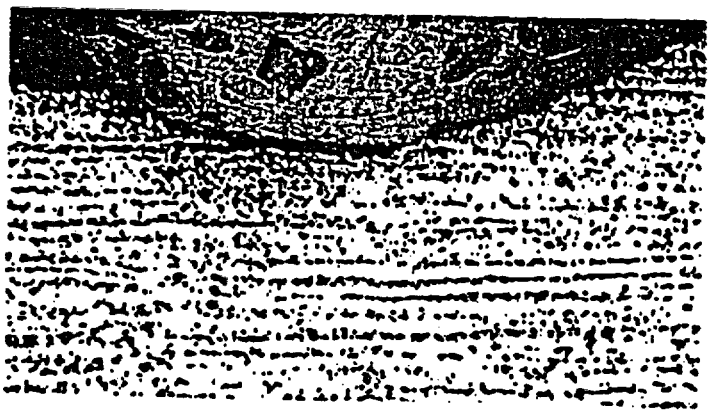

Brine 1 ($MgCl_2$-rich) X200

Brine 2 ($MgCl_2$-rich) X200

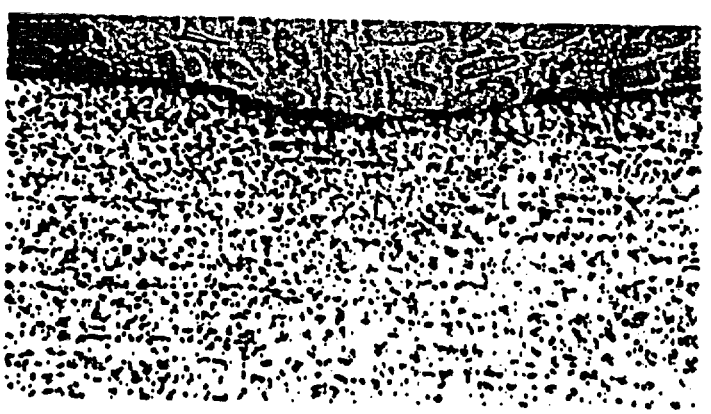

Brine 3 (NaCl-rich) X200

Fig 5: Optical micrographs of the steel TStE 355 after 166 days exposure to brines at 150°C and 10 Gy/h

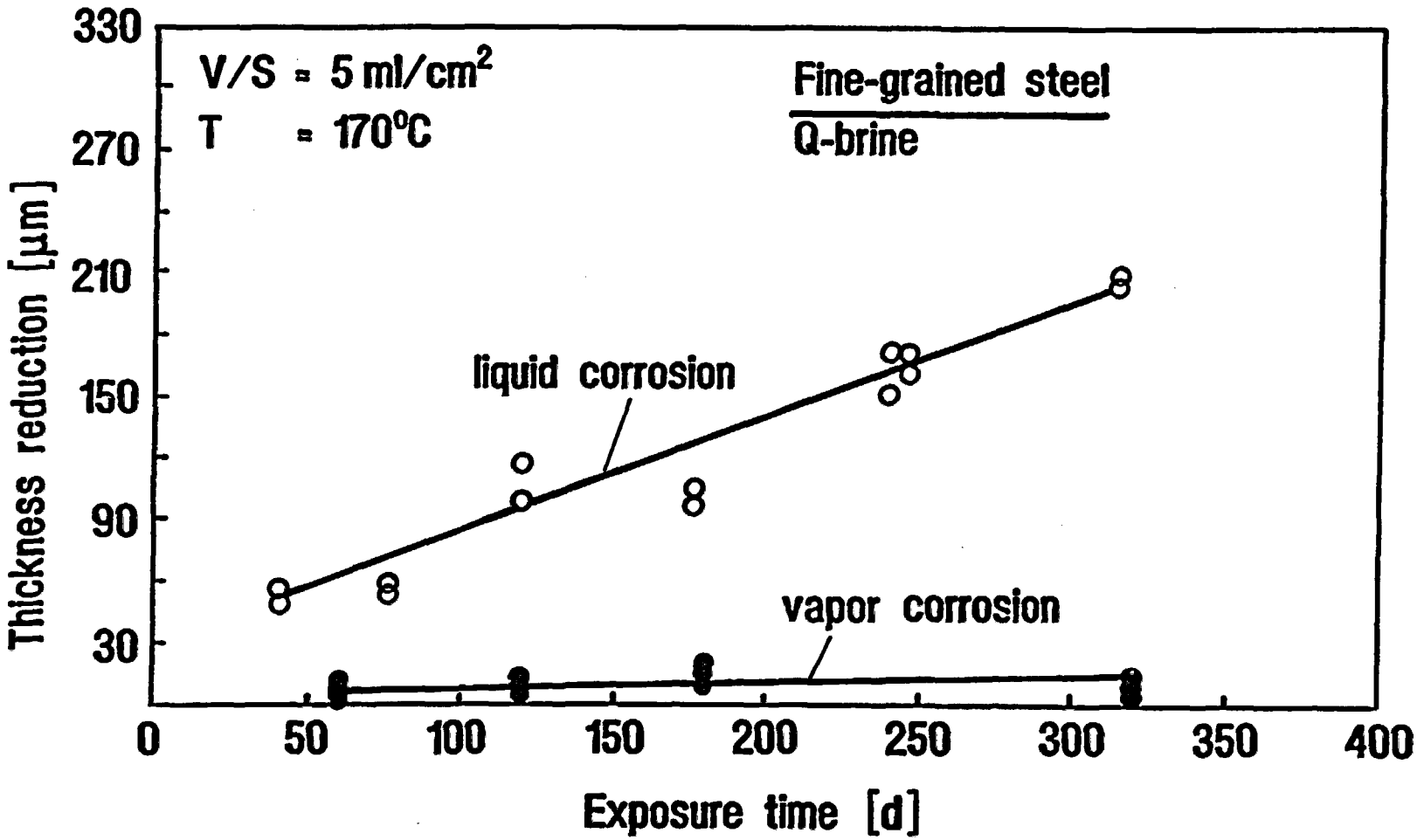

Fig. 6: Thickness reduction of the fine-grained steel TStE 355 at 170°C in Q-brine

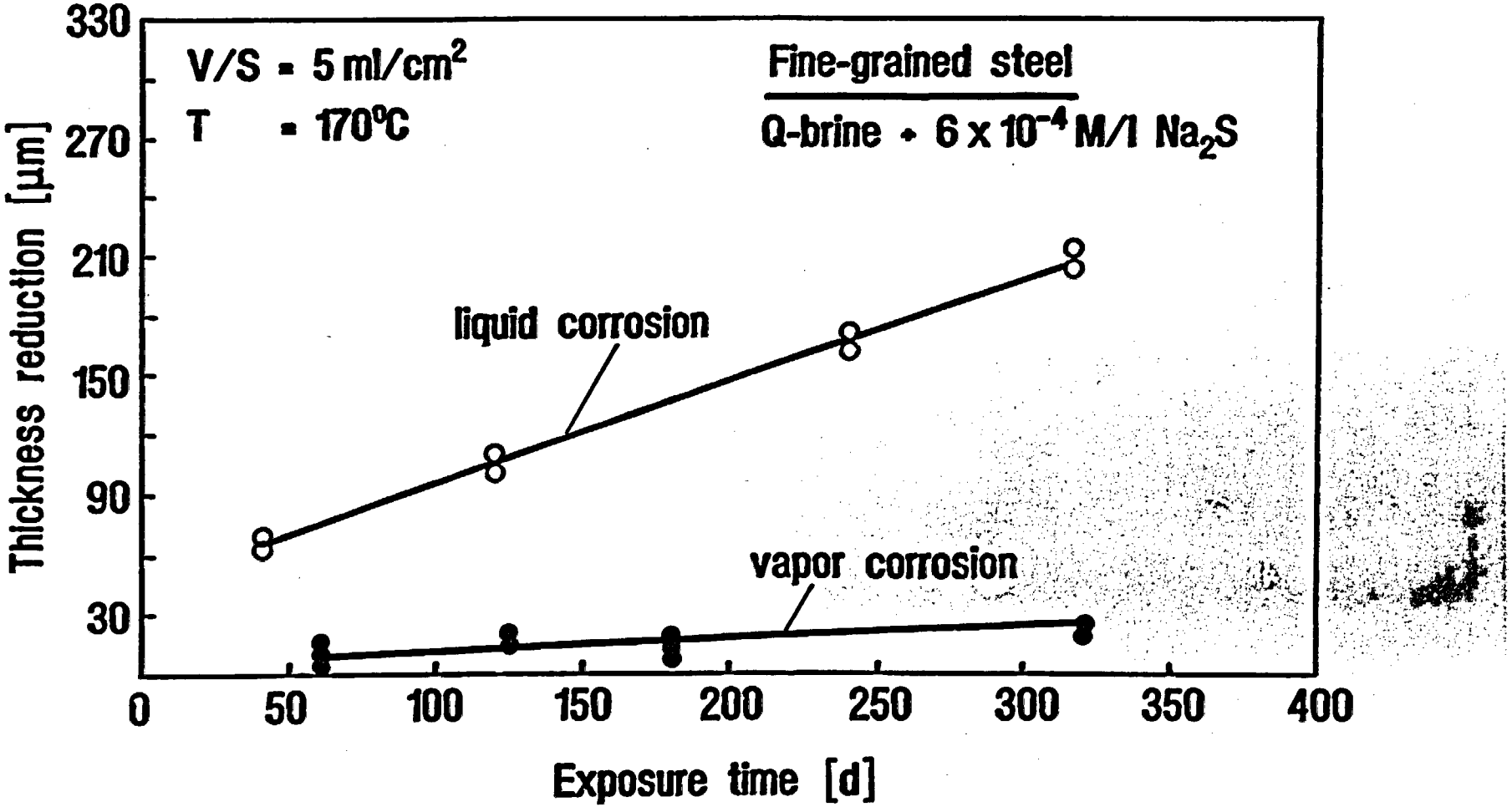

Fig. 7: Thickness reduction of the fine-grained steel TStE 355 at 170°C in Q-brine + 6x10^{-4} M/l Na_2S

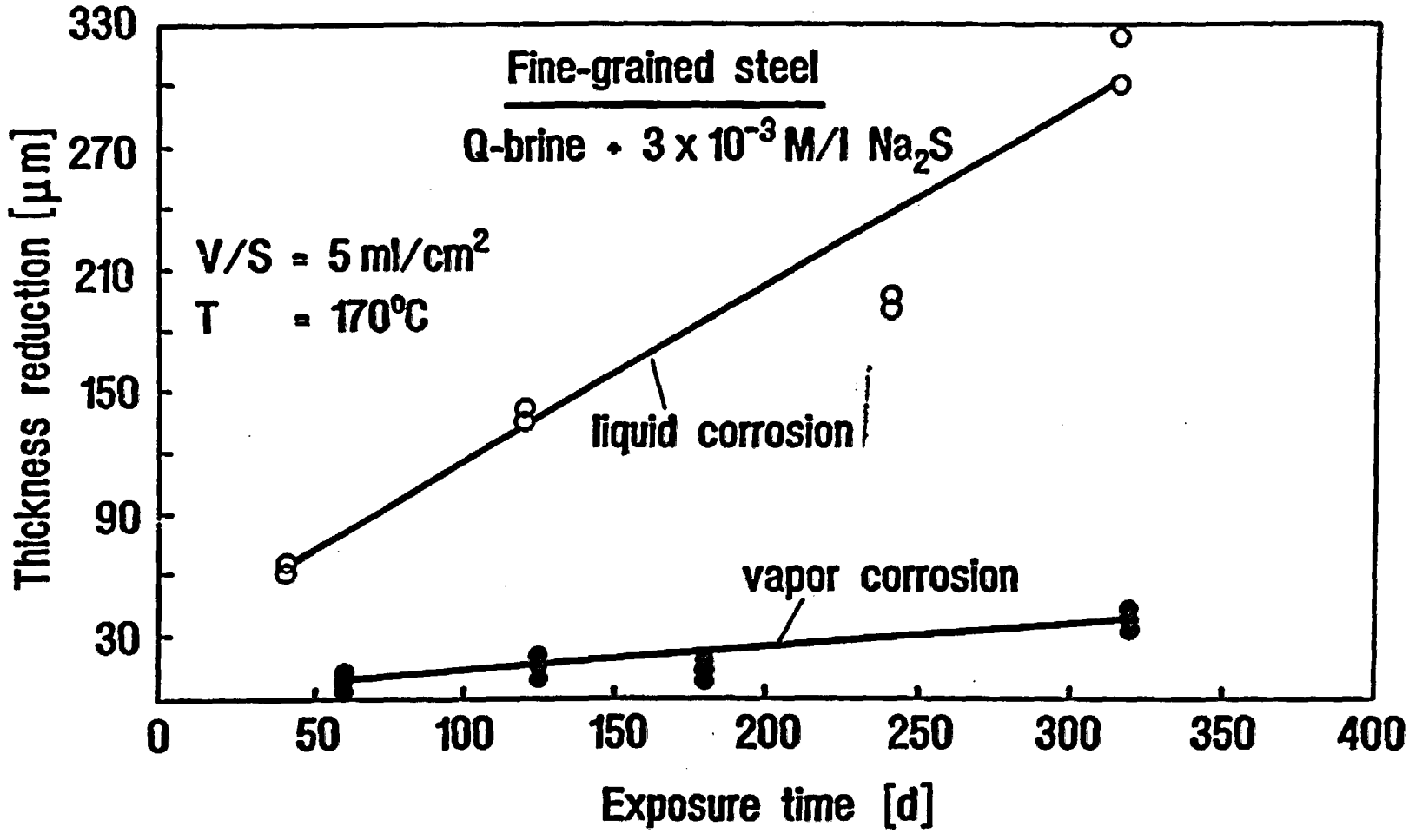

Fig. 8: Thickness reduction of the fine-grained steel TStE 355 at 170°C in Q-brine + 3x10^{-3} M/l Na_2S

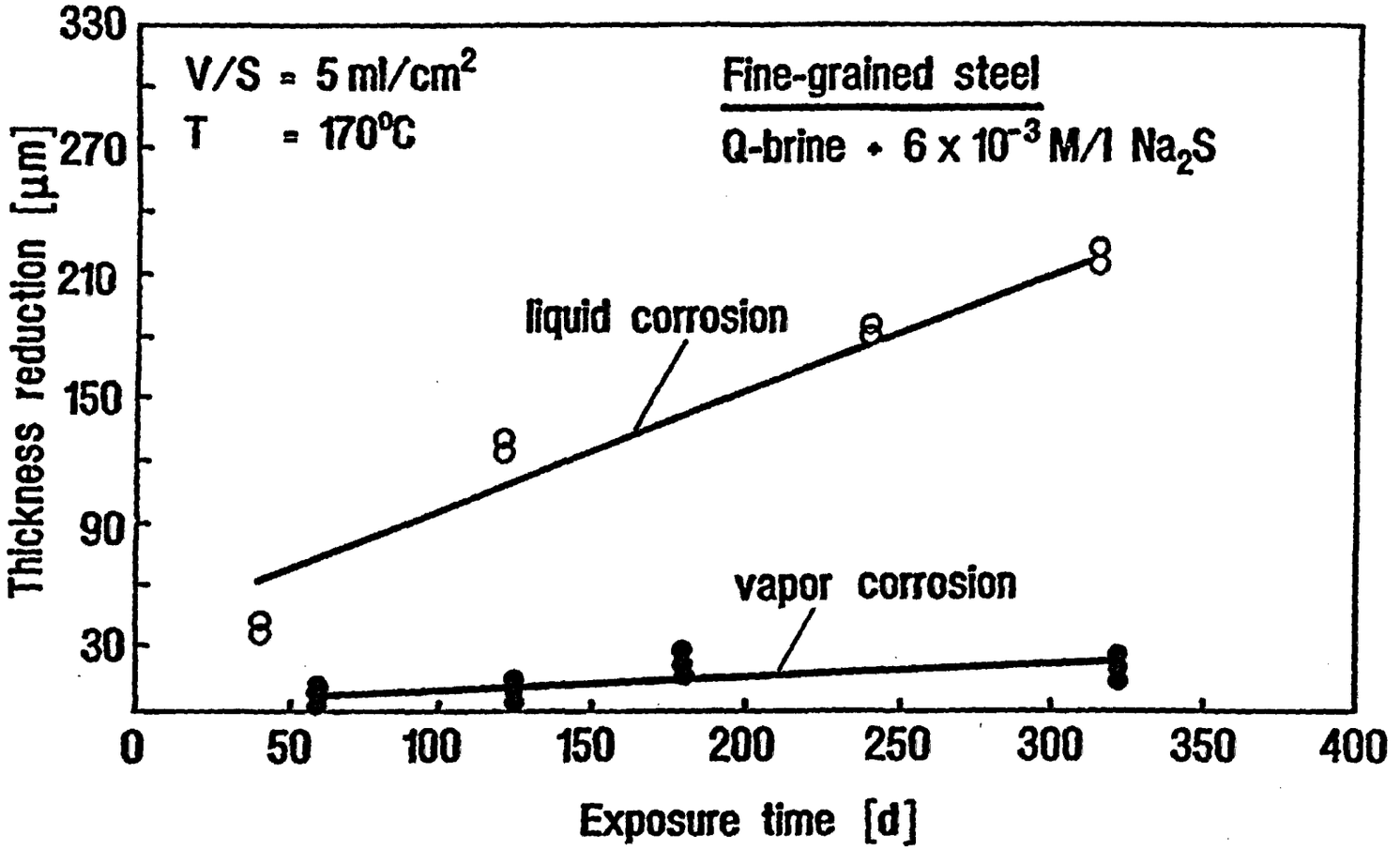

Fig. 9: Thickness reduction of the fine-grained steel TStE 355 at 170°C in Q-brine + 6×10^{-3} M/l Na_2S

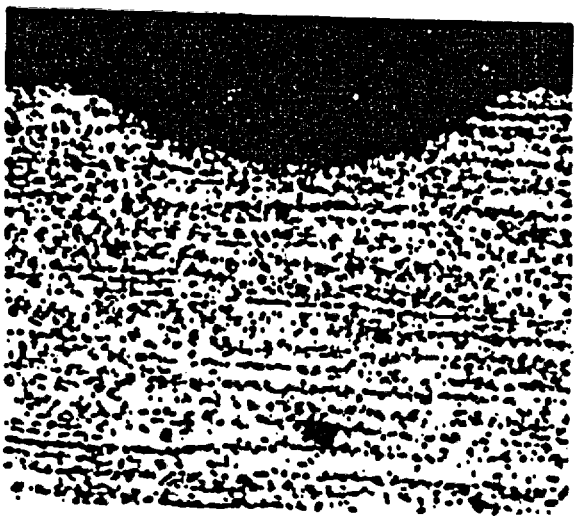

Fig. 10: Q-brine

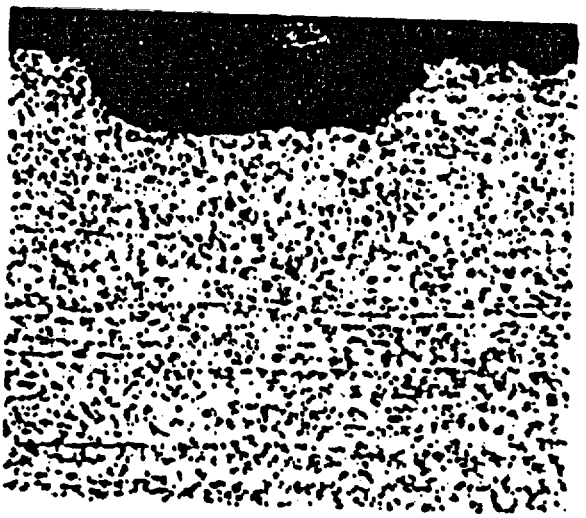

Fig. 11: Q-brine + 6×10^{-4} M/l Na_2S

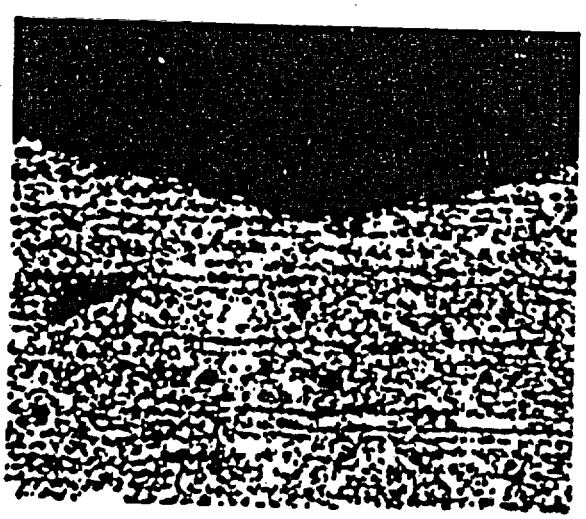

Fig. 12: Q-brine + 3×10^{-3} M/l Na_2S

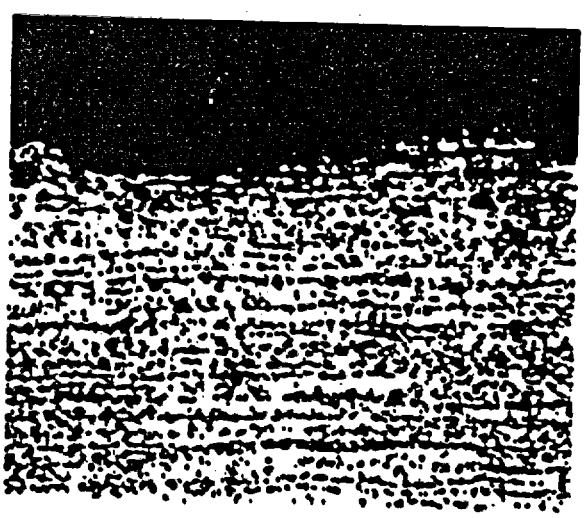

Fig. 13: Q-brine + 6×10^{-3} M/l Na_2S

Figs. 10-13: Optical micrographs of the fine-grained steel TStE 355 after 320 days exposure to the vapor phase of the test brines at 170°C (200 x)

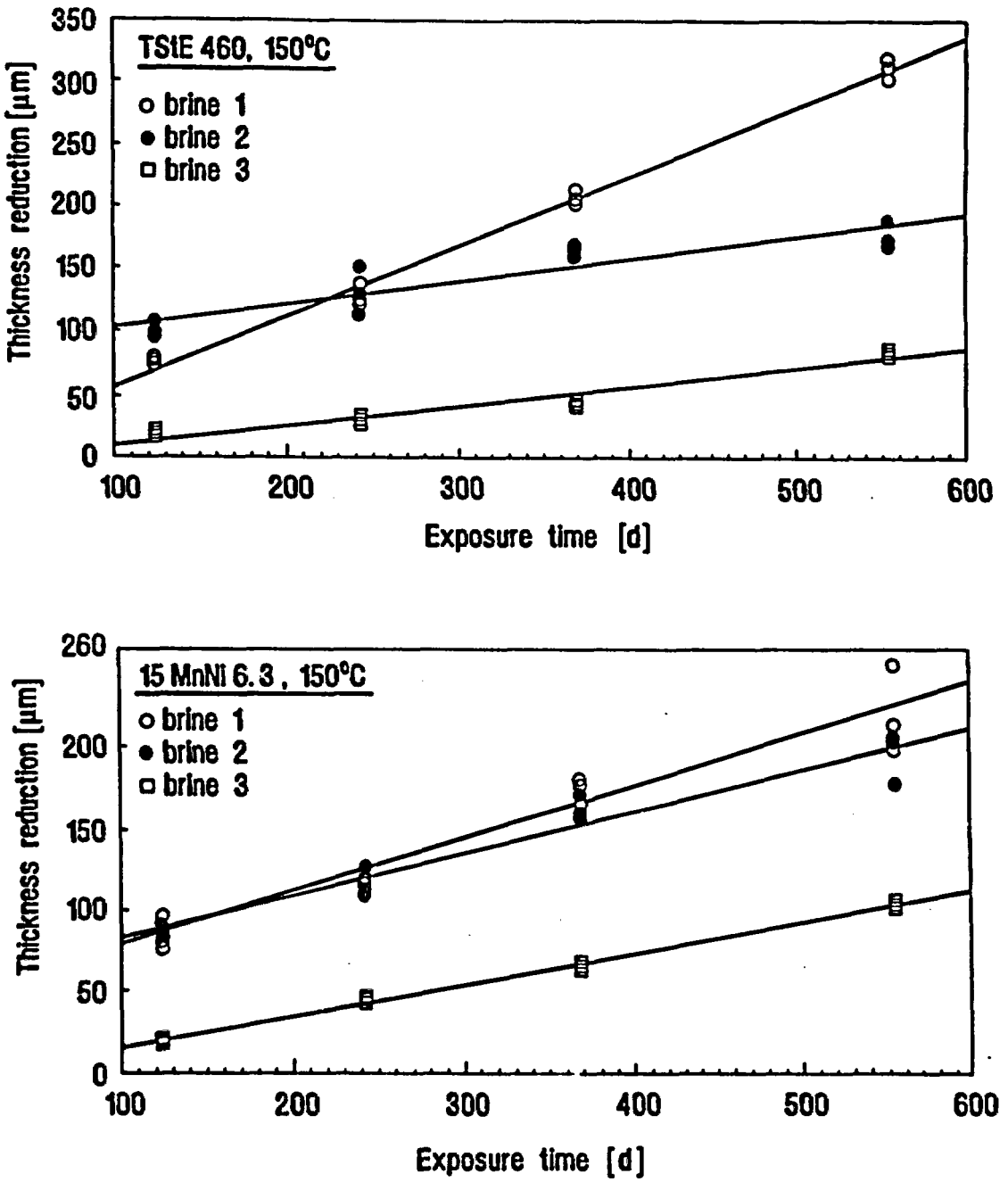

Fig.14: Thickness reduction of the steels TStE 460 and 15MnNi 6.3 in salt brines at 150°C

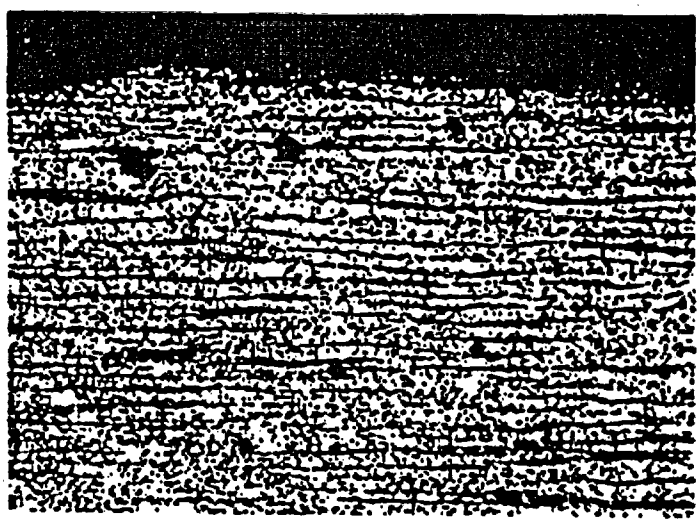

TStE 460 X 100

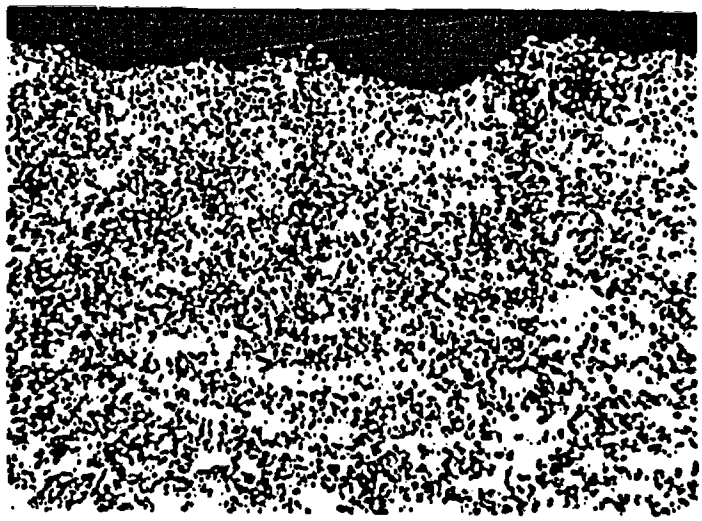

15MnNi 6.3 X 50

Fig 15: Optical micrographs of the unwelded steels TStE 460 and 15MnNi 6.3 after an 18-month exposure to brine 1 (Q-brine) at 150°C

TStE 460 X 20

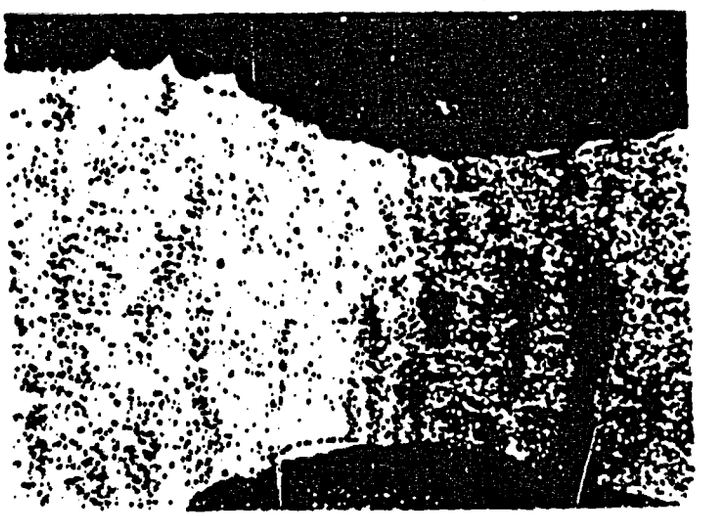

15MnNi 6.3 X 20

Fig 16: Optical micrographs of the submerged arc welded steels TStE 460 and 15MnNi 6.3 after an 18-month exposure to brine 1 (Q-brine) at 150°C

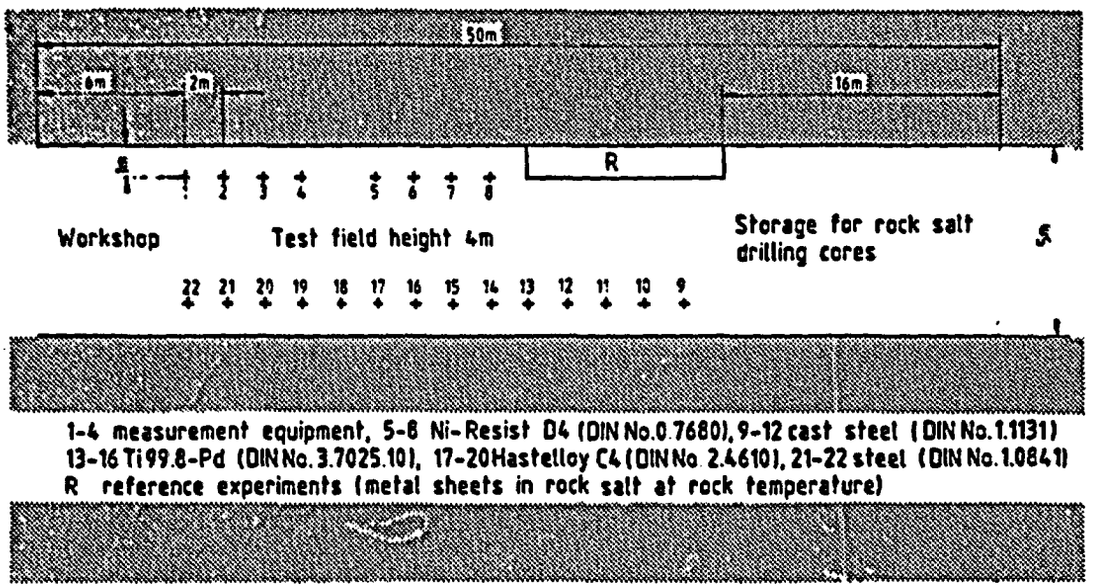

Fig. 17: Layout of the in-situ corrosion test field on the 775 m level in the Asse salt mine and arrangement of the emplacement boreholes

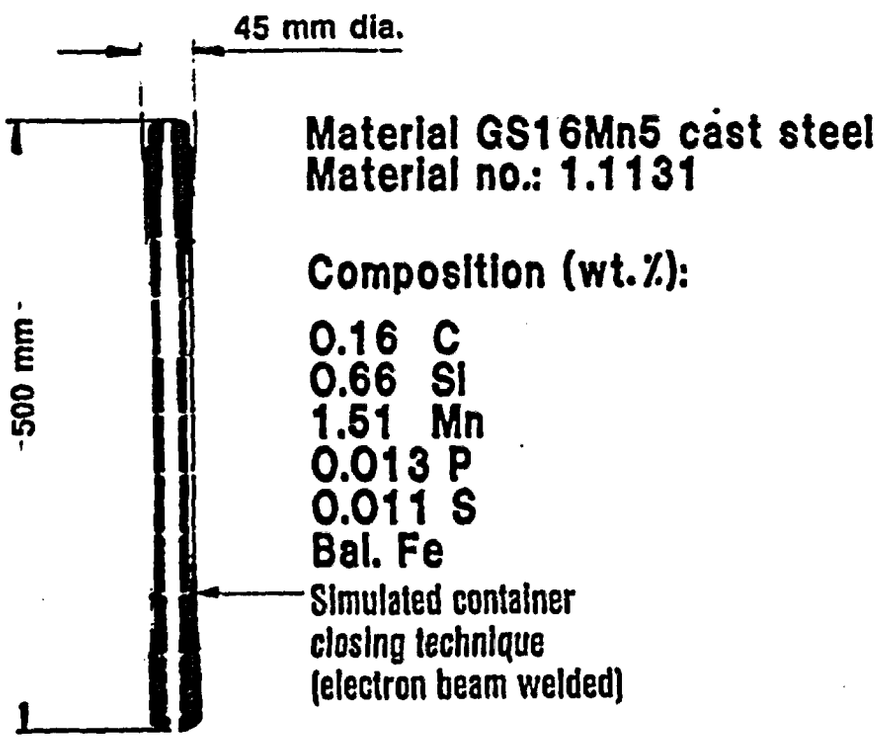

Fig. 18: Chemical composition and dimensions of a cast steel specimen

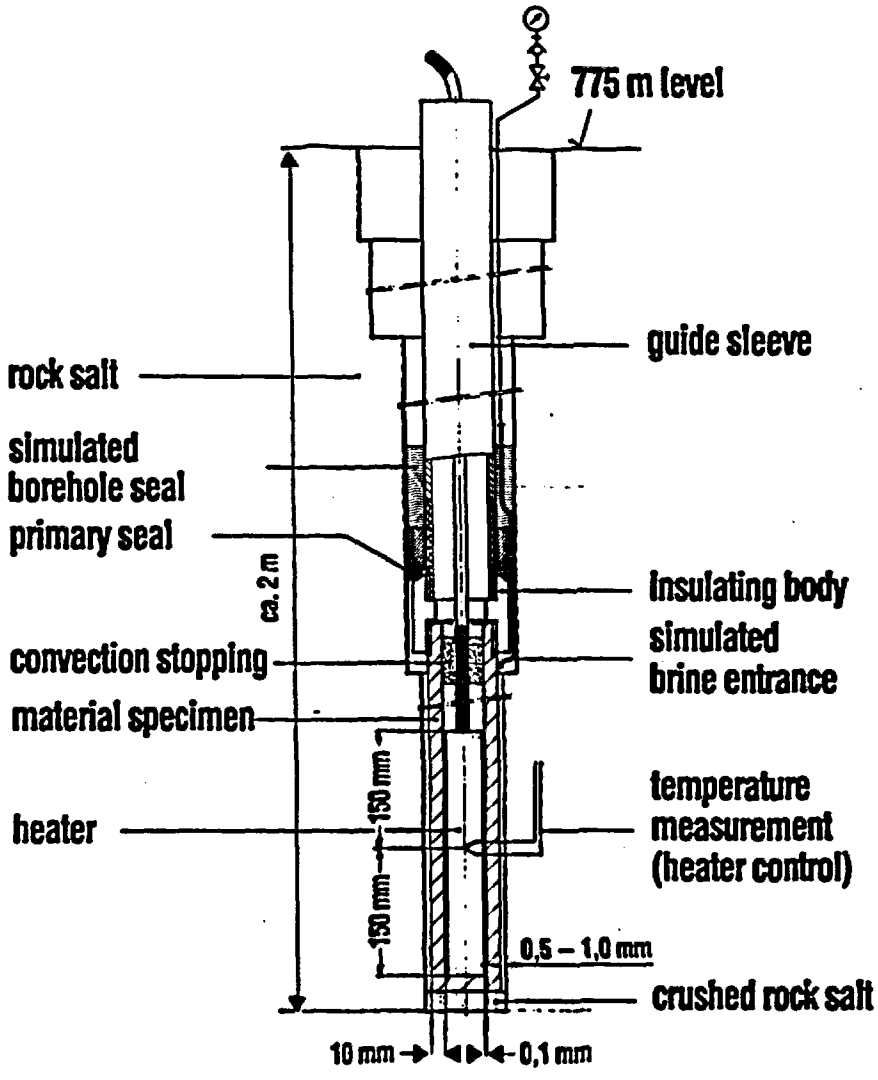

Fig. 19: Vertical cross-section of the test assembly

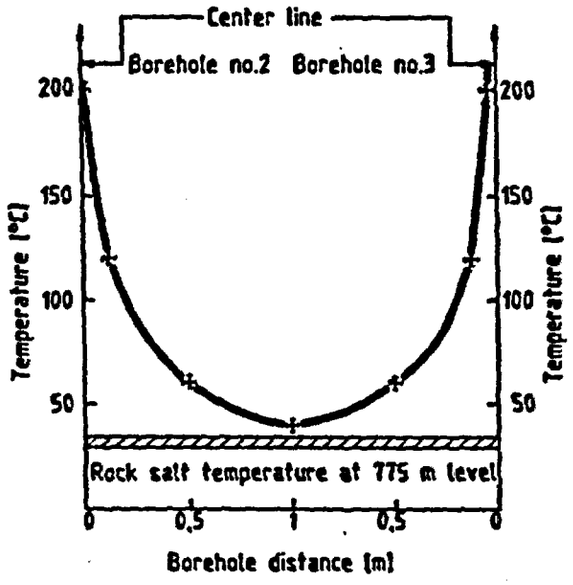

Fig. 20: Radial temperature distribution between two boreholes in the center of the heated zone

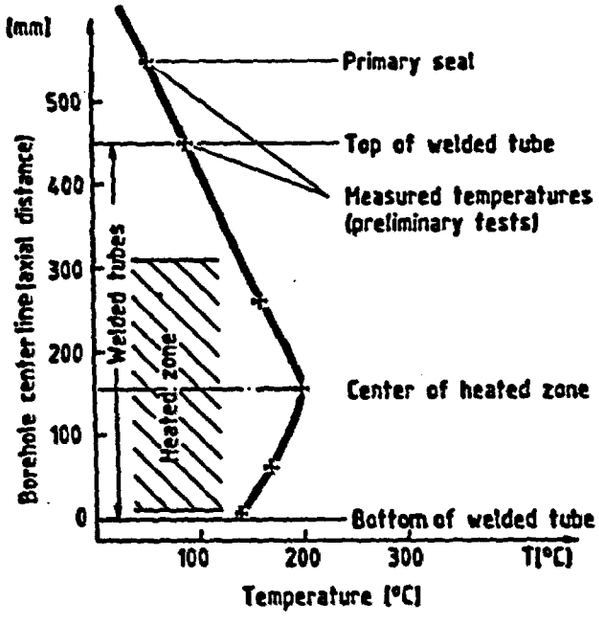

Fig. 21: Vertical temperature distribution on the welded tube wall

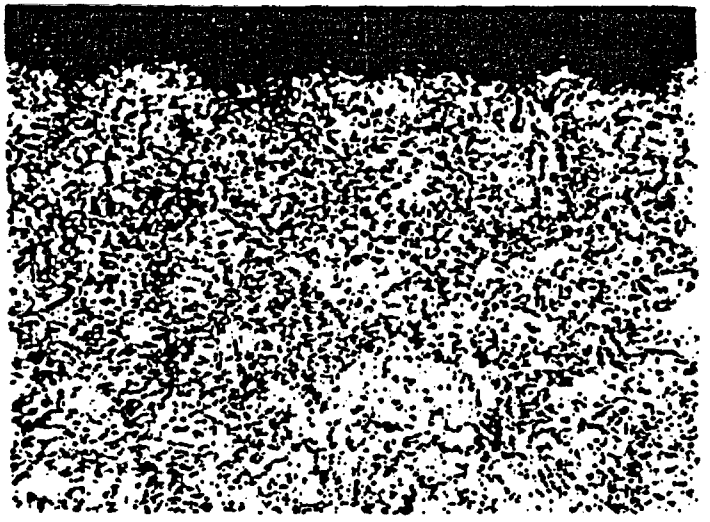

Fig. 22: Optical micrograph of a cast steel tube after 5.3 years in-situ testing in rock salt (0.1 wt.% H_2O) at 200°C (x 100)

Fig. 23: Optical micrograph of a cast steel tube after 6.3 years in-situ testing in rock salt plus 100 ml $MgCl_2$-rich Q-brine at 32°C (x 100)

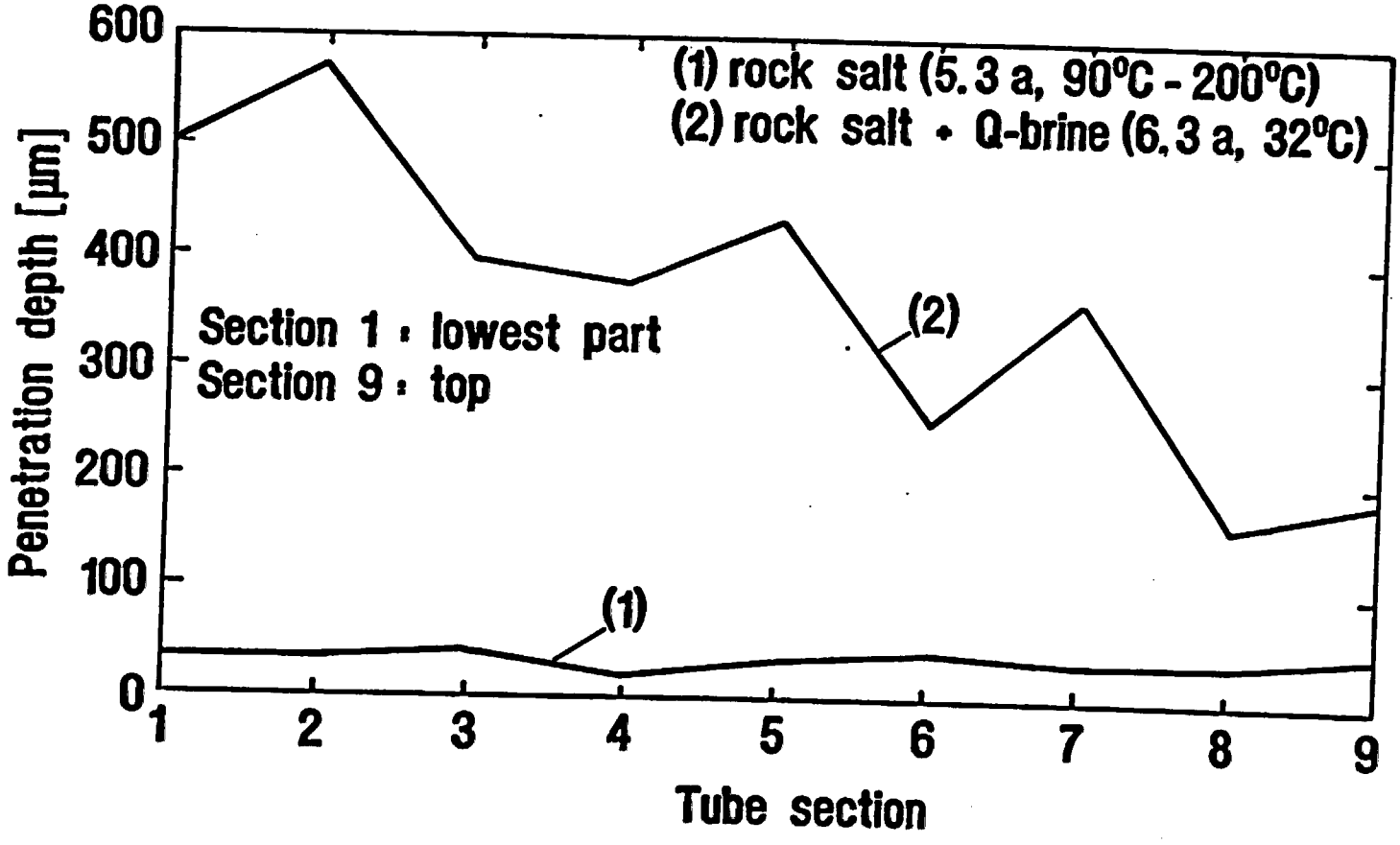

Fig. 24: Surface profilometry results of in-situ tested cast steel tubes. Maximum depth of non-uniform corrosion in rock salt and rock salt+brine

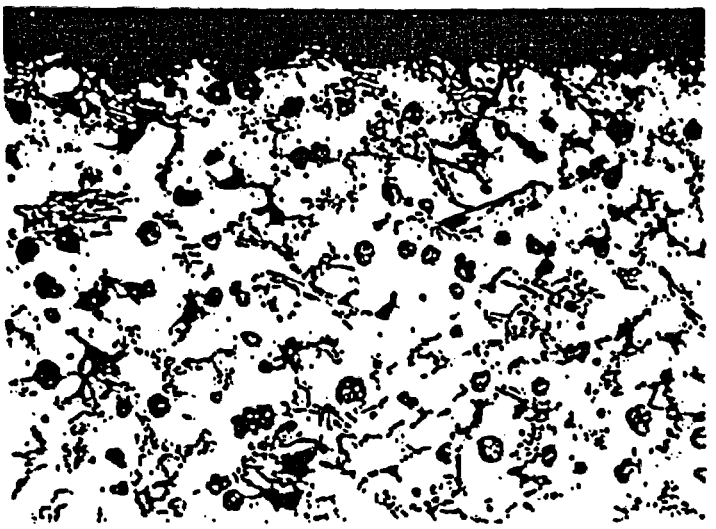

Fig 25: Optical micrograph of a Ni-resist D4 tube after 6.3 years in-situ testing in rock salt (0.1 wt.% H_2O) at 200°C

Fig 26: Optical micrograph of a Ti 99.8-Pd tube after 2.8 years in-situ testing in rock salt plus NaCl-brine at 200°C

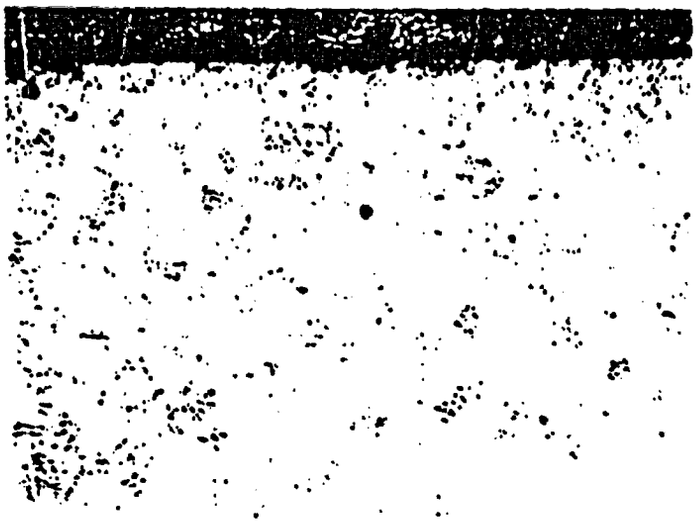

Fig 27: Optical micrograph of the steel tube plating material Ti 99.8-Pd after 5.3 years in-situ testing in rock salt at 200°C (x 200)

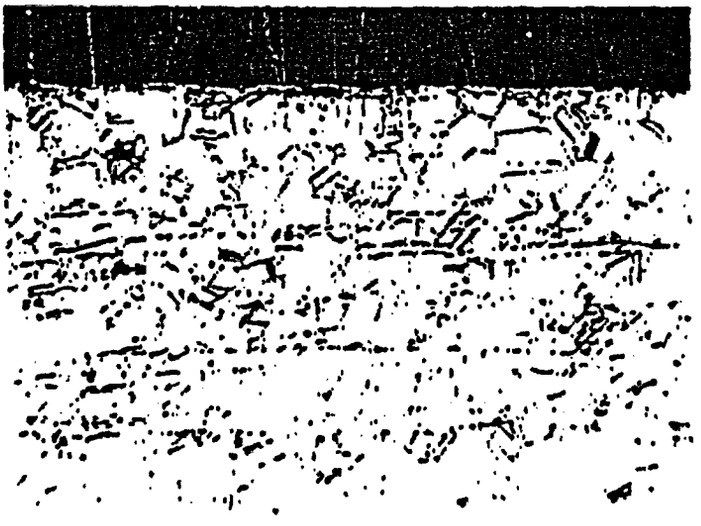

Fig 28: Optical micrograph of the steel tube plating material Hastelloy C4 after 6.3 years in-situ testing in rock salt plus NaCl-brine at 32°C (x 200)

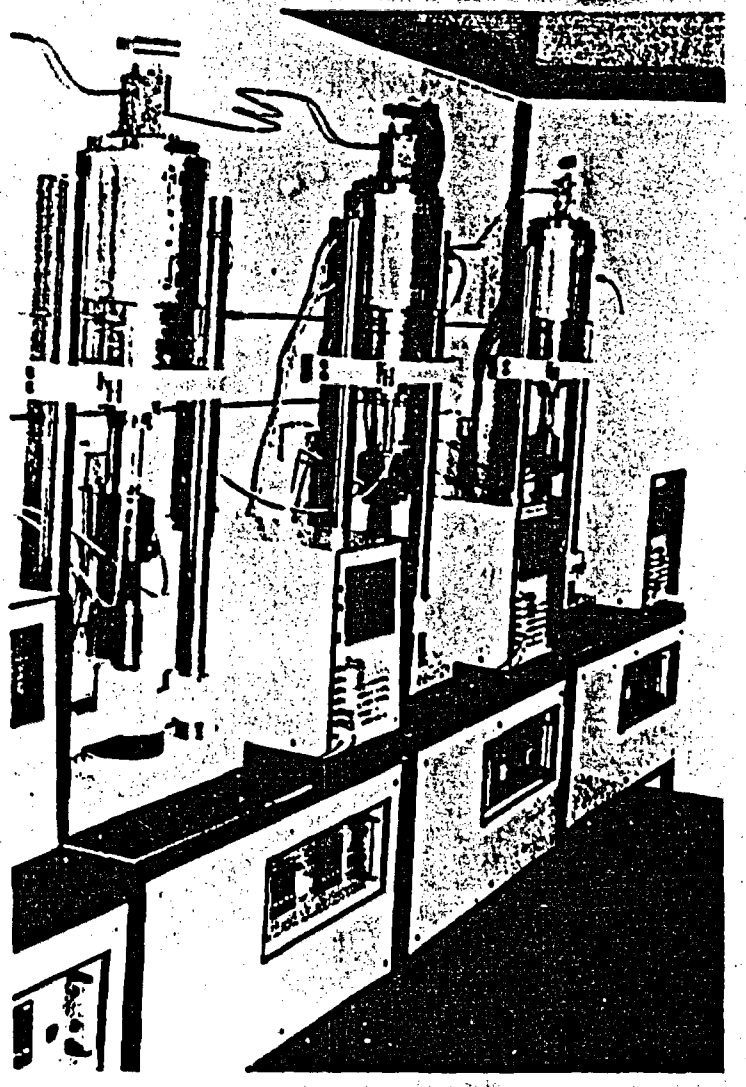

Fig. 29: Slow strain rate testing machine with autoclave

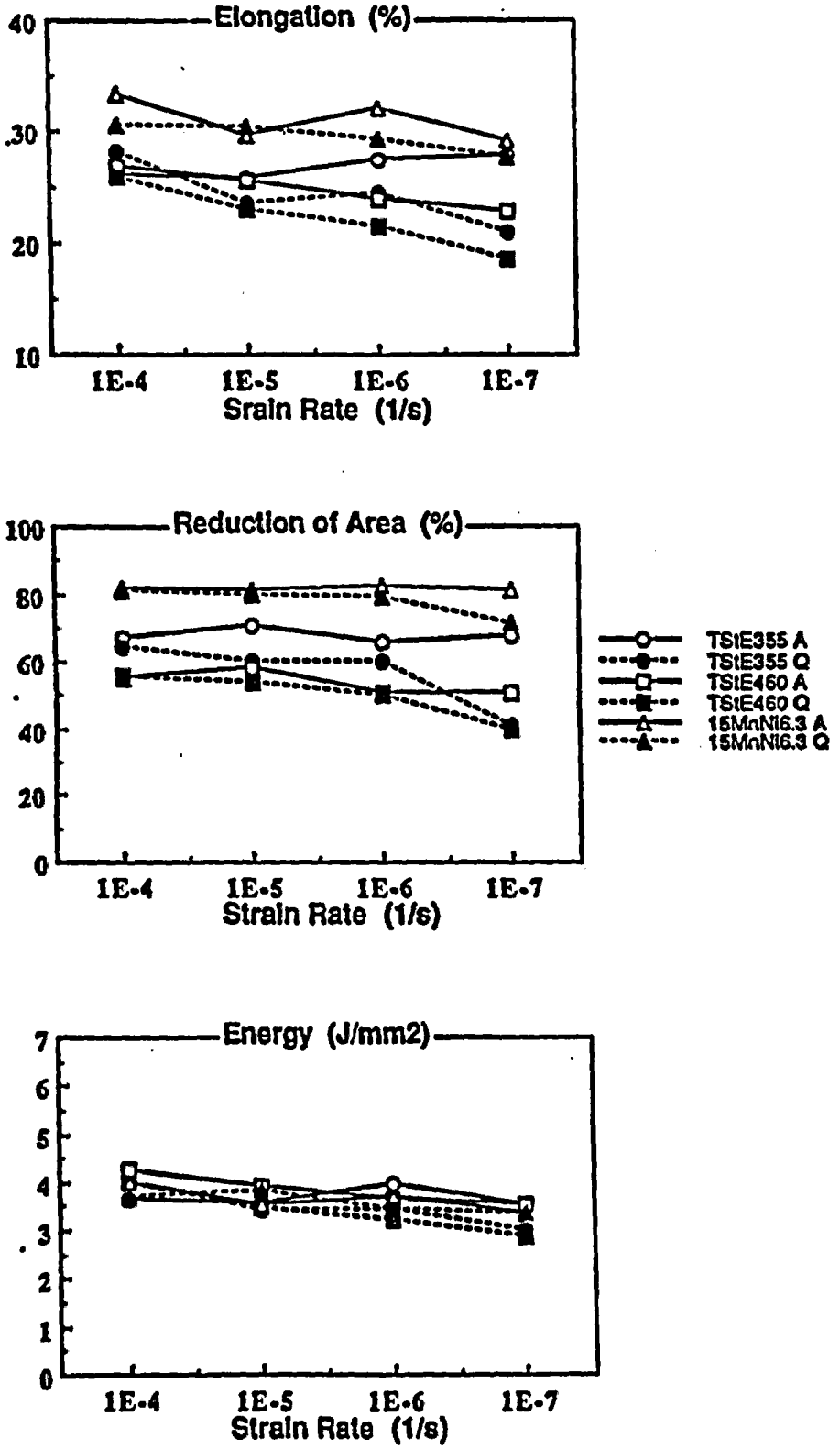

Fig. 30: Elongation, reduction of area and energy versus strain rate for the steels TStE 355, TStE 460 and 15MnNi 6.3 tested at 25°C and 13 MPa in argon and Q-brine

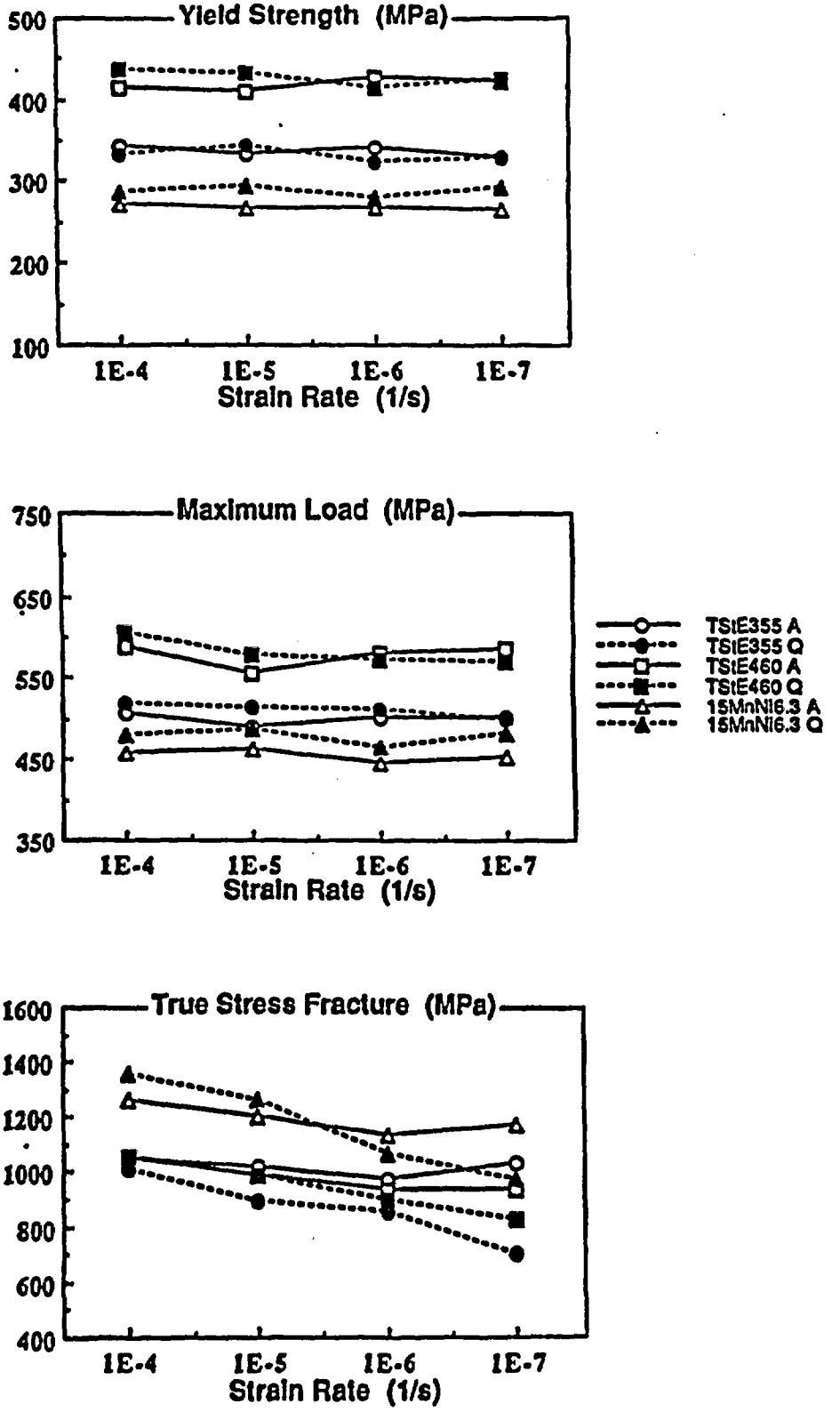

Fig. 31: Yield strength, maximum load and true stress fracture versus strain rate for the steels TStE 355, TStE 460 and 15MnNi 6.3 tested at 25°C and 13 MPa in argon and Q-brine

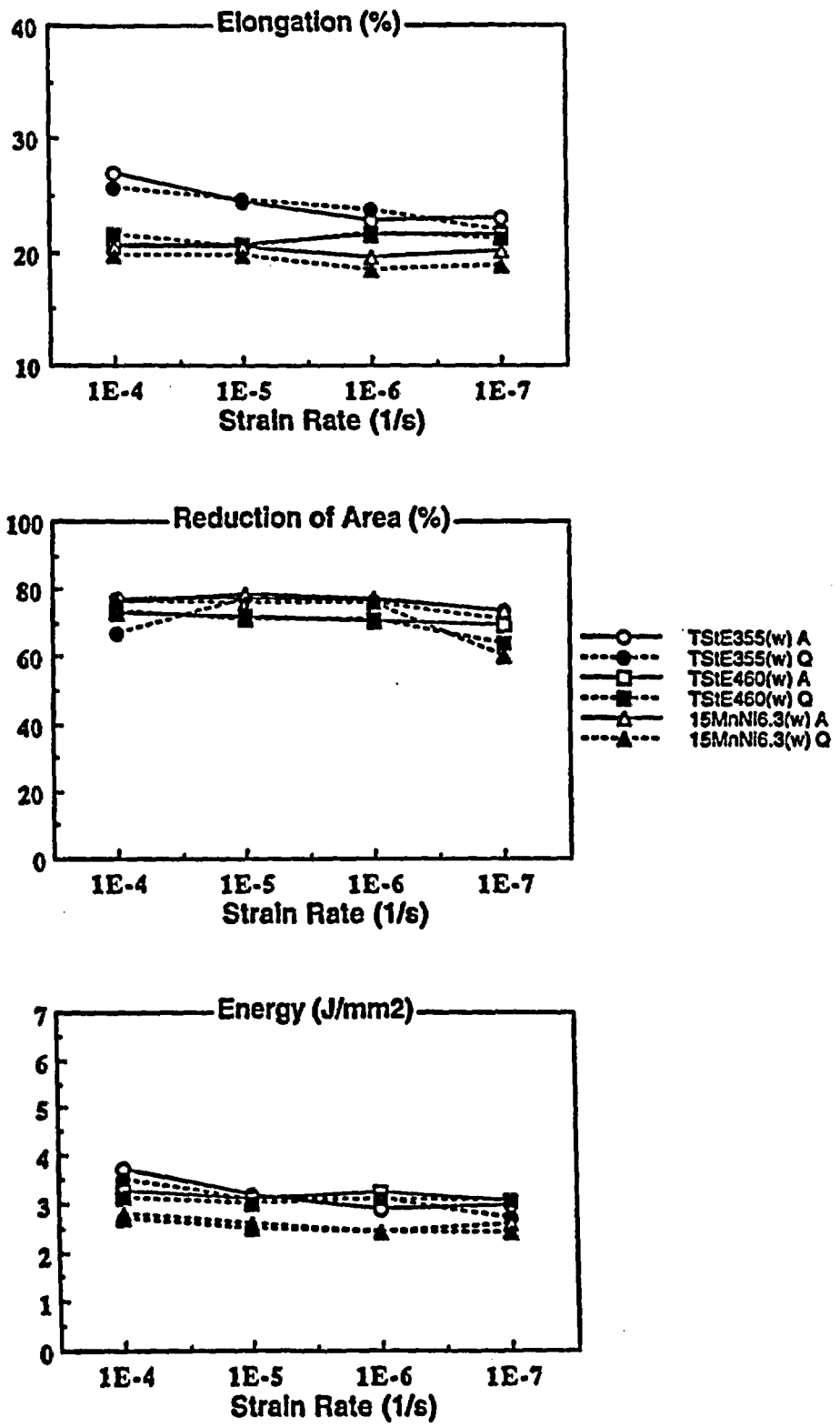

Fig. 32: Elongation, reduction of area and energy versus strain rate for the MAG welded steels TStE 355, TStE 460 and 15MnNi 6.3 tested at 25°C in argon and Q-brine

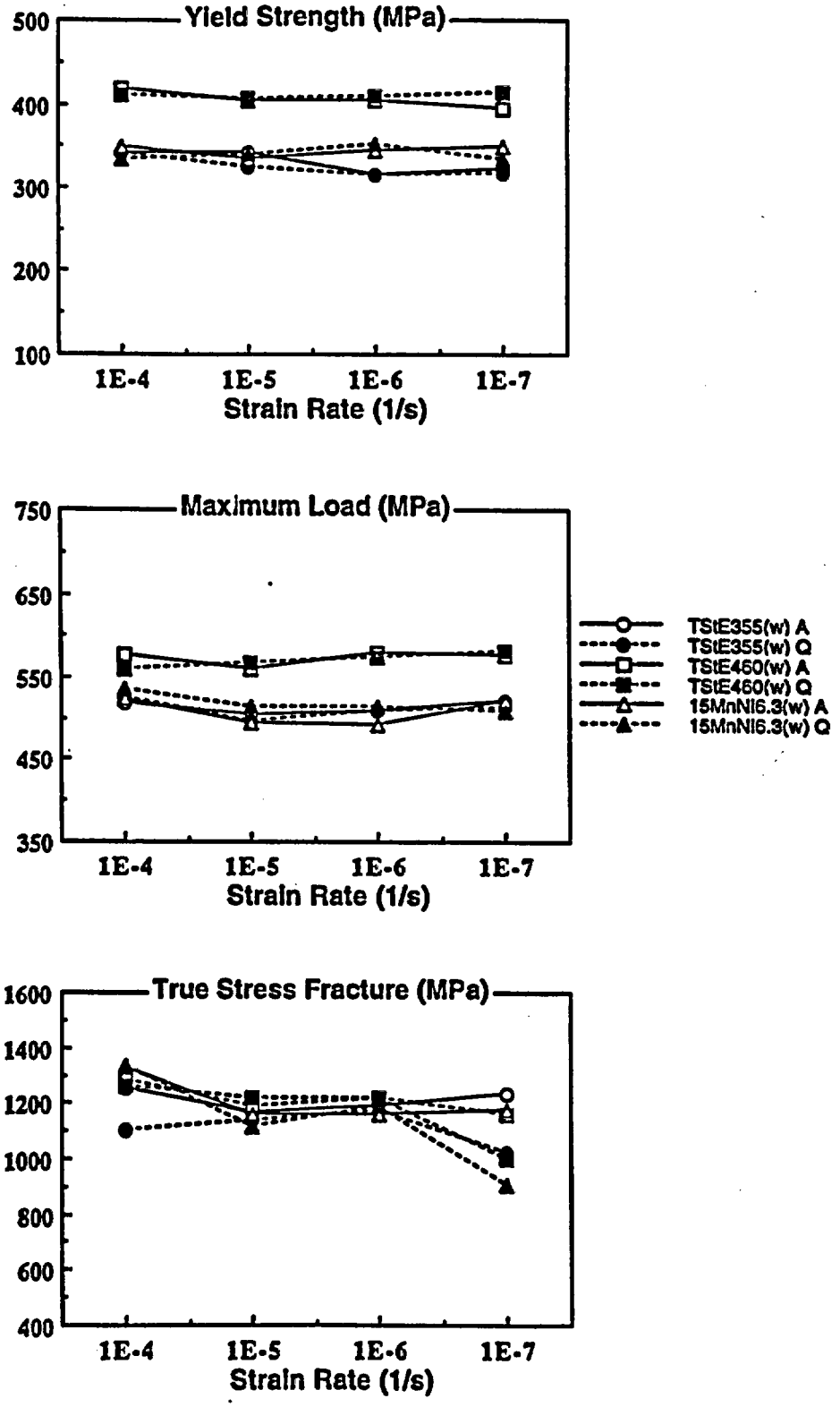

Fig. 33: Yield strength, maximum load and true stress fracture versus strain rate for the MAG welded steels TStE 355, TStE 460 and 15MnNi 6.3 tested at 25°C in argon and Q-brine

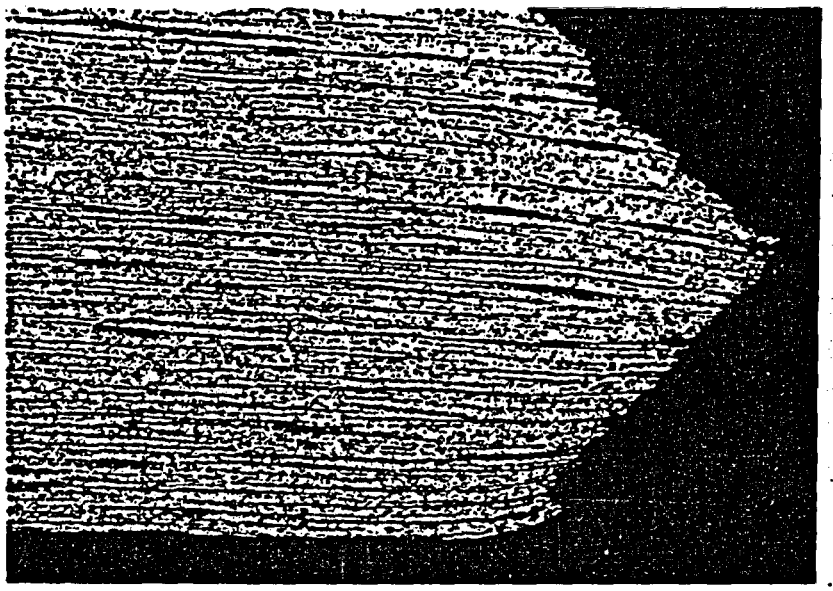

Fig. 34: TStE 460 steel X 50

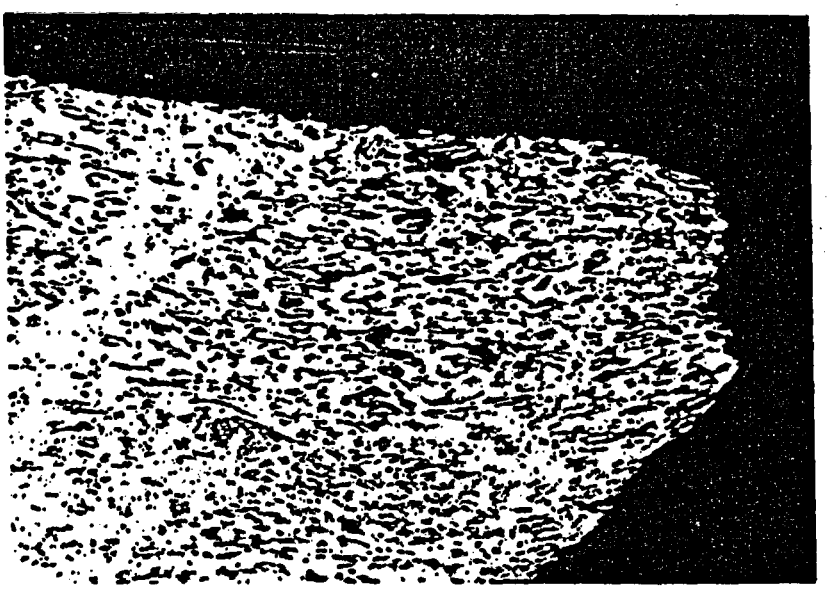

Fig. 35: 15MnNi 6.3 steel (MAG welded) X 100

Fig 34-35: Optical micrographs of steel specimens tested in Q-brine at 25°C and $10^{-7}s^{-1}$

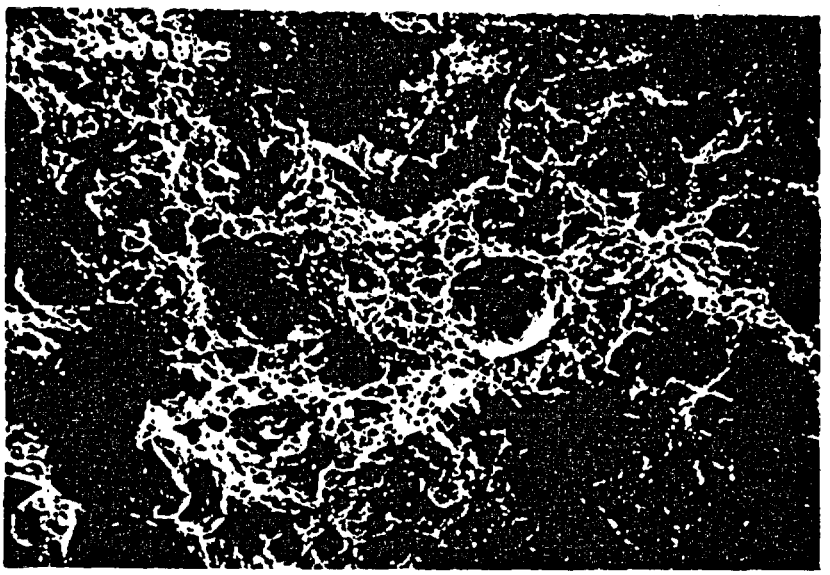

Fig. 36: SEM micrograph of the fracture surface of a MAG welded 15MnNi 6.3 steel specimen tested in Q-brine at 25°C and $10^{-6}s^{-1}$ (x 500)

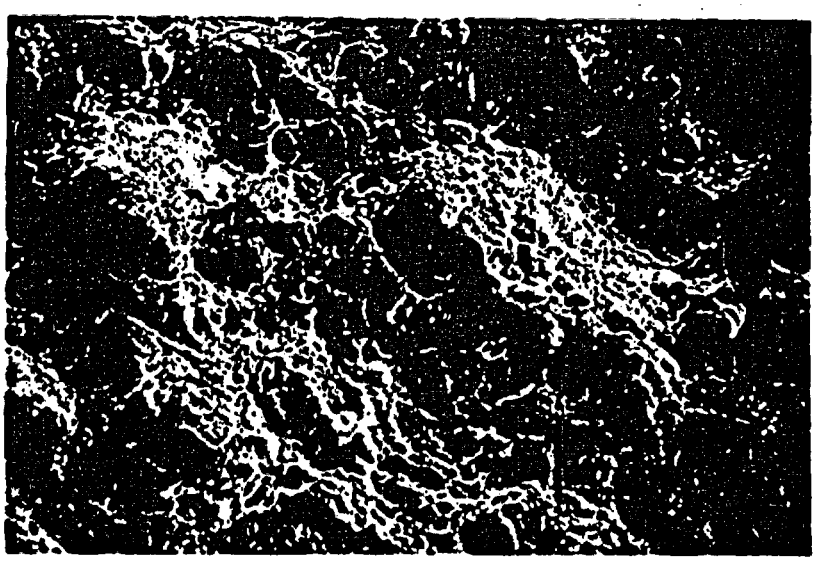

Fig. 37: SEM micrograph of the fracture surface of a TStE 355 steel specimen tested in Q-brine at 25°C and $10^{-7}s^{-1}$ (x 1000)

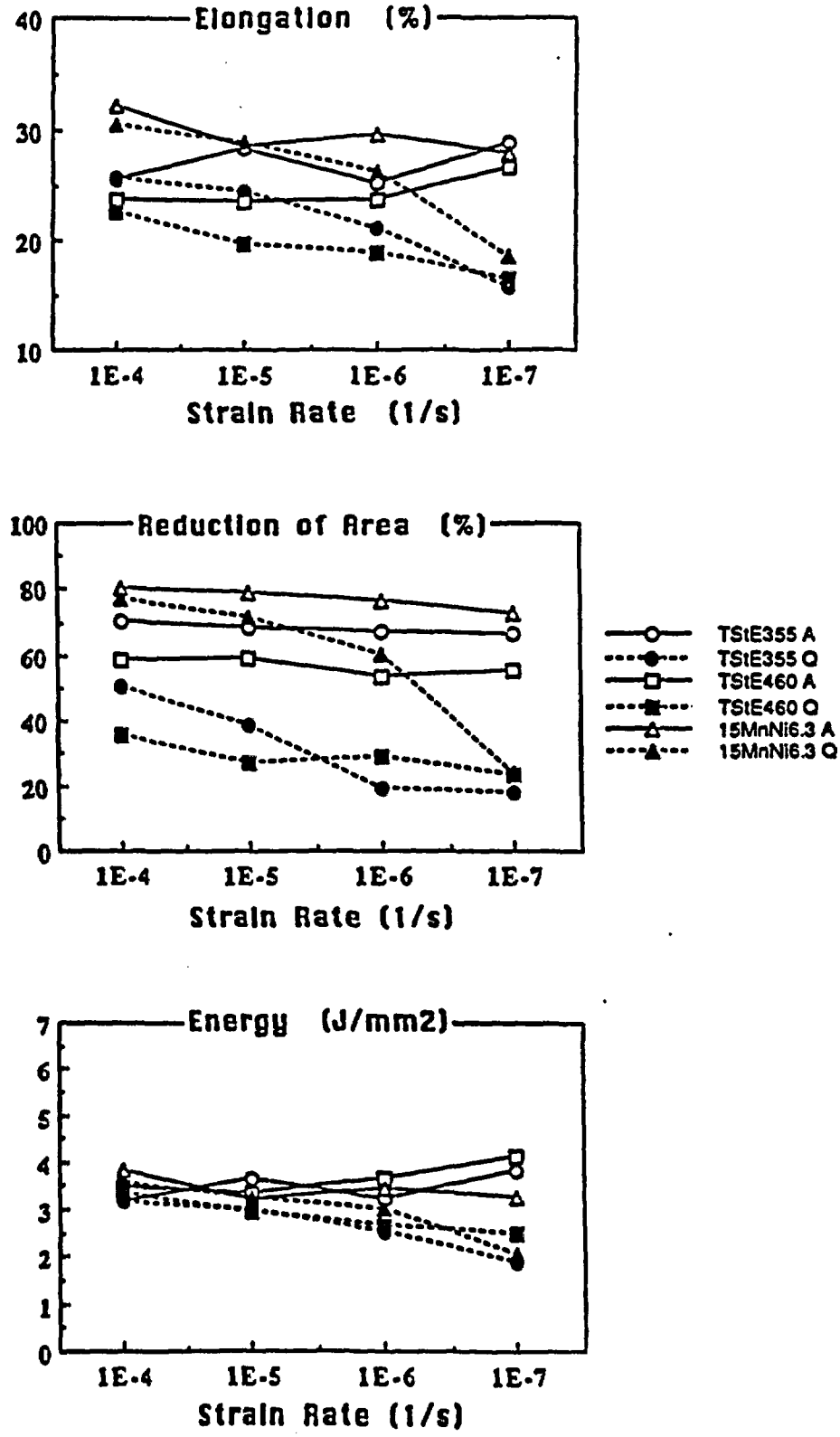

Fig. 38: Elongation, reduction of area and energy versus strain rate for the steels TStE 355, TStE 460 and 15MnNi 6.3 tested at 90°C and 13 MPa in argon and Q-brine

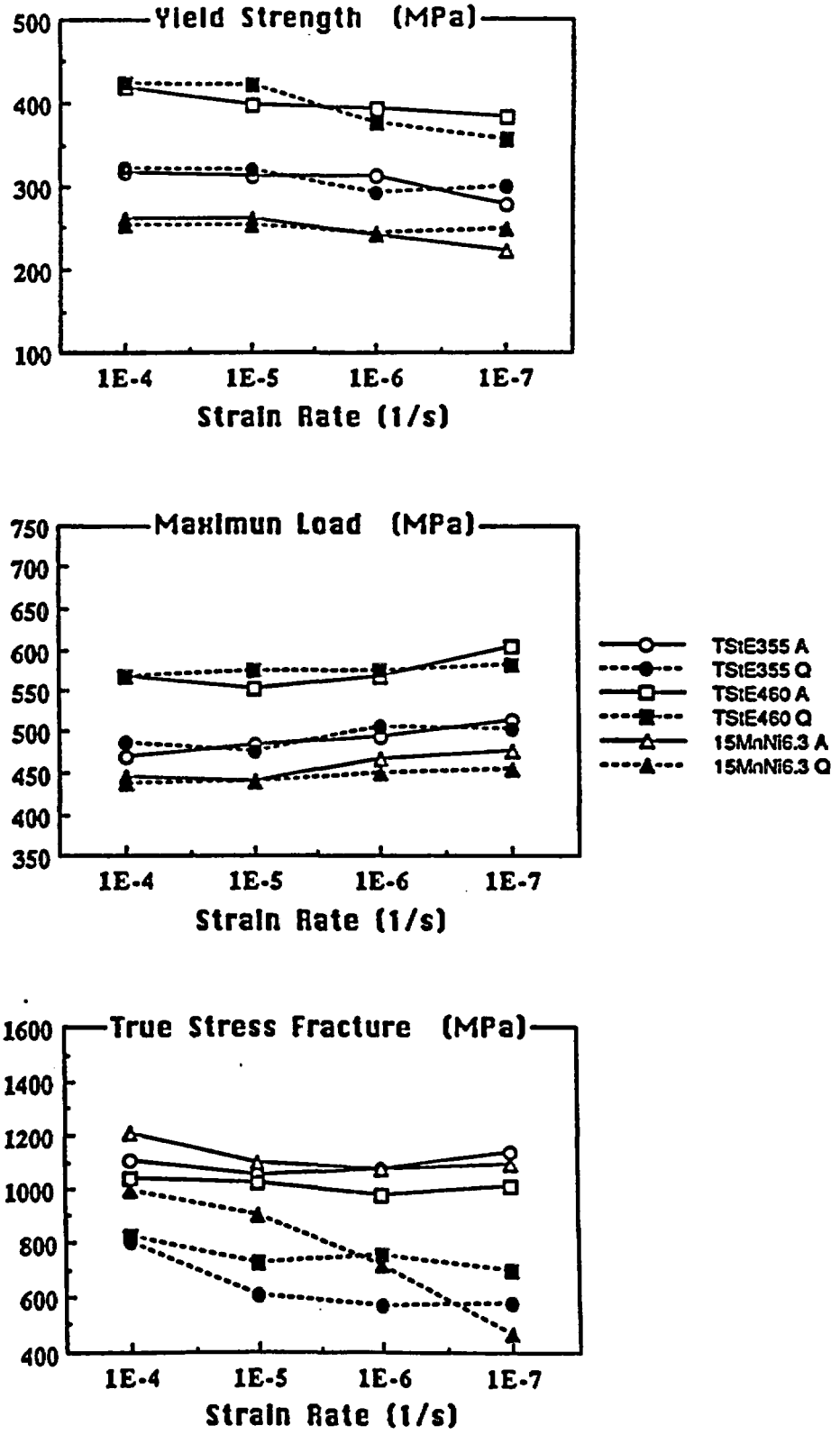

Fig. 39: Yield strength, maximum load and true stress fracture versus strain rate for the steels TStE 355, TStE 460 and 15MnNi 6.3 tested at 90°C and 13 MPa in argon and Q-brine

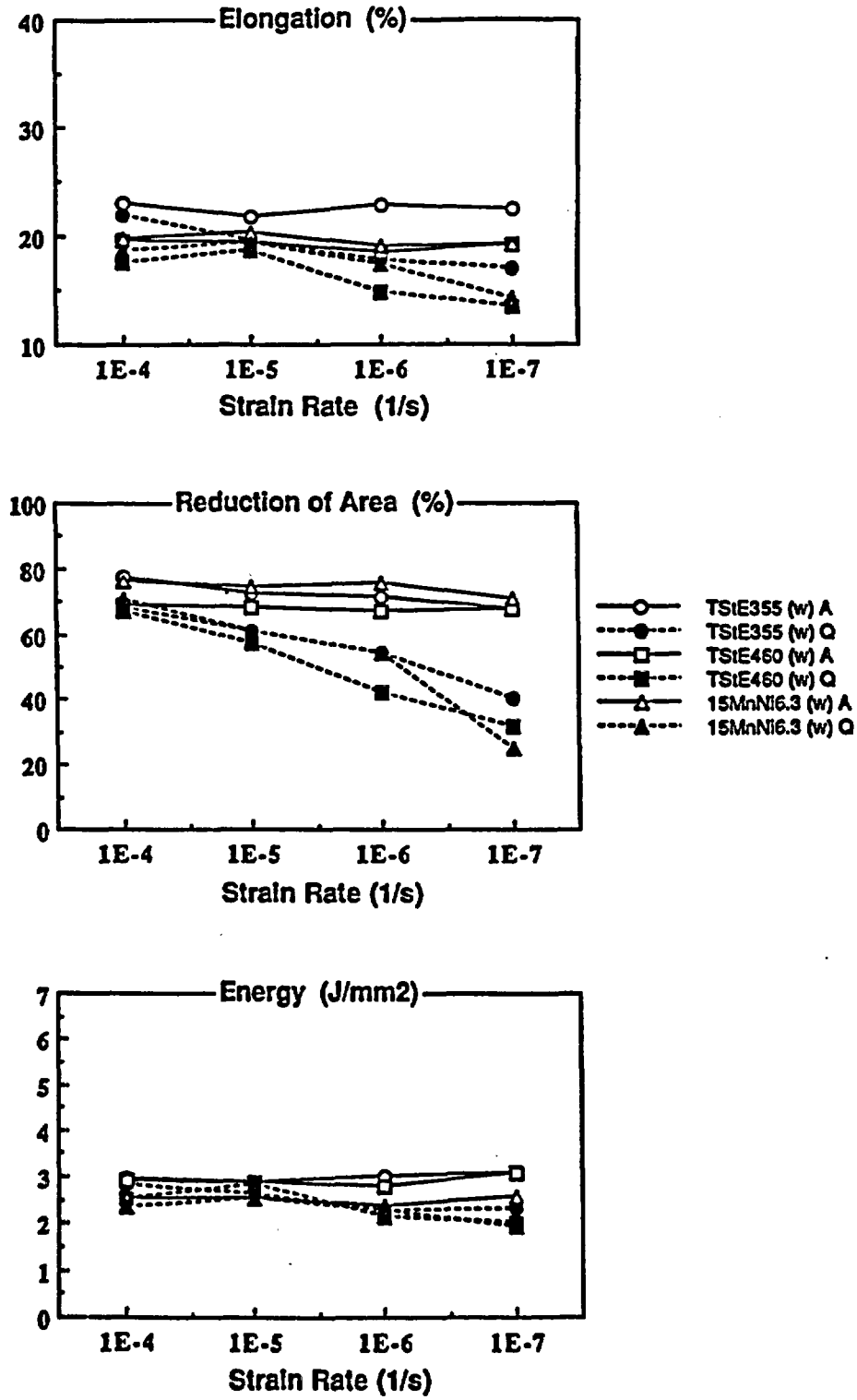

Fig. 40: Elongation, reduction of area and energy versus strain rate for the steels TStE 355, TStE 460 and 15MnNi 6.3 tested at 90°C in argon and Q-brine

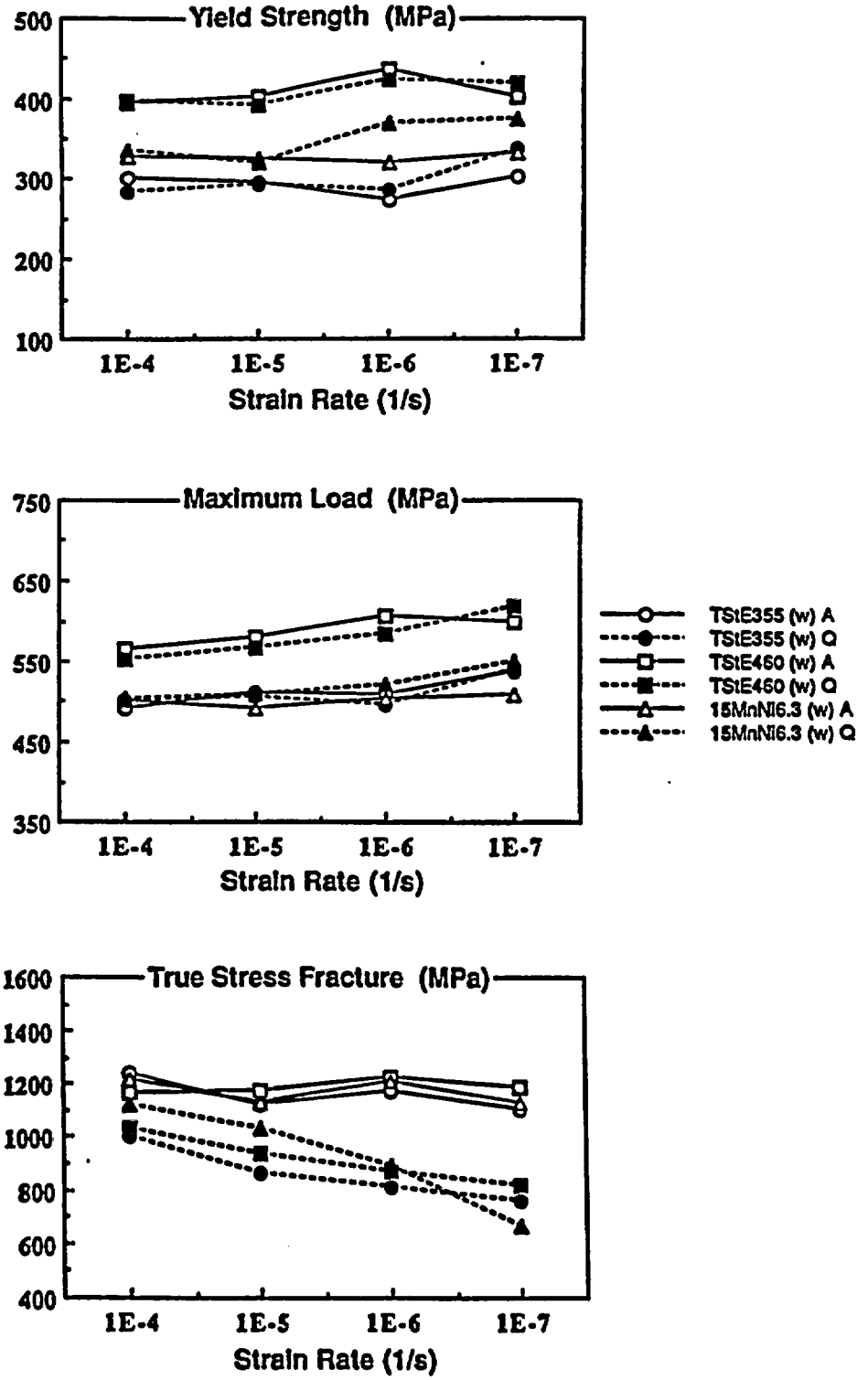

Fig. 41: Yield strength, maximum load and true stress fracture versus strain rate for the MAG welded steels TStE 355, TStE 460 and 15MnNi 6.3 tested at 90°C in argon and Q-brine

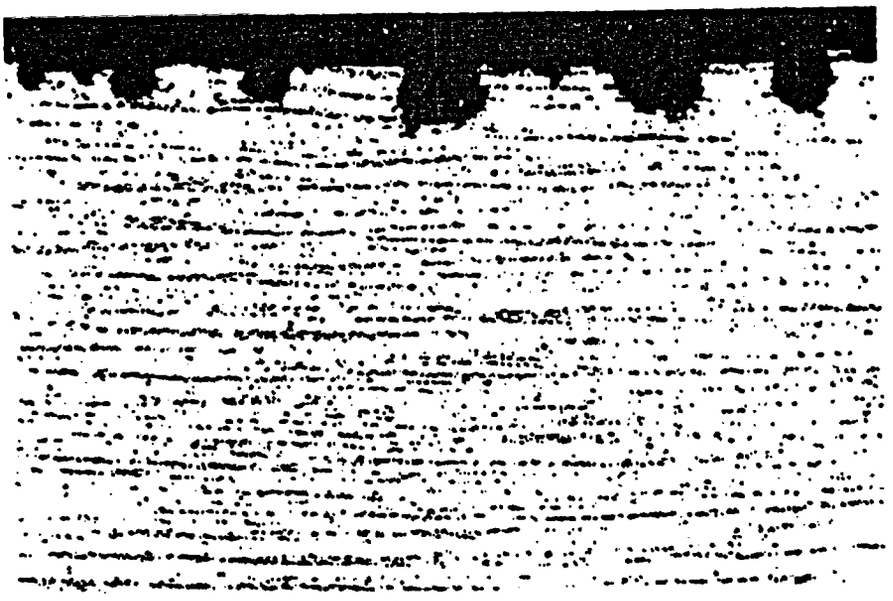

Fig. 42: Optical micrograph of a MAG welded TStE 460 steel specimen tested in Q-brine at 90°C and $10^{-6}s^{-1}$ (X 100)

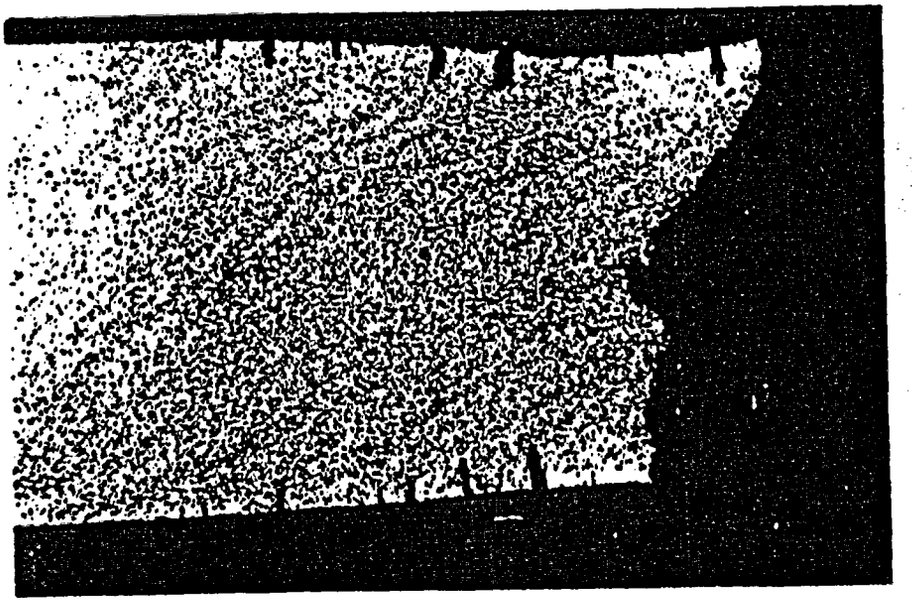

Fig. 43: Optical micrograph of a 15MnNi 6.3 steel specimen tested in Q-brine at 25°C and $10^{-7}s^{-1}$ (X 12.8)

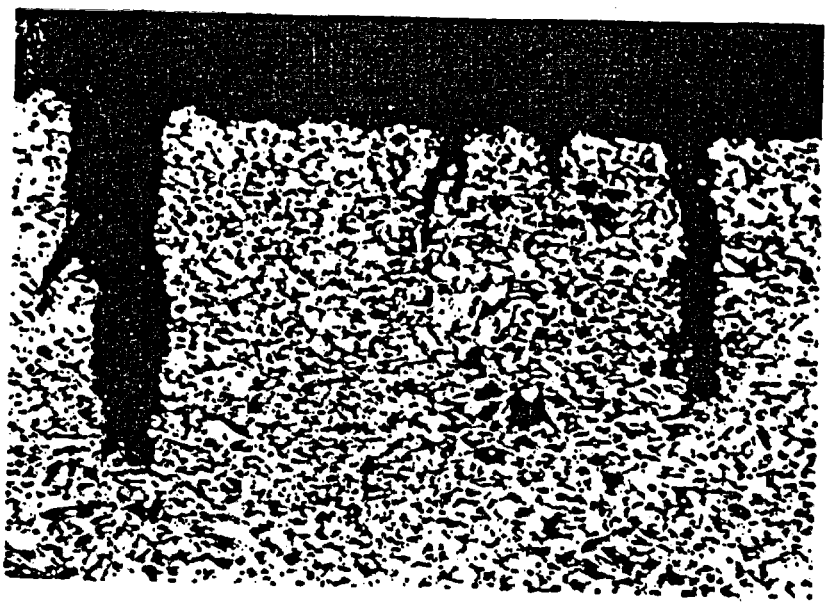

Fig. 44: Optical micrograph of a 15MnNi 6.3 steel specimen tested in Q-brine at 90°C and $10^{-7}s^{-1}$ (x 100)

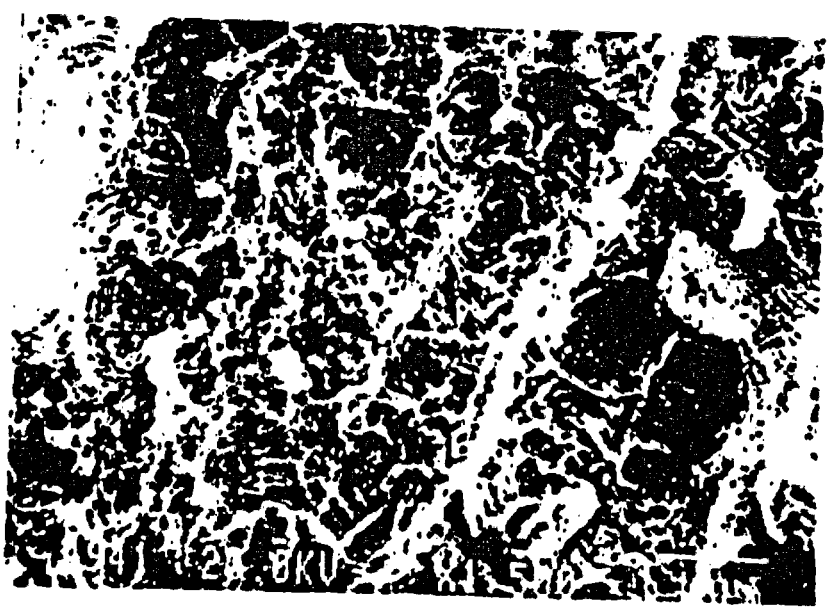

Fig. 45: SEM micrograph of the fracture surface of a TStE 460 steel specimen tested in Q-brine at 90°C and $10^{-7}s^{-1}$ (x 1500)

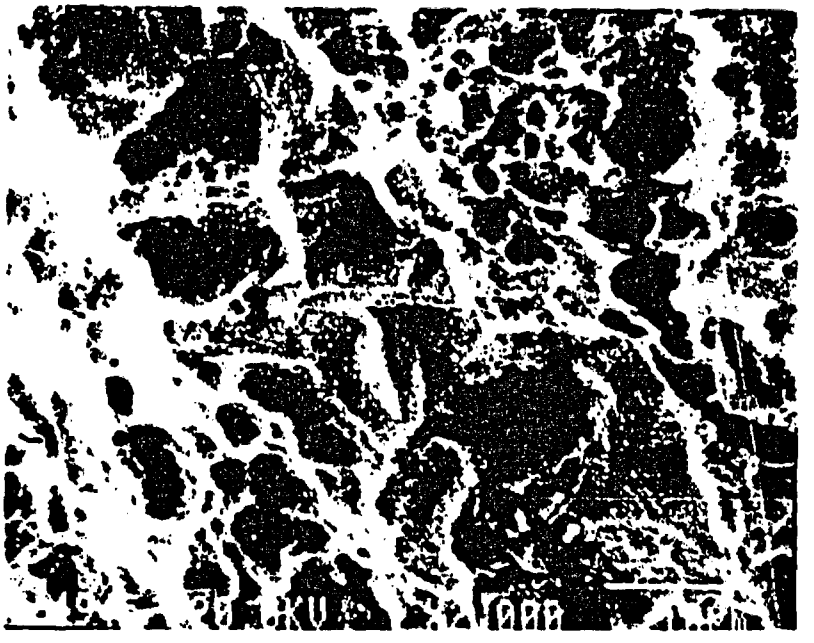

Fig. 46: SEM micrograph of the fracture surface of a 15MnNi 6.3 steel specimen tested in Q-brine at 90°C and $10^{-7}s^{-1}$ (X 2000)

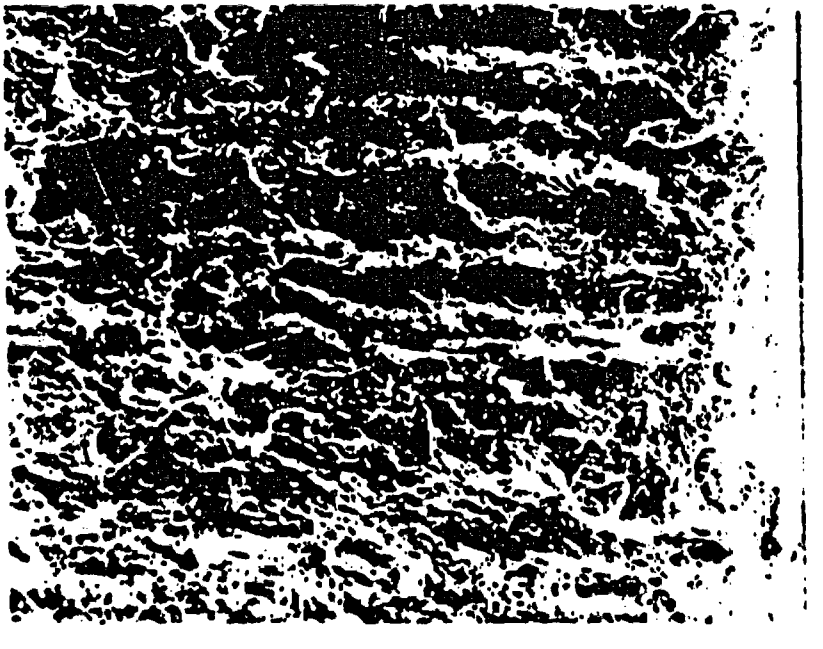

Fig. 47: SEM micrograph of the fracture surface of a MAG welded TStE 355 steel specimen tested in Q-brine at 90°C and $10^{-7}s^{-1}$ (X 500)

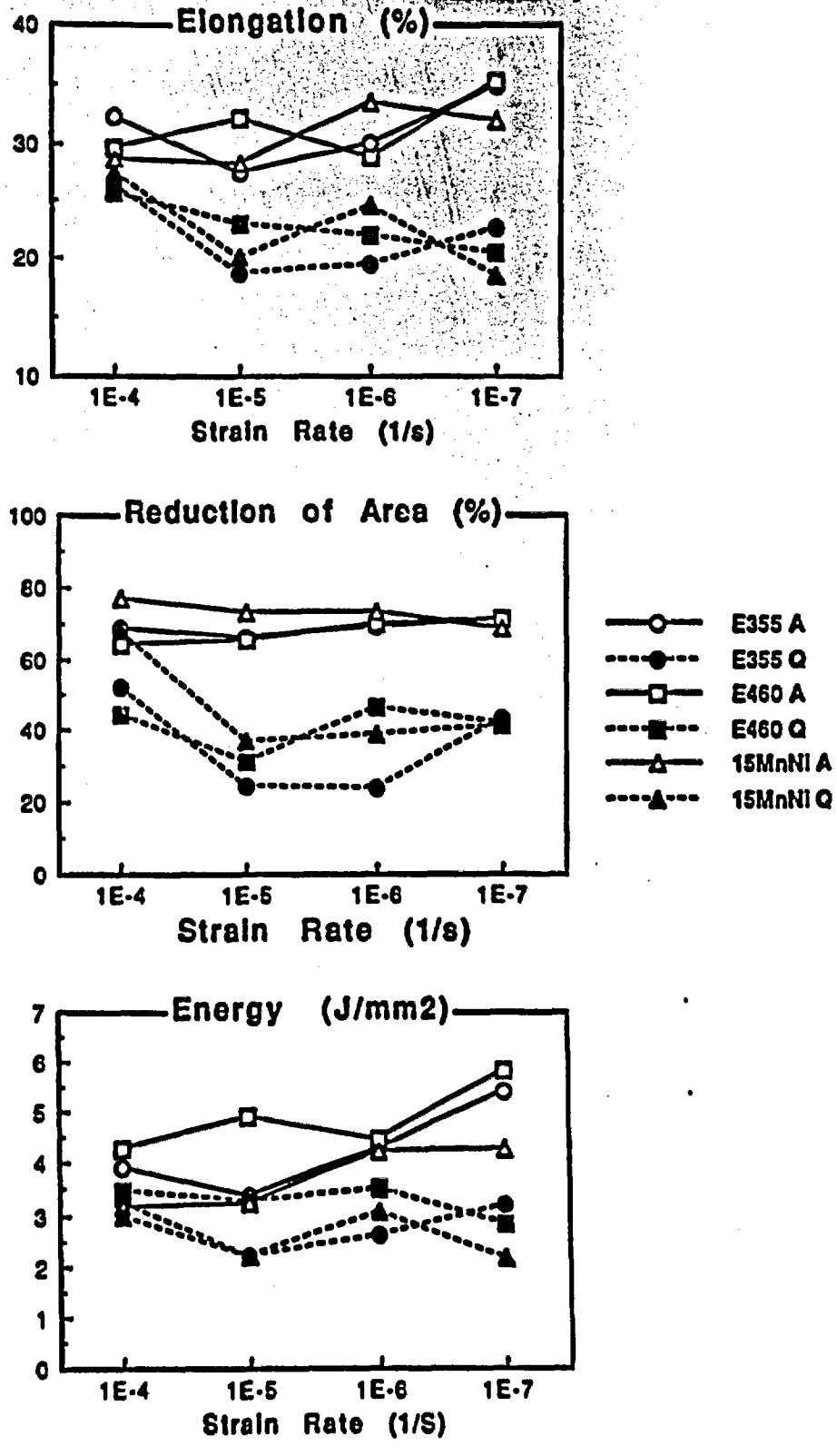

Fig. 48: Elongation, reduction of area and energy versus strain rate for the steels TStE 355, TStE 460 and 15MnNI 6.3 tested at 170°C and 13 MPa in argon and Q-brine

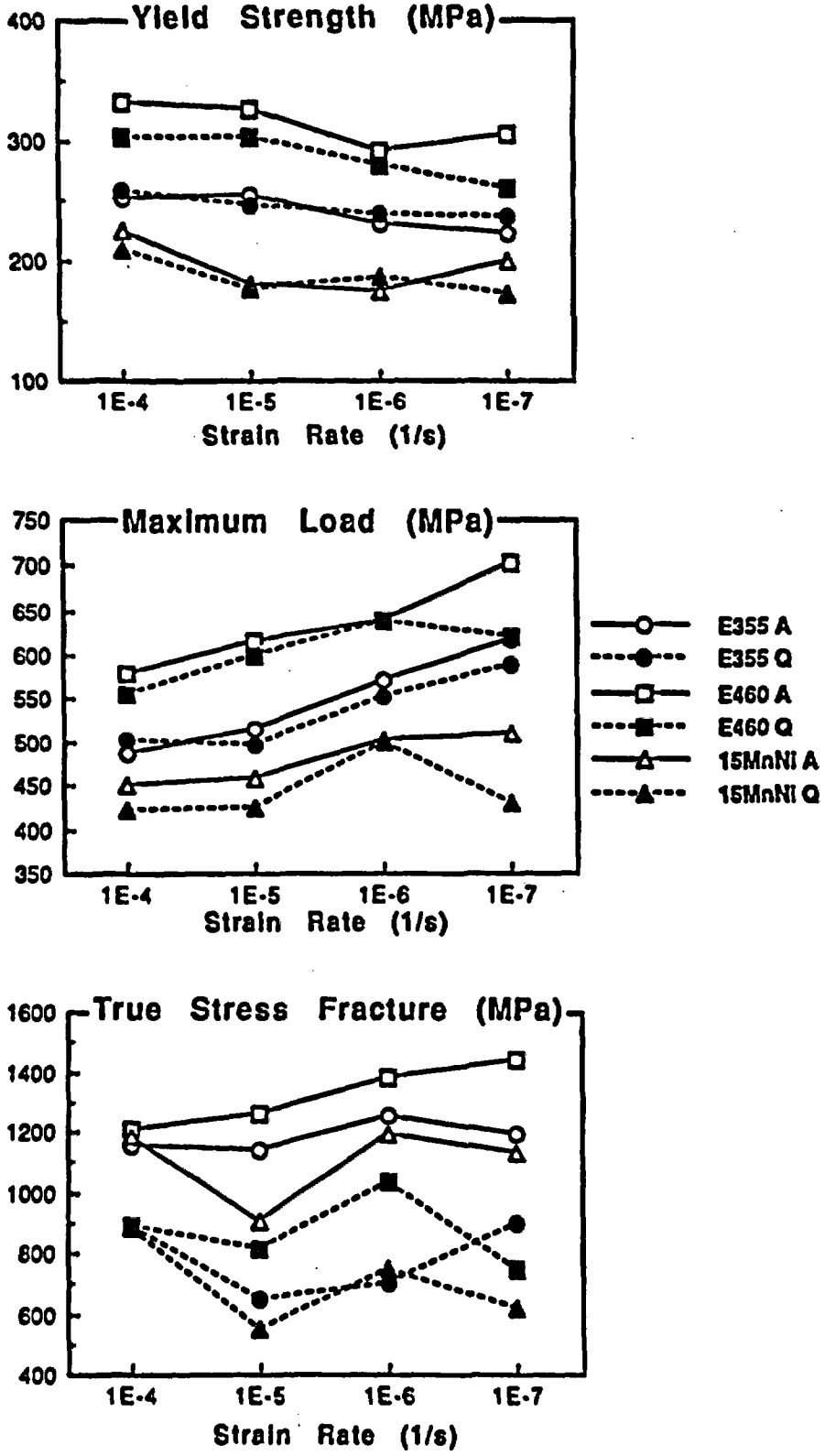

Fig. 49: Yield strength, maximum load and true stress fracture versus strain rate for the steels TStE 355, TStE 460 and 15MnNi 6.3 tested at 170°C and 13 MPa in argon and Q-brine

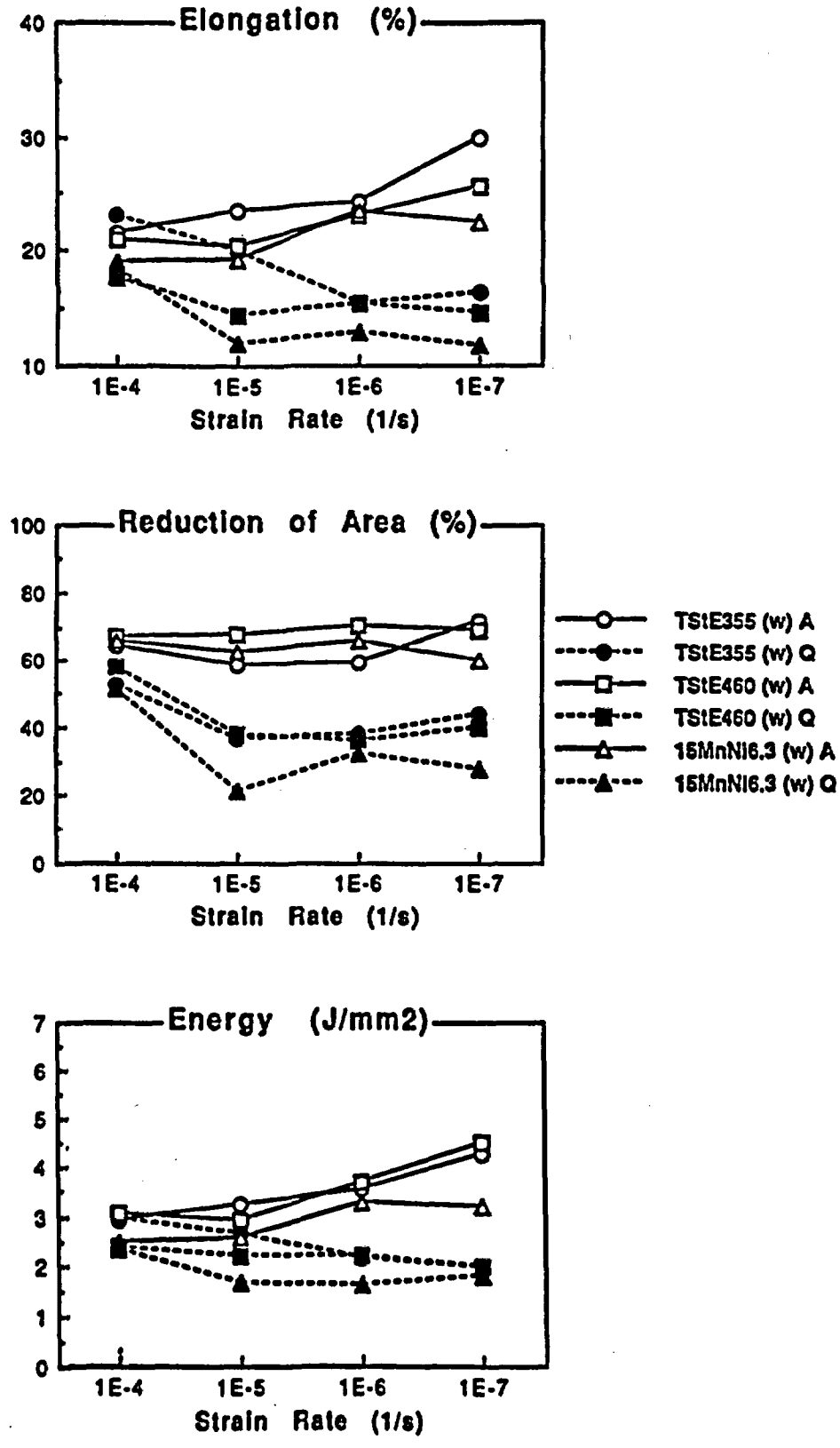

Fig. 50: Elongation, reduction of area and energy versus strain rate for the MAG welded steels TStE 355, TStE 460 and 15MnNi 6.3 tested at 170°C and 13 MPa in argon and Q-brine

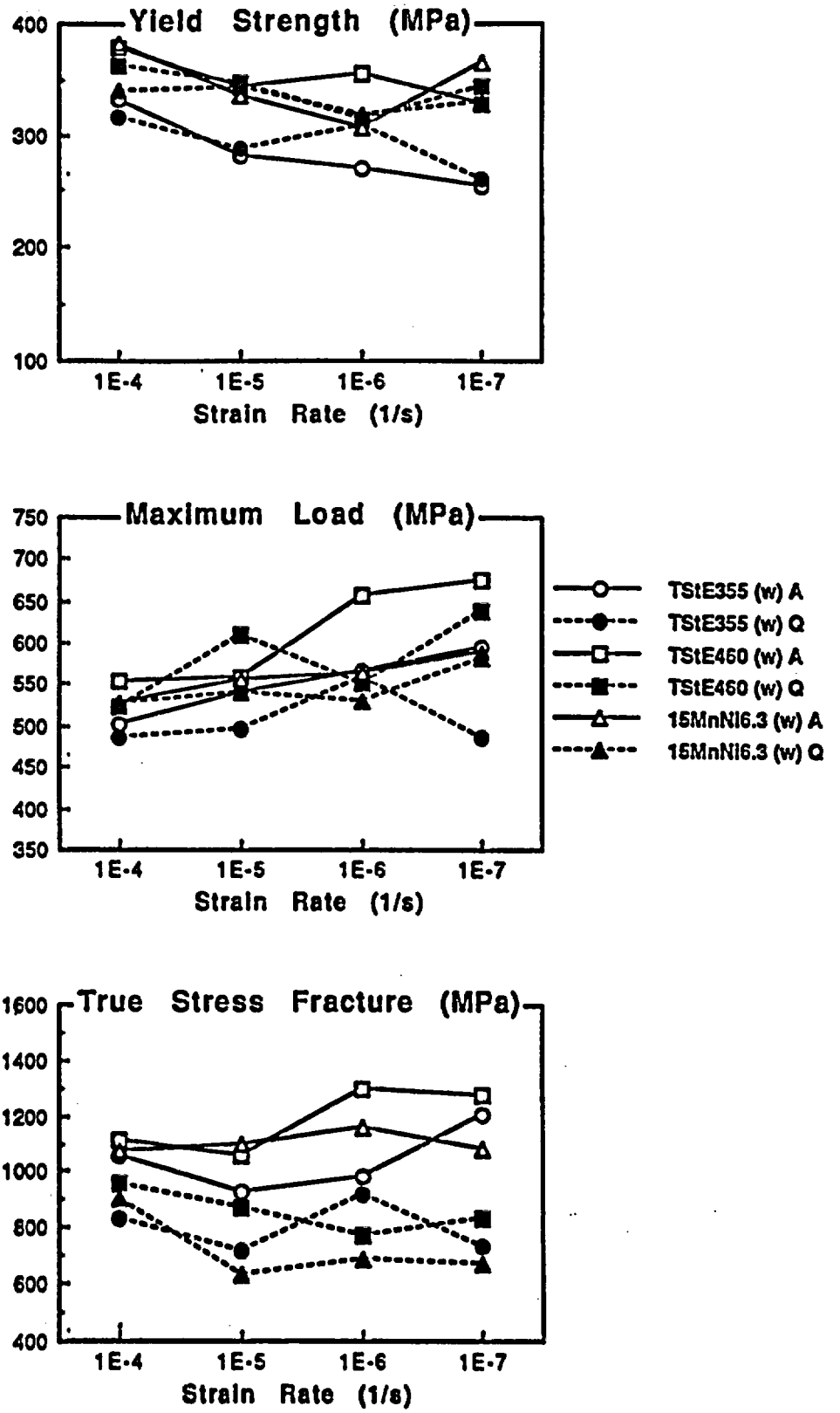

Fig. 51: Yield strength, maximum load and true stress fracture versus strain rate for the MAG welded steels TStE 355, TStE 460 and 15MnNi 6.3 tested at 170°C and 13 MPa in argon and Q-brine

Fig. 52: Extensive secondary cracking of the 15MnNi 6.3 steel tested in Q-brine at 170°C, 13 MPa and $10^{-5}s^{-1}$

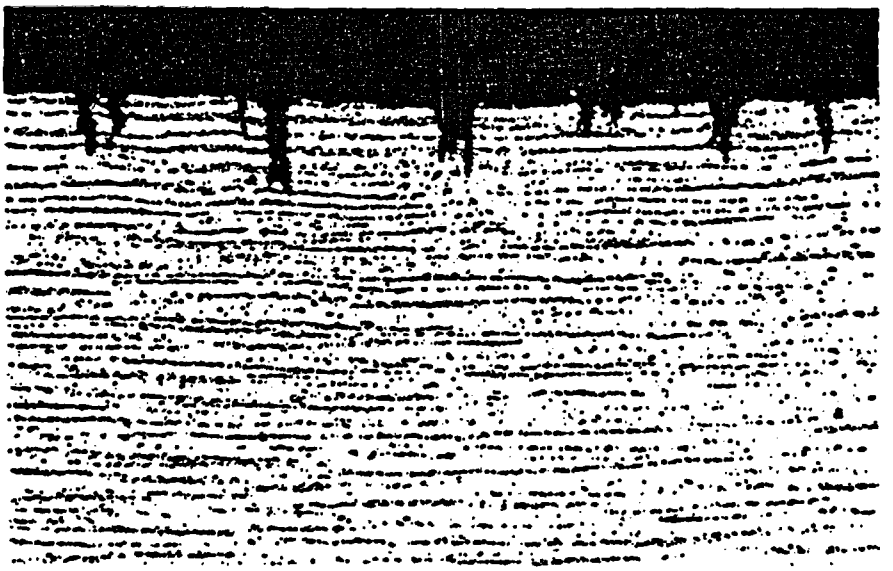

Fig. 53: Optical micrograph of a TStE 460 steel specimen tested in Q-brine at 170°C and $10^{-5}s^{-1}$ (x 100)

Fig. 54: Optical micrograph of a 15MnNi 6.3 steel specimen tested in Q-brine at 170°C and $10^{-5}s^{-1}$ (x 200)

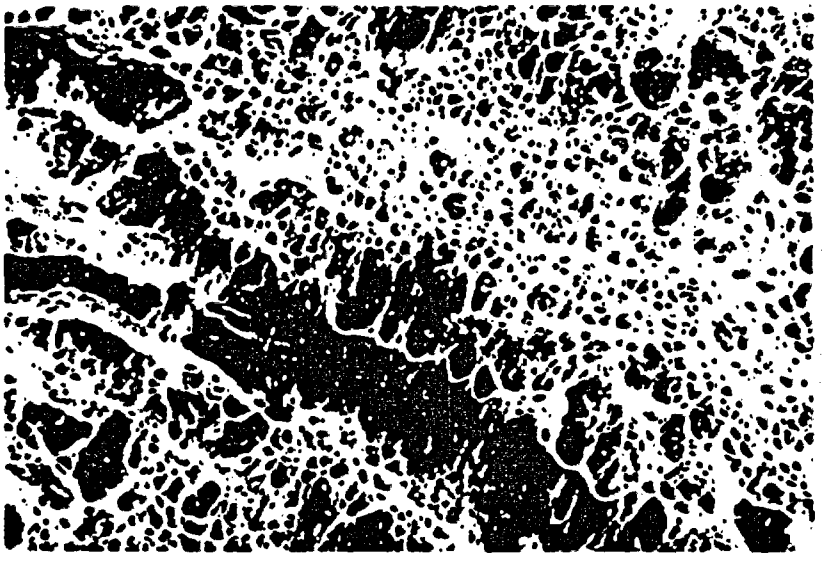

Fig. 55: Argon

Fig. 56: Q-brine

Figs. 55-56: SEM micrographs of the fracture surface of TStE 460 steel specimens tested in argon and Q-brine at 170°C and $10^{-5}s^{-1}$ (x500)

Fig. 57: SEM micrograph of the fracture surface of a 15MnNi 6.3 steel specimen tested in Q-brine at 170°C and $10^{-6}s^{-1}$ (X 200)

Fig. 58: SEM micrograph of lateral secondary cracks of a 15MnNi 6.3 steel specimen tested in Q-brine at 170°C and $10^{-5}s^{-1}$ (X 200)

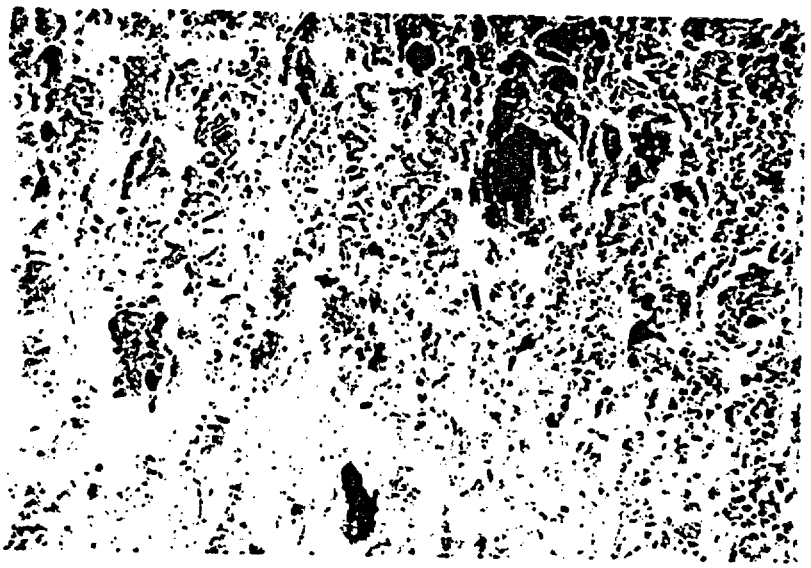

Fig. 59: SEM micrograph of the fracture surface of a MAG welded TStE 355 steel specimen tested in Q-brine at 170°C and $10^{-5}s^{-1}$ (X 250)

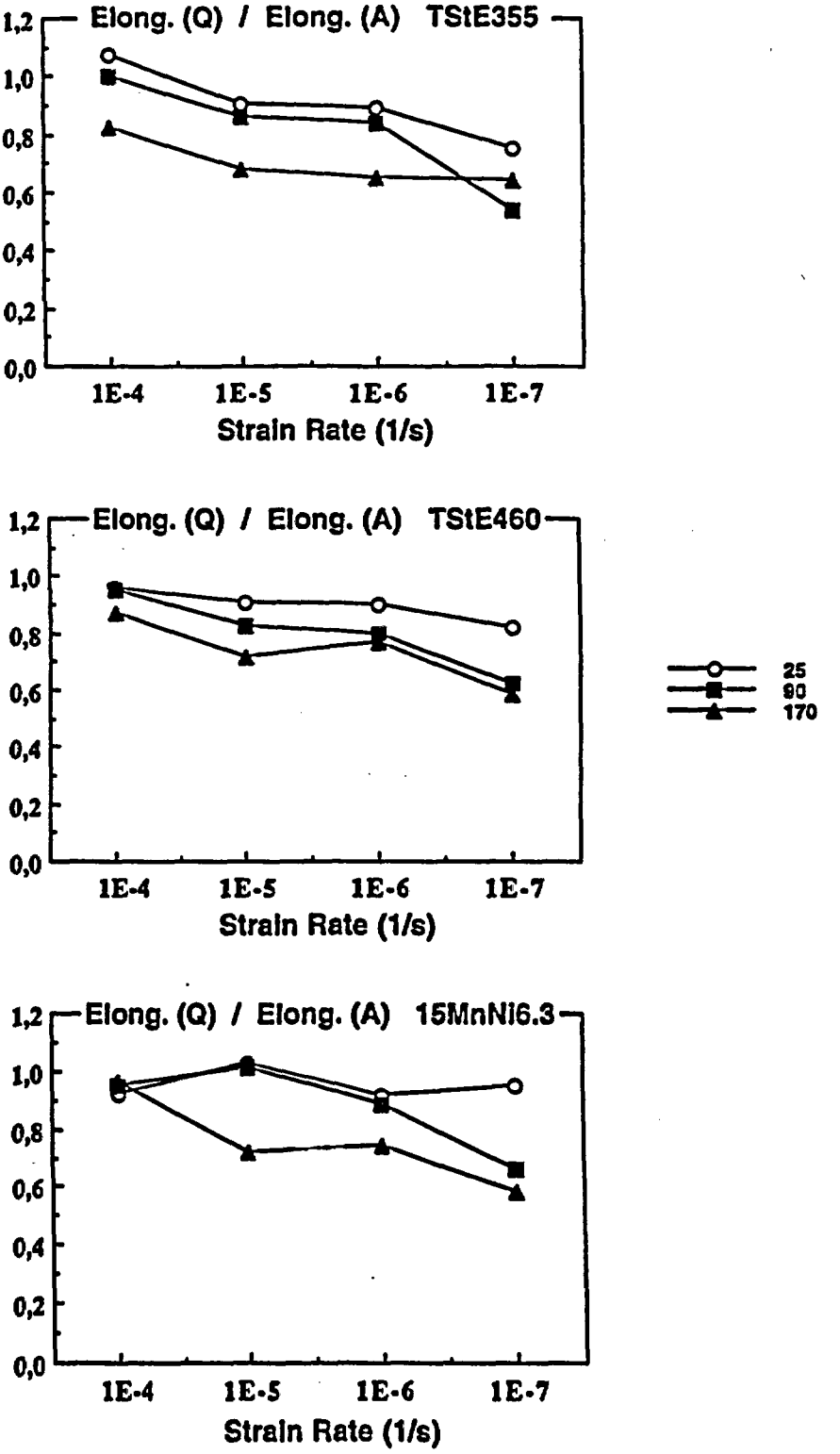

Fig. 60: Ratio of elongations in Q-brine and argon versus strain rate for the TStE 355, TStE 460 and 15MnNi 6.3 steels at various temperatures

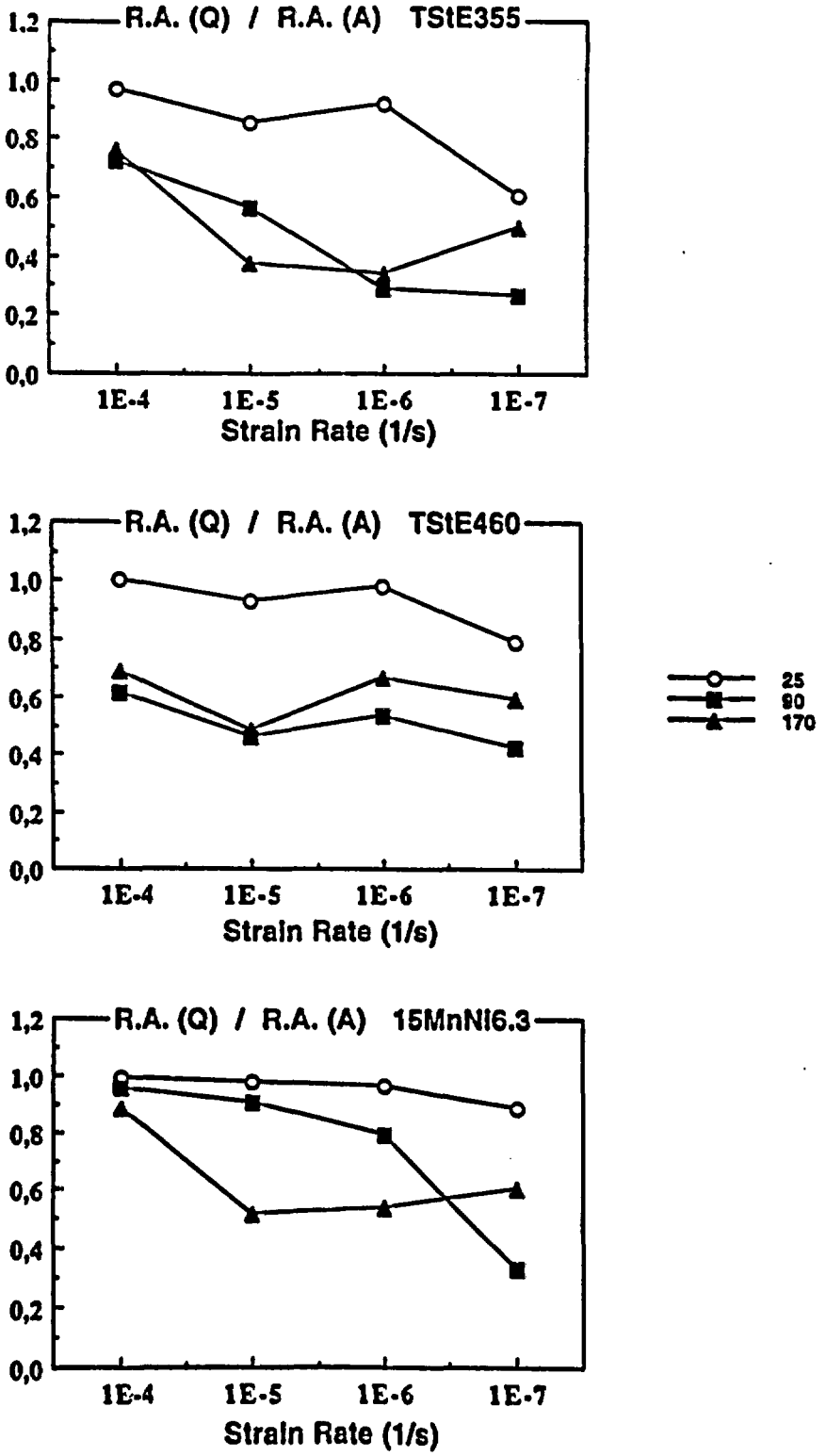

Fig. 61: Ratio of reduction of areas in Q-brine and argon versus strain rate for the TStE 355, TStE 460 and 15MnNi 6.3 steels at various temperatures

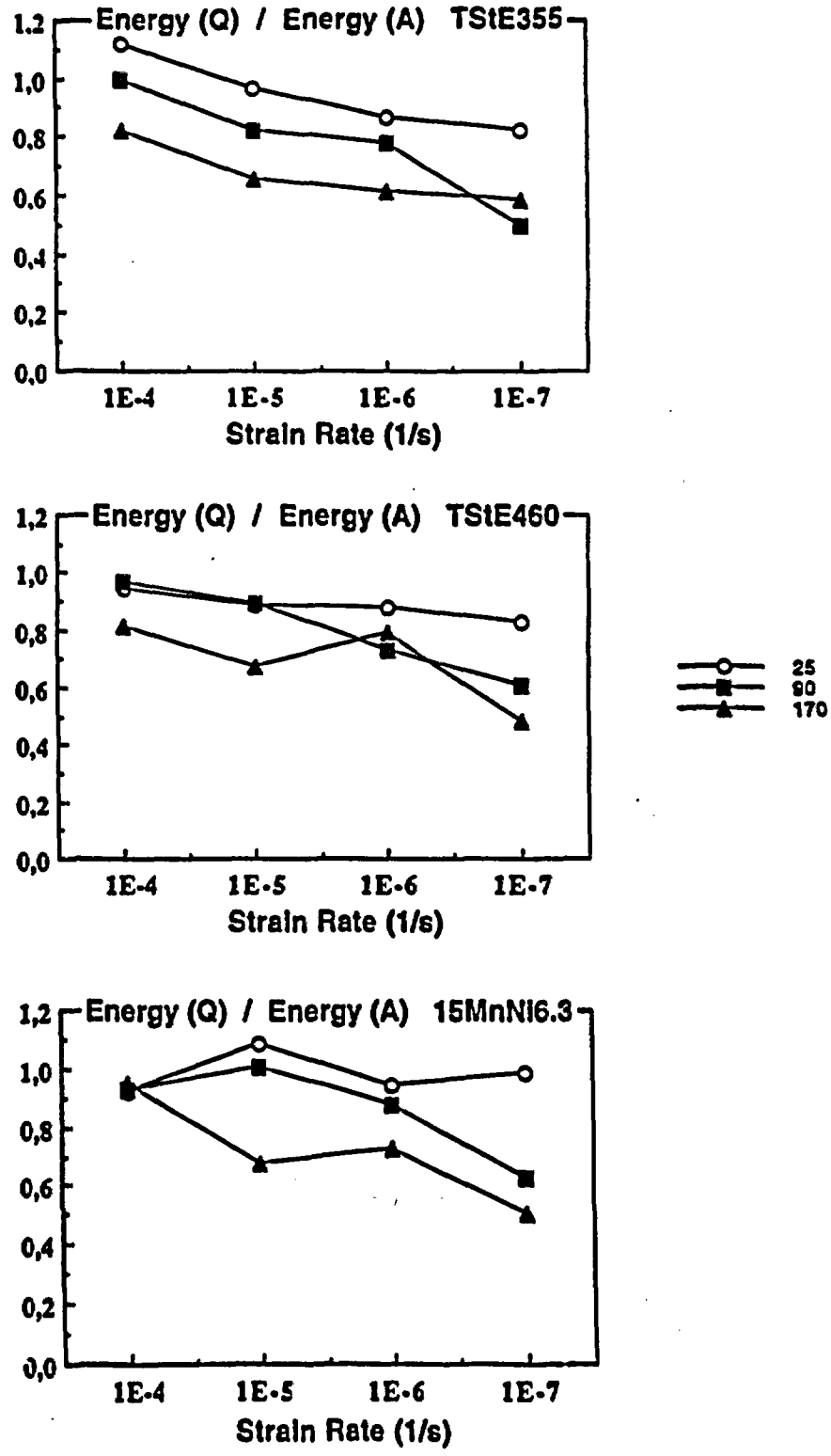

Fig. 62: Ratio of energies in Q-brine and argon versus strain rate for the TStE 355, TStE 460 and 15MnNi 6.3 steels at various temperatures

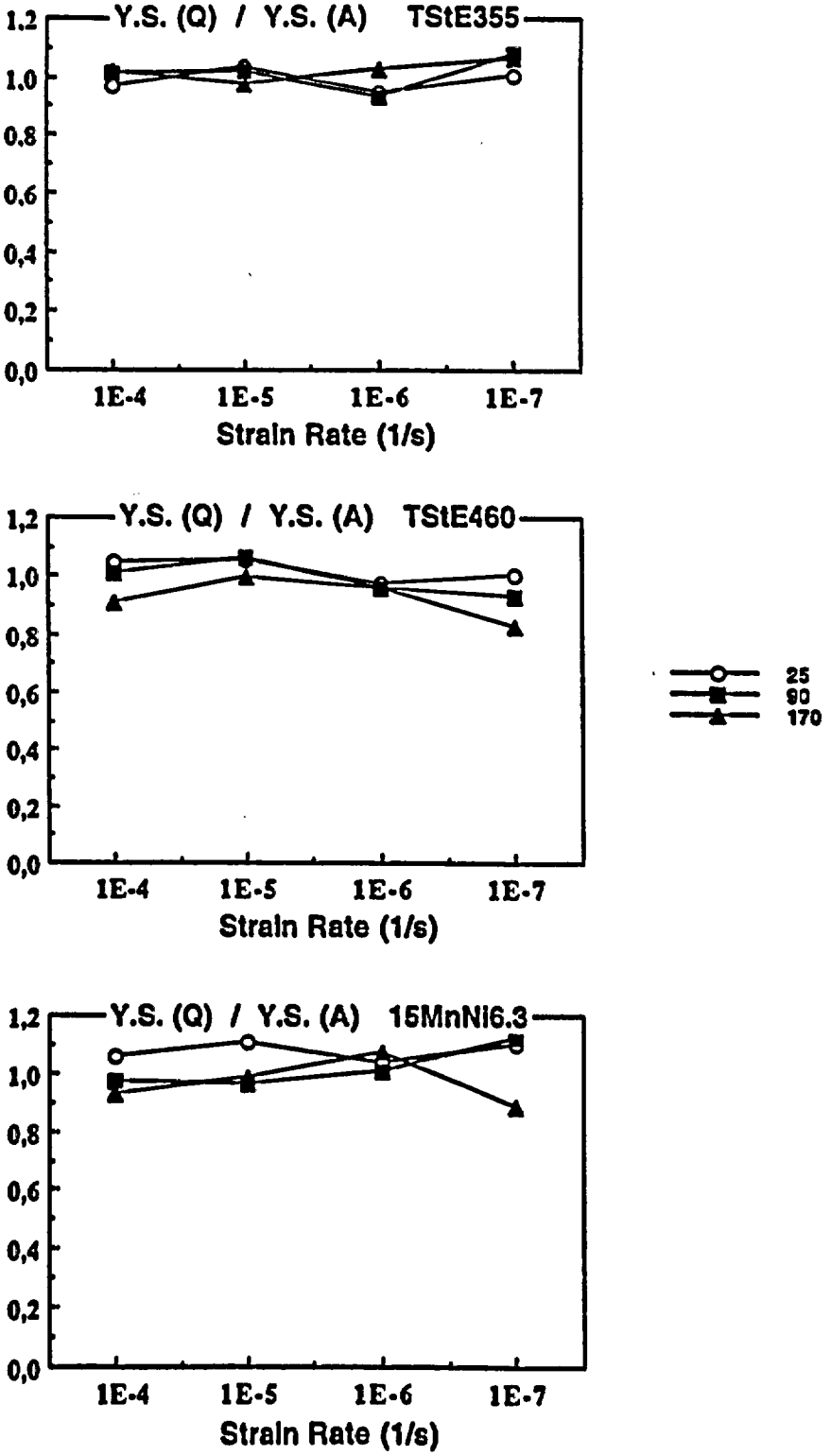

Fig. 63: Ratio of yield strengths in Q-brine and argon versus strain rate for the TStE 355, TStE 460 and 15MnNi 6.3 steels at various temperatures

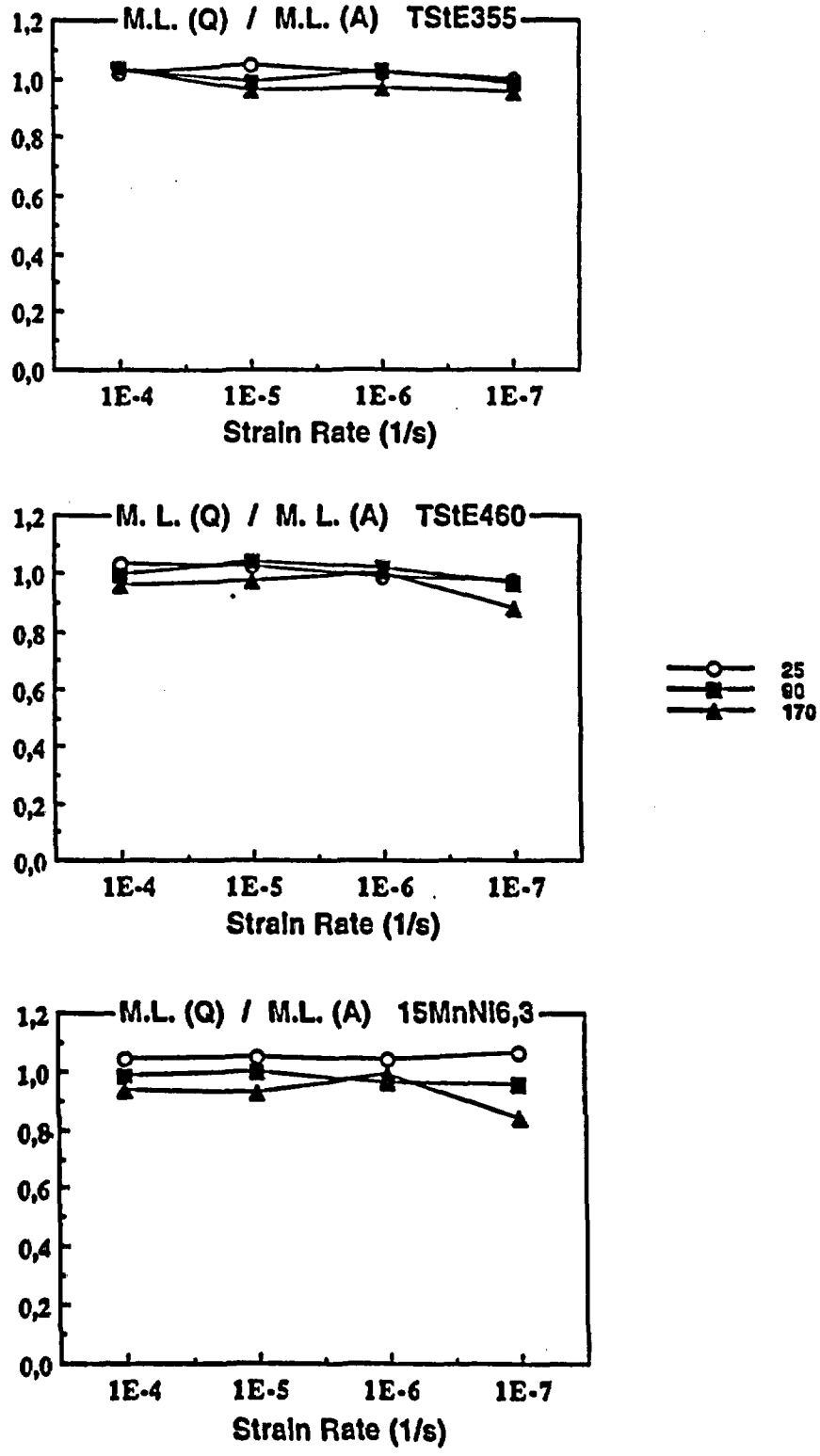

Fig. 64: Ratio of maximum loads in Q-brine and argon versus strain rate for the TStE 355, TStE 460 and 15MnNi 6.3 steels at various temperatures

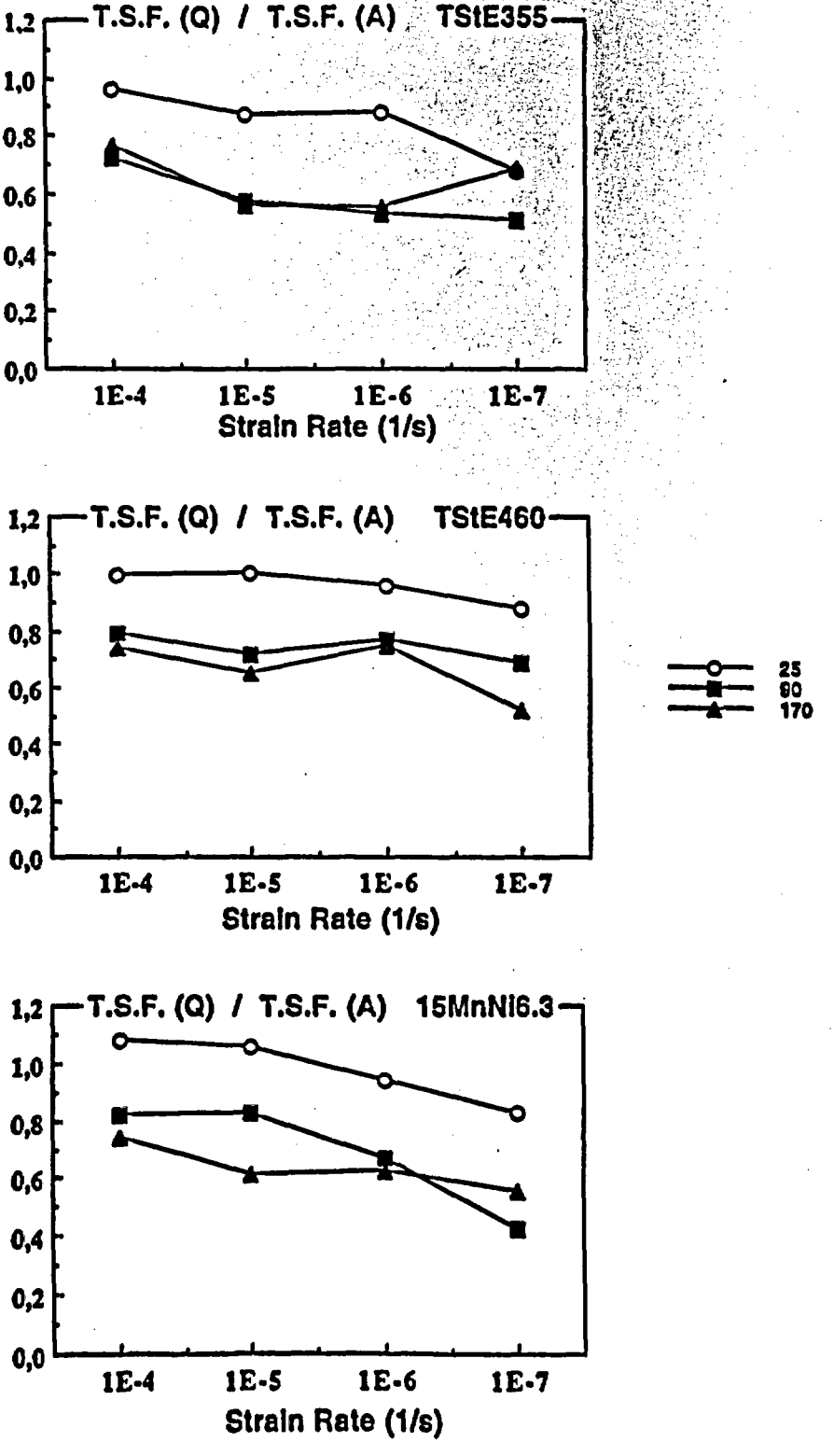

Fig. 65: Ratio of true stresses at fracture in Q-brine and argon versus strain rate for the TStE 355, TStE 460 and 15MnNi 6.3 steels at various temperatures

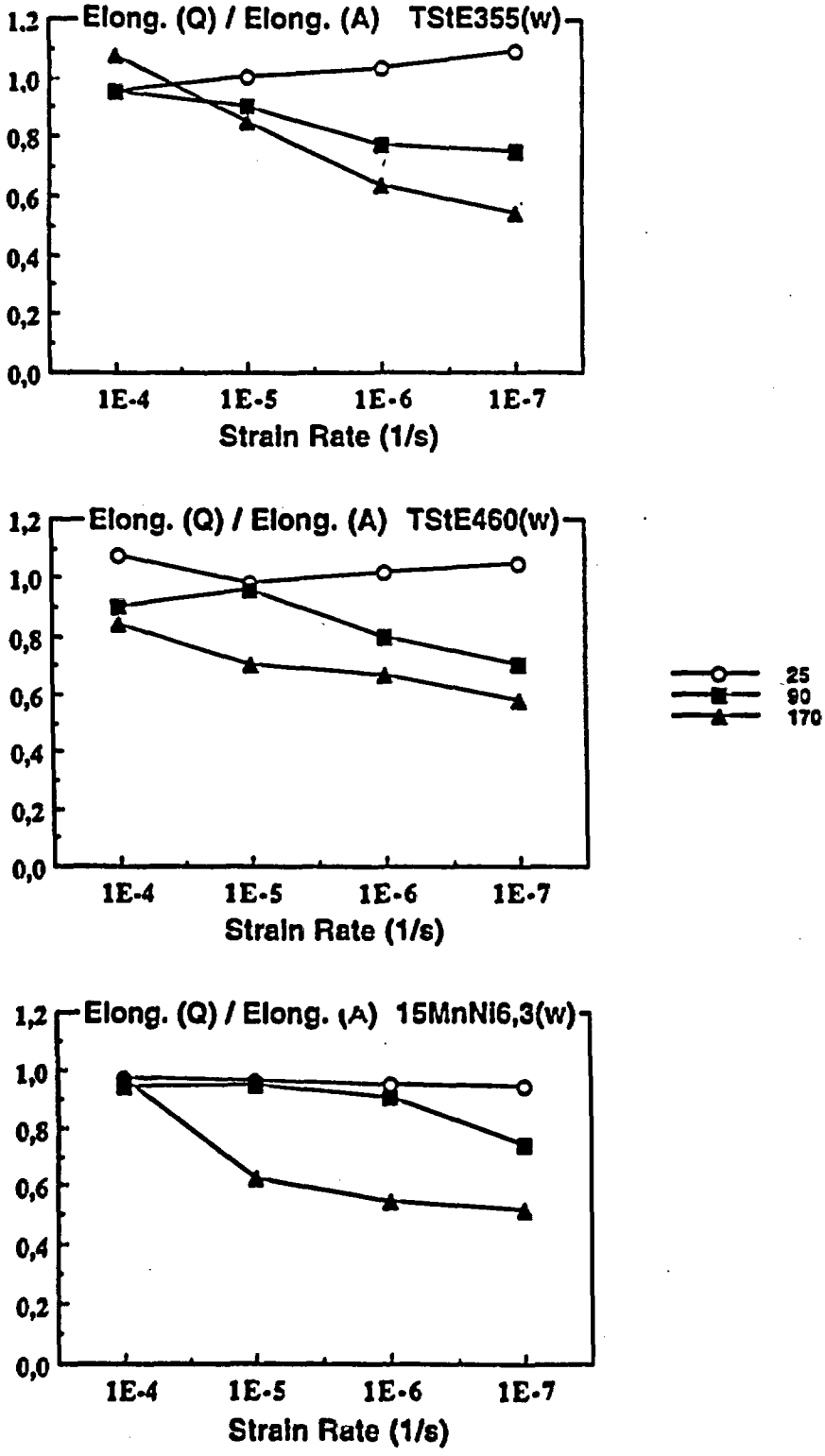

Fig. 66: Ratio of elongations in Q-brine and argon versus strain rate for the MAG welded TStE 355, TStE 460 and 15MnNi 6.3 steels at various temperatures

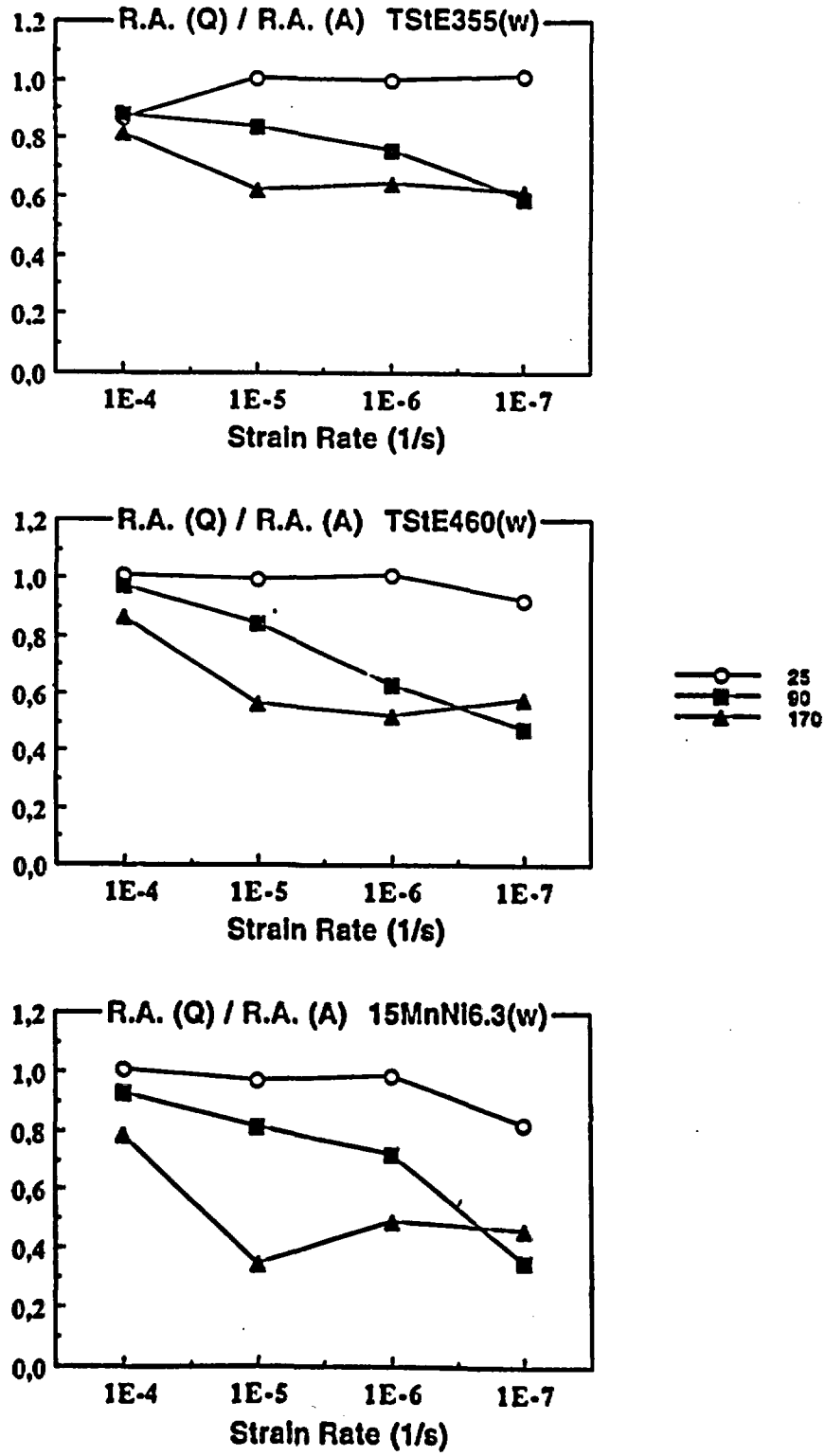

Fig. 67: Ratio of reduction of areas in Q-brine and argon versus strain rate for the MAG welded TStE 355, TStE 460 and 15MnNi 6.3 steels at various temperatures

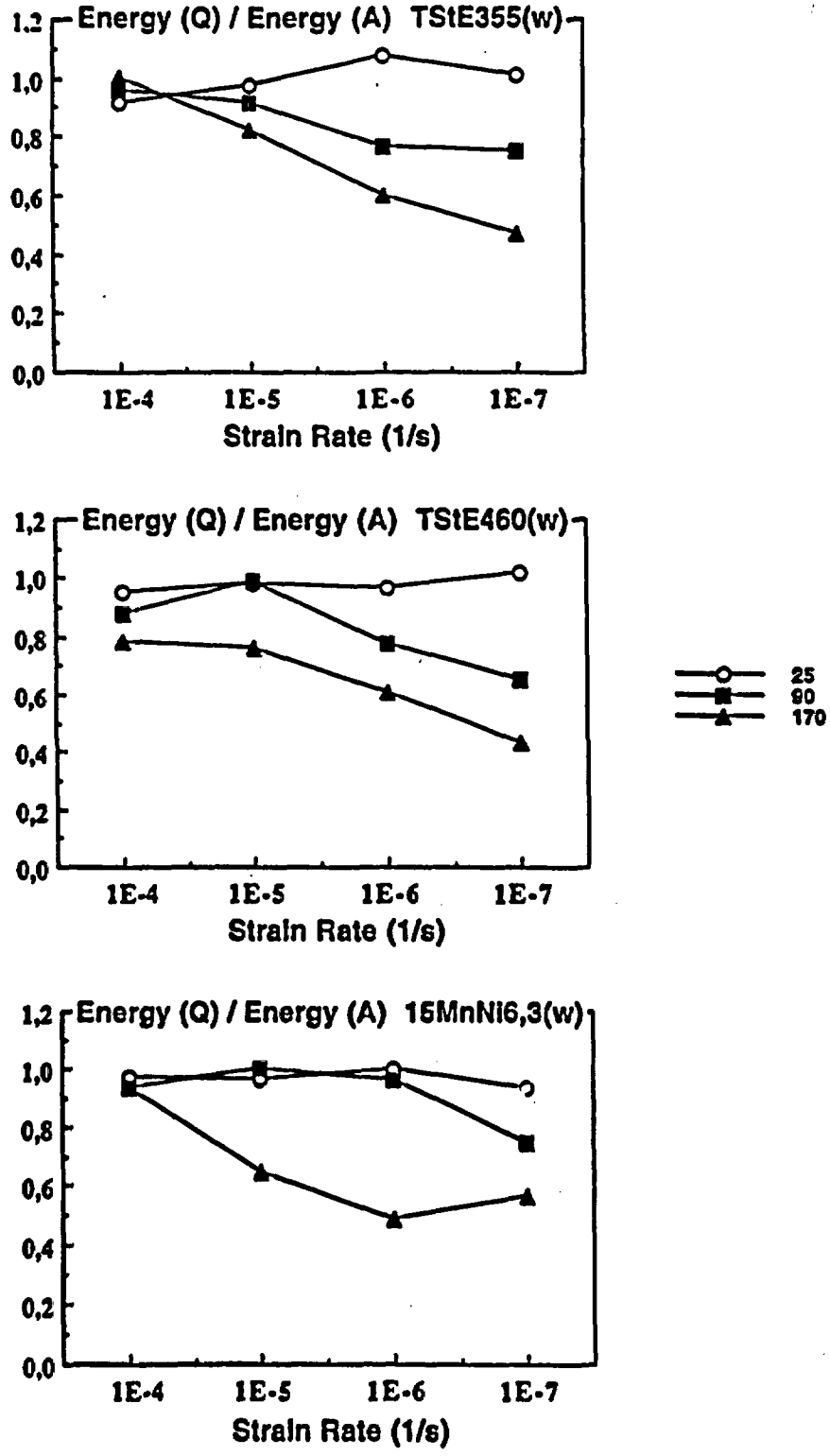

Fig. 68: Ratio of energies in Q-brine and argon versus strain rate for the MAG welded TStE 355, TStE 460 and 15MnNi 6.3 steels at various temperatures

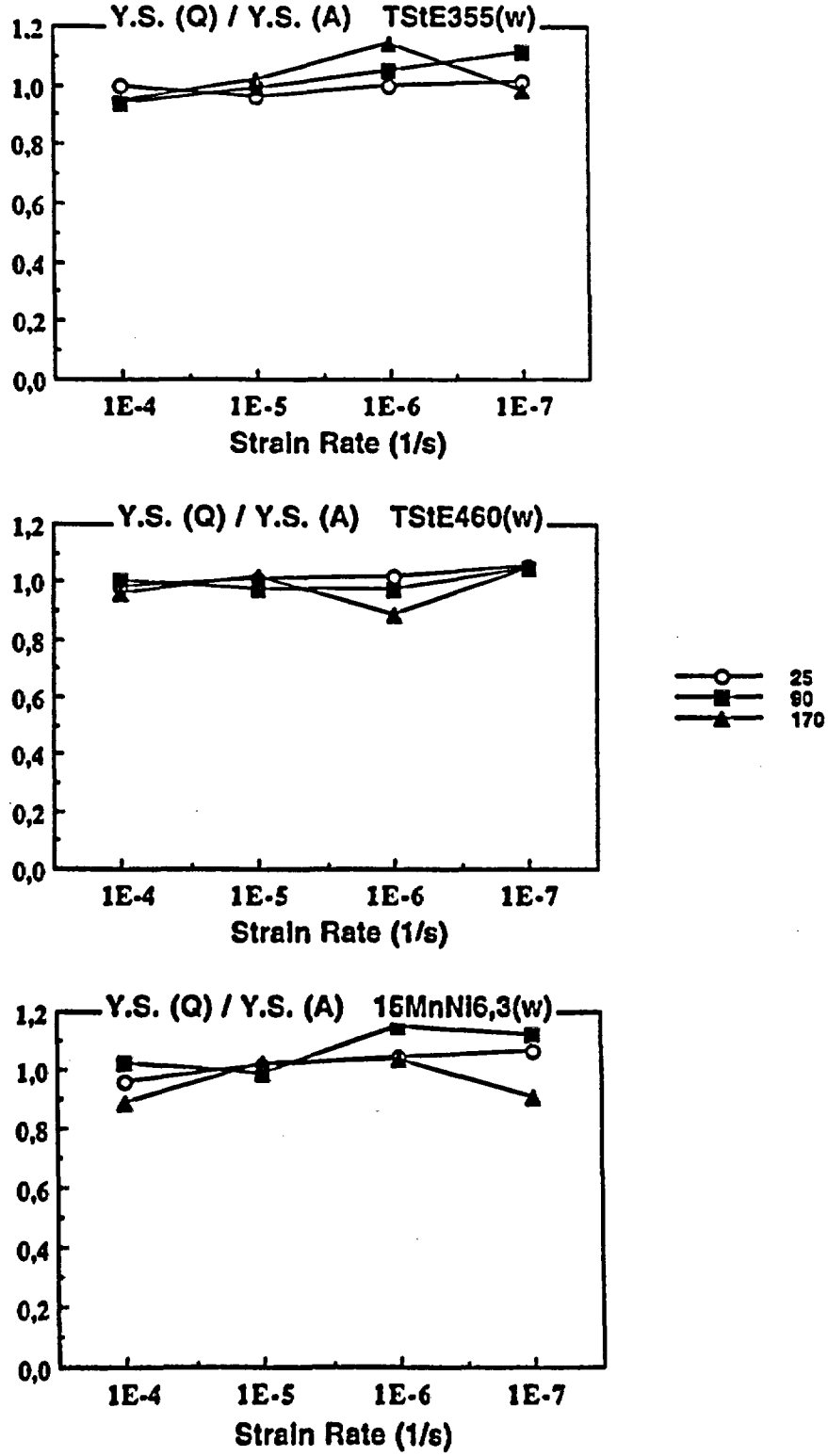

Fig. 69: Ratio of yield strengths in Q-brine and argon versus strain rate for the MAG welded TStE 355, TStE 460 and 15MnNi 6.3 steels at various temperatures

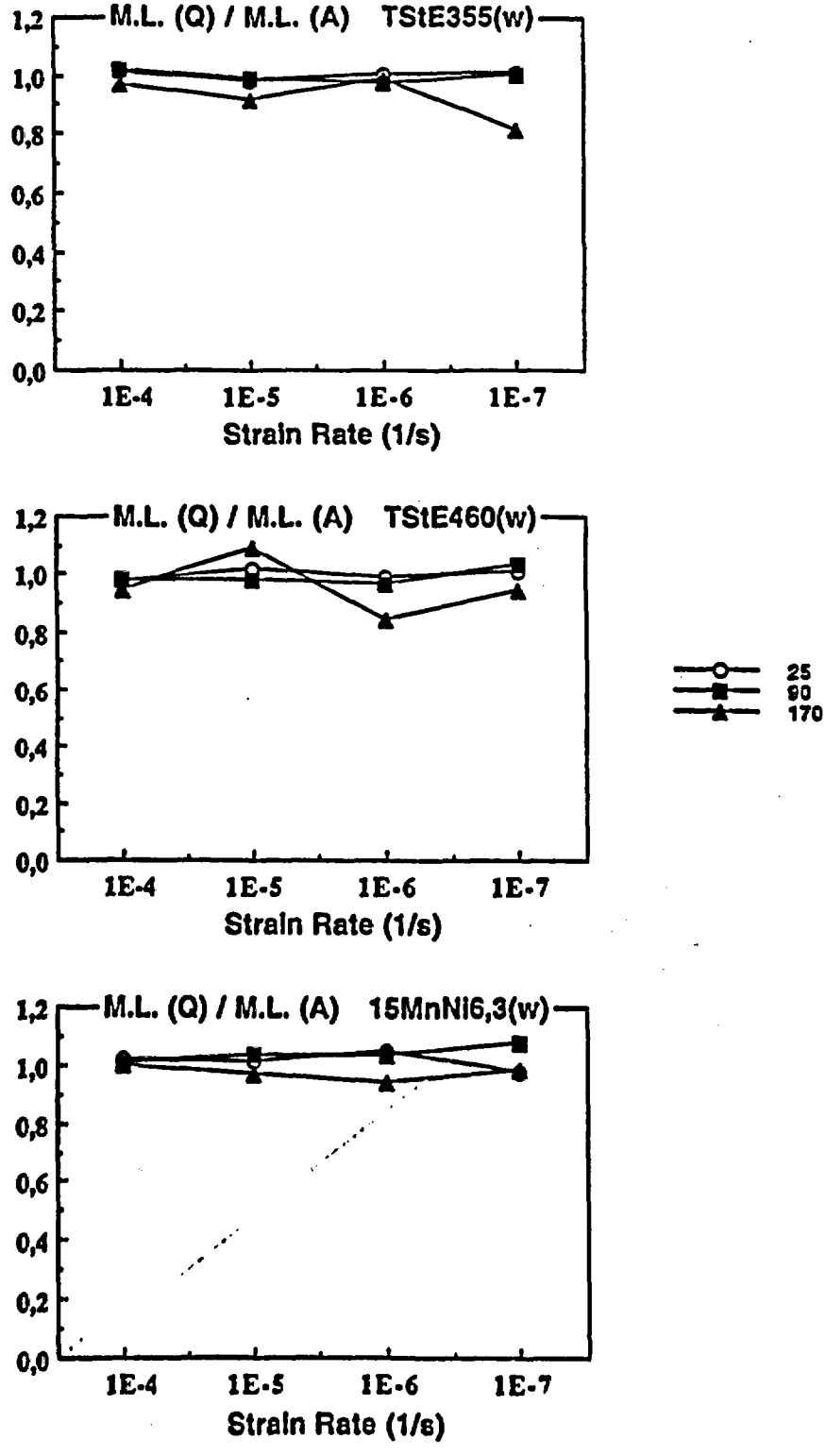

Fig. 70: Ratio of maximum loads in Q-brine and argon versus strain rate for the MAG welded TStE 355, TStE 460 and 15MnNi 6.3 steels at various temperatures

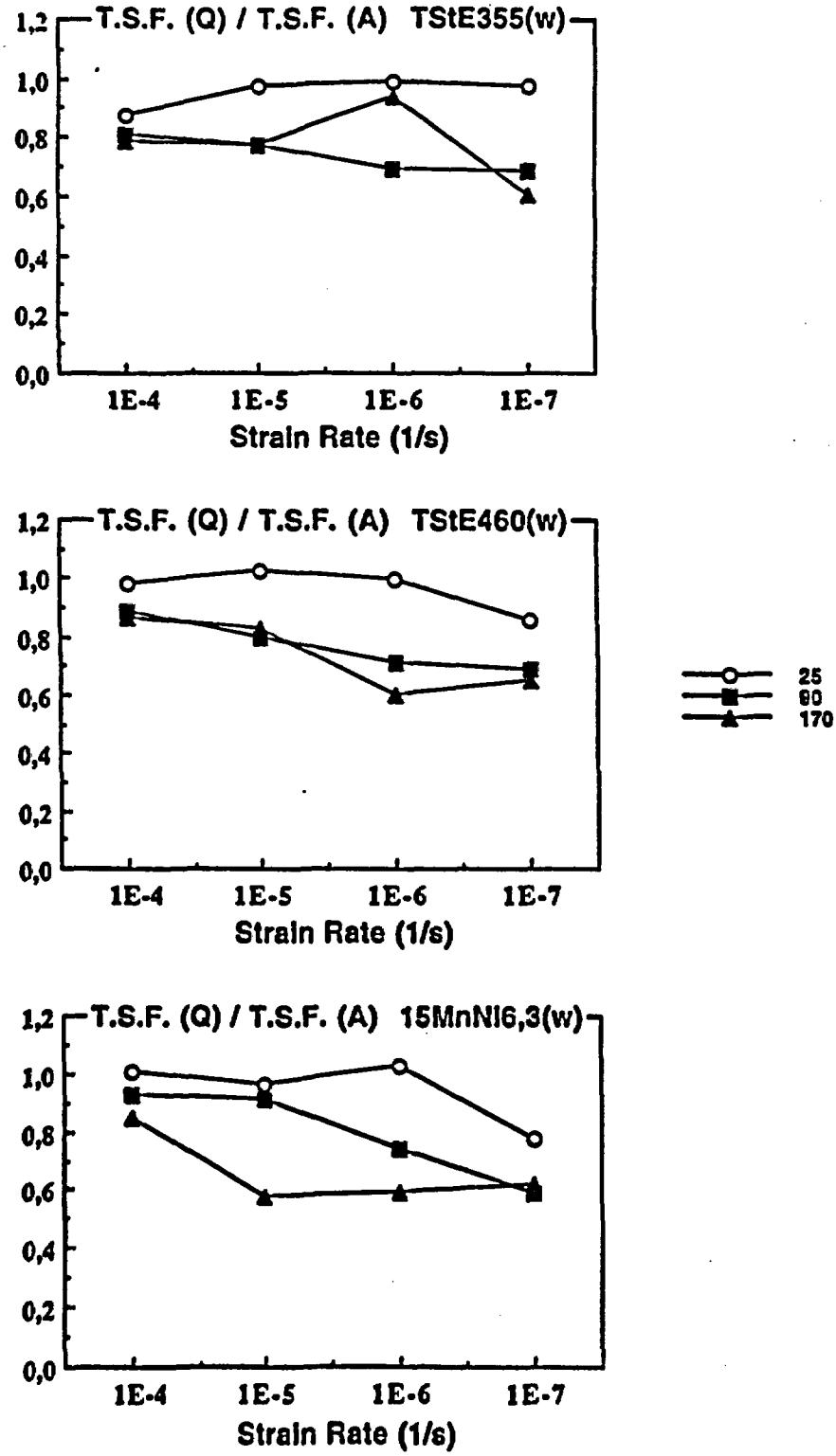

Fig. 71: Ratio of true stresses at fracture in Q-brine and argon versus strain rate for the MAG welded TStE 355, TStE 460 and 15MnNi 6.3 steels at various temperatures

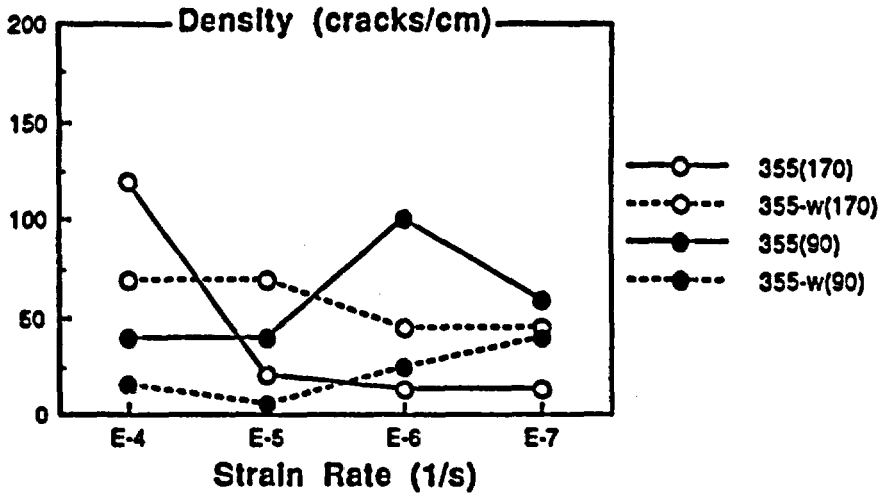

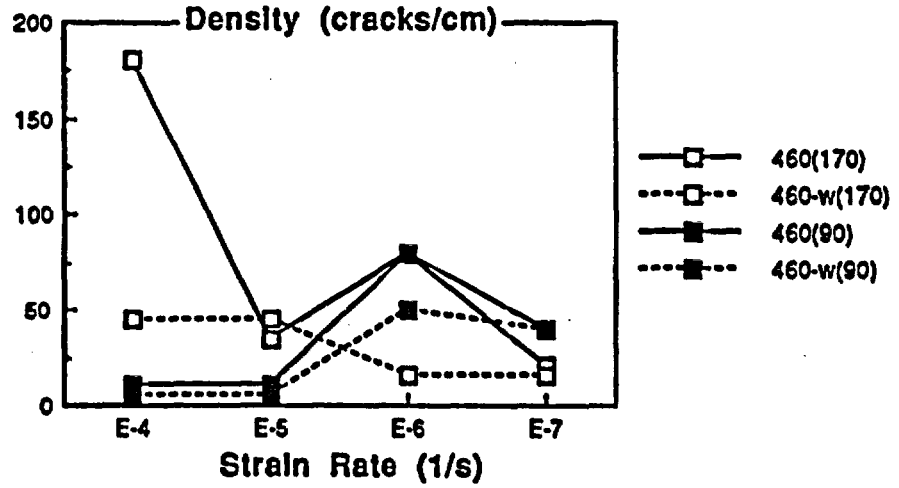

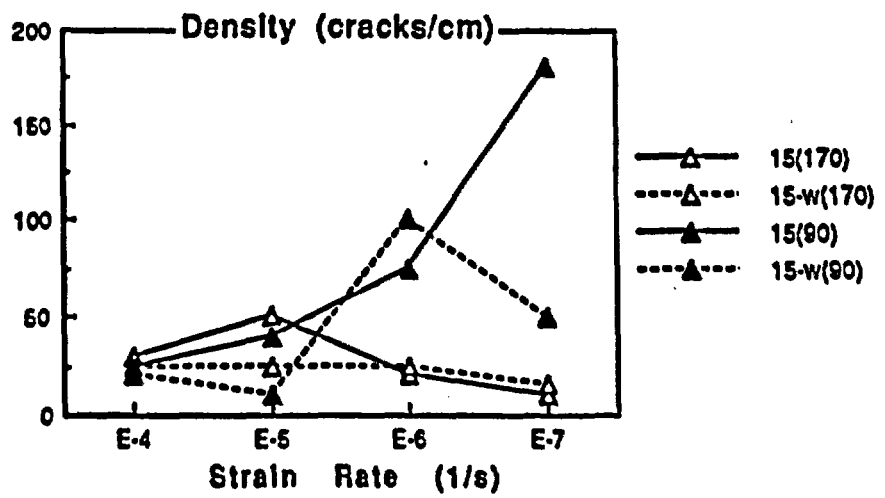

Fig. 72: Crack density obtained for the steels TStE 355, TStE 460 and 15MnNi 6.3 after slow strain rate testing in Q-brine under various conditions (T= 90°C, 170°C, w = welded material)

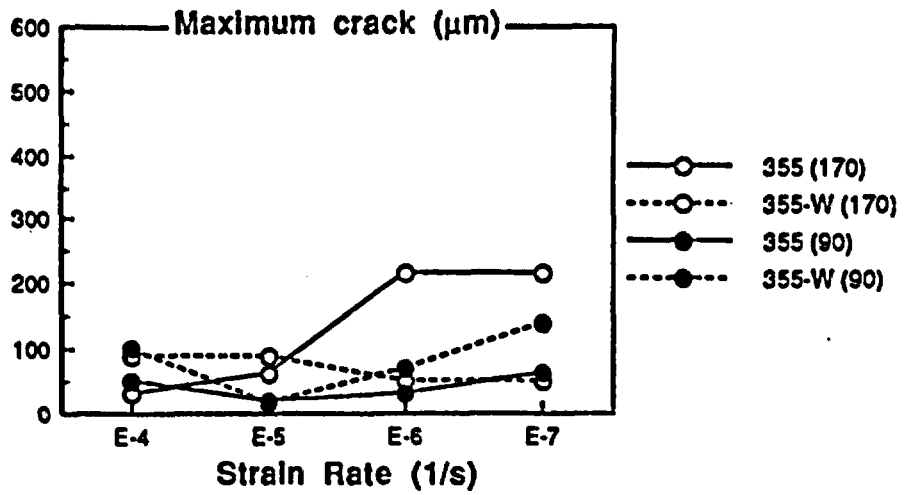

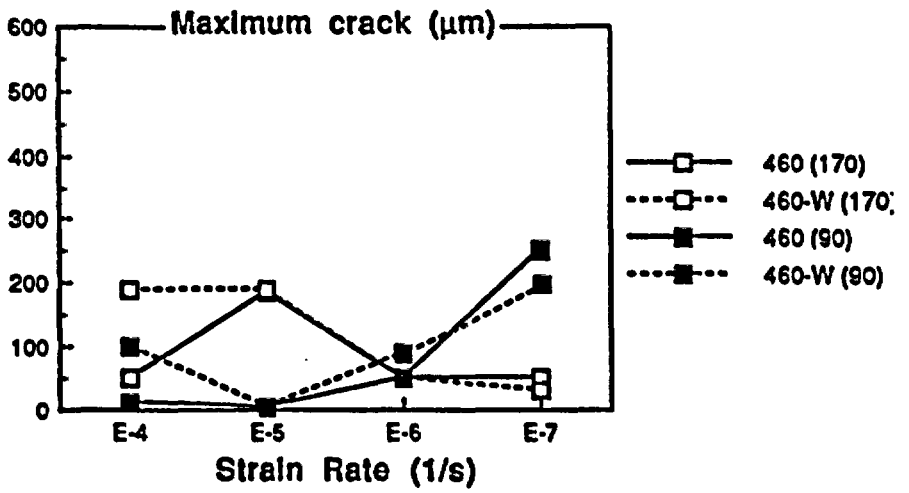

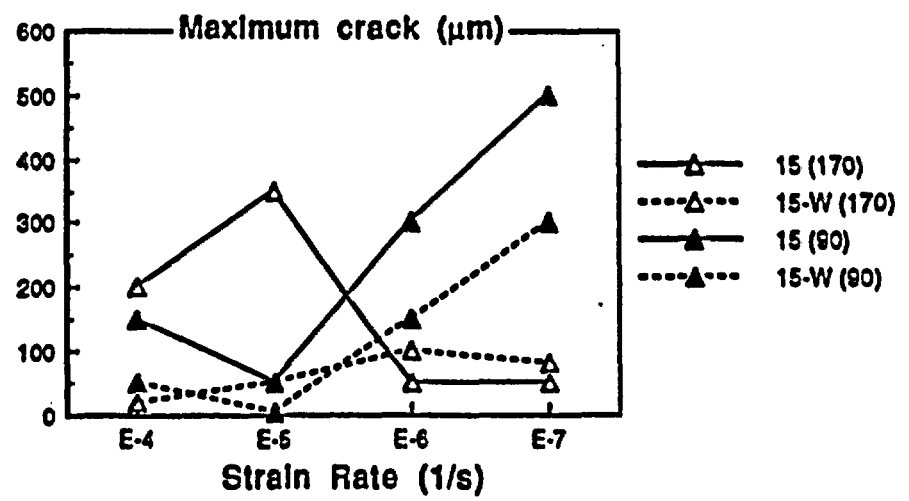

Fig. 73: Maximum crack length obtained for the steels TStE 355, TStE 460 and 15MnNi 6.3 after slow strain rate testing in Q-brine under various conditions (T= 90°C, 170°C, w = welded material)

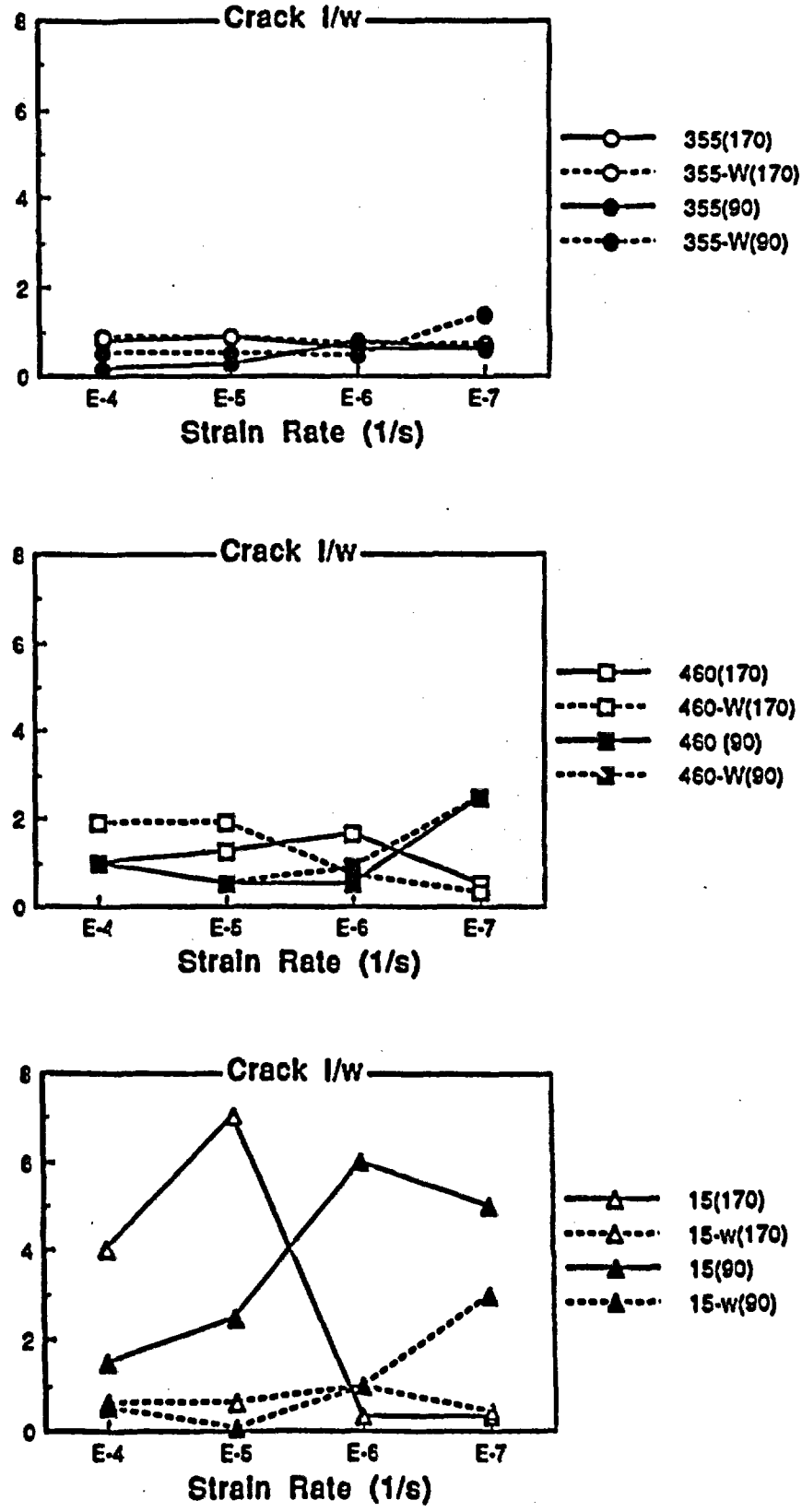

Fig. 74: Crack length to wide ratio obtained for the steels TStE 355, TStE 460 and 15MnNi 6.3 after slow strain rate testing in Q-brine under various conditions (T= 90°C, 170°C, w = welded material)